

Formation and stabilization of all-inorganic perovskites for photovoltaics

Présentée le 12 juin 2020

à la Faculté des sciences de base
Laboratoire des sciences photomoléculaires
Programme doctoral en chimie et génie chimique

pour l'obtention du grade de Docteur ès Sciences

par

Zaiwei WANG

Acceptée sur proposition du jury

Prof. J.-E. Moser, président du jury
Prof. U. A. Hagfeldt, directeur de thèse
Dr T. Edvinsson, rapporteur
Dr S. Yakunin, rapporteur
Prof. M. K. Nazeeruddin, rapporteur

Abstract

Hybrid perovskite materials, owing to their outstanding photo-physical properties, such as long charge carrier diffusion length, high light-harvesting efficiency, and tunable band gaps, have been extensively investigated in the fields of solar cells, light-emitting diodes and detectors. To date, the certified power conversion efficiency (PCE) of three dimensional (3D) organic-inorganic hybrid perovskite solar cells (PSCs) has reached 25.2%. Despite their outstanding performance, the 3D organic-inorganic hybrid PSCs are suffering from limited stability under moisture and heat due to the volatility of organic molecules such as methylammonium (MA) and formamidinium (FA), which hinders their further long-term application. By replacing volatile organic components with inorganic cations, all-inorganic perovskites CsPbX_3 ($\text{X} = \text{Br}, \text{I}$) are particularly attractive as emerging photoactive semiconductors to improve the stability of PSCs intrinsically. However, the desirable inorganic perovskites (such as CsPbI_3 and CsPbI_2Br) for high-efficiency inorganic PSCs are suffering from the thermodynamic phase instability, as the photoactive black phase (α , β , or γ phase) spontaneously transforms into a more thermodynamically stable yellow phase (δ -phase) in ambient condition, which is limiting the further development of high-performance inorganic PSCs. The stabilization of black phase and the formation of high-quality perovskite films are promoting the remarkable progress for the performance and stability of inorganic perovskite solar cells.

Firstly, we show that europium doping of CsPbI_2Br stabilizes the black phase of narrow band gap inorganic perovskite at room temperature. We rationalize it by using solid-state nuclear magnetic resonance and high-angle annular dark-field scanning transmission electron microscopy, which show that europium is incorporated into the perovskite lattice. We demonstrate a maximum power-conversion efficiency of 13.71% for an inorganic PSC with the composition $\text{CsPb}_{0.95}\text{Eu}_{0.05}\text{I}_2\text{Br}$ perovskite in the mesoscopic architecture and a stable power output of 13.34%. Stability tests show that the devices retain 93% of the initial efficiency after 370 hours under $100 \text{ mW}\cdot\text{cm}^{-2}$ continuous white light illumination under maximum power point tracking measurement.

Secondly, we demonstrate a function of dopants by adding barium in CsPbI_2Br . We find that barium is not incorporated into the perovskite lattice but induces phase segregation, resulting in a change in the iodide/bromide ratio compared to the precursor stoichiometry and consequently a reduction in the band gap energy of the perovskite phase. The device with 20 mol% barium shows a high power conversion efficiency of 14.0% and a great suppression of non-radiative recombination within the inorganic perovskite, yielding a high open-circuit voltage of 1.33 V and an external quantum efficiency of electroluminescence of 10^{-4} .

Then we propose an intermediate-phase engineering strategy to improve the inorganic perovskite/metal oxide interface by utilizing volatile salts. The introduction of organic cations (such as methylammonium and formamidinium), which can be doped into the perovskite lattice, leads to the formation of an organic-inorganic hybrid perovskite intermediate phase, promoting a robust interfacial contact through hydrogen bonding. A champion $\text{CsPb}(\text{I}_{0.75}\text{Br}_{0.25})_3$ -based device with a power conversion efficiency of 17.0% and an open-circuit voltage of 1.34 V was realized, implying that a record of over 65% of the Shockley-Queisser efficiency limit is achieved.

Last, the intermediate phase engineering strategy is reported to promote the pure γ -phase CsPbI_3 perovskite film formation. According to the investigation of the phase transformation processes of pure CsPbI_3 and that with different additives, including NH_4I , BAI, MAI, FAI and DMAI, we found that the formation of a 3D organic-inorganic hybrid perovskite intermediate phase is essential to avoid the generation of undesired yellow phase and promote the formation of pure black-phase CsPbI_3 film. A champion efficiency of 17.70% with a stabilized power output of 17.58% based on the optimized CsPbI_3 -DMAI device is achieved.

Overall, we investigate two possible scenarios for element doping: (1) the dopants are incorporated into the crystal lattice for the improvement of stability and efficiency of inorganic PSCs; (2) the dopants form separate phases to induce the halide phase segregation and suppress non-radiative recombination of perovskite films. Besides, based on the formation of 3D organic-inorganic hybrid perovskite intermediate phase, we not only promote the formation of pure black phase CsPbI_3 , but also promotes a robust interfacial contact of inorganic perovskite and metal oxide transport layers.

Keywords: inorganic perovskites, perovskite solar cells, element doping, intermediate phase, interfacial contact, phase transformation

Resume

Les matériaux pérovskites hybrides, en raison de leurs propriétés photo-physiques exceptionnelles telles que la longue longueur de diffusion du porteur de charge, la grande efficacité de récolte de la lumière et le caractère ajustable de leurs bandes interdites, ont fait l'objet d'études approfondies dans le domaine des cellules solaires, des diodes électroluminescentes et des détecteurs. À ce jour, l'efficacité certifiée de conversion photo-électrique (PCE) des cellules solaires tridimensionnelles (3D) à pérovskites hybrides organiques-inorganiques (PSC) a atteint 25,2 %. Malgré leurs performances exceptionnelles, les PSC hybrides organiques-inorganiques 3D souffrent d'une stabilité limitée sous atmosphère humide et/ou chaude en raison de la volatilité des molécules organiques les composant, telles que le méthylammonium (MA) et le formamidinium (FA), ce qui, jusqu'à maintenant, prévient leur stabilité à long terme et donc leur application dans le monde industriel. En remplaçant les composants organiques volatils par des cations inorganiques, des pérovskites entièrement inorganiques CsPbX_3 ($X = \text{Br}, \text{I}$) sont obtenus. Ces derniers sont particulièrement intéressants en tant que nouveaux semi-conducteurs photoactifs pour améliorer la stabilité intrinsèque des PSC. Cependant, les pérovskites inorganiques de composition souhaitable (telles que CsPbI_3 et CsPbI_2Br) pour le développement de PSC inorganiques à haute efficacité souffrent de l'instabilité de la phase thermodynamique, car la phase noire photoactive (phase α , β ou γ) se transforme spontanément en une phase jaune plus stable thermodynamiquement (phase δ) dans les conditions ambiantes, limitant donc à l'heure actuelle le développement des PSC inorganiques à haute performance. La stabilisation de la phase noire et la formation de films de pérovskites de haute qualité constituent des pistes de progrès remarquables pour la performance et la stabilité des cellules solaires à pérovskite inorganiques.

Tout d'abord, nous montrons que le dopage à l'euporium du CsPbI_2Br stabilise à température ambiante la phase noire de la pérovskite inorganique à bande interdite étroite. Nous le rationalisons en utilisant la résonance magnétique nucléaire (RMN) à l'état solide et la microscopie électronique en transmission à balayage annulaire (TEM) à grand angle en champ noir, qui démontrent que l'euporium est incorporé dans le réseau du pérovskite. Nous démontrons une efficacité de conversion photo-électrique (PCE) maximale de 13,71% pour une cellule solaire à pérovskites (PSC) inorganique de composition $\text{CsPb}_{0,95}\text{Eu}_{0,05}\text{I}_2\text{Br}$ en utilisant l'architecture mésoscopique et une puissance de sortie stabilisée de 13,34%. Les tests de stabilité montrent que les appareils conservent 93% de l'efficacité initiale après 370 heures sous un éclairage continu de 100 mW.cm^{-2} en lumière blanche avec une mesure de suivi du point de puissance maximale.

Deuxièmement, nous démontrons l'effet du doping en ajoutant du baryum dans le CsPbI_2Br . Nous constatons que le baryum n'est pas incorporé dans le réseau du pérovskite mais induit une ségrégation de phase, ce qui entraîne une modification du rapport iode/bromure par rapport à la stoechiométrie du précurseur et, par conséquent, une réduction de l'énergie de la bande interdite de la phase pérovskite. Le dispositif avec 20 mol% de baryum montre un rendement élevé de conversion photo-électrique de 14,0% et une grande suppression de la recombinaison non radiative au sein du pérovskite inorganique, résultant en une tension élevée en circuit ouvert de 1,33 V et un rendement quantique externe de l'électroluminescence (EQE) de 10^{-4} .

Nous proposons ensuite une stratégie d'ingénierie en phase intermédiaire pour améliorer l'interface pérovskite inorganique/oxyde métallique en utilisant des sels volatils. L'introduction de cations organiques (tels que le méthylammonium et le formamidinium), qui peuvent être dopés dans le réseau du pérovskite, conduit à la formation d'une phase intermédiaire hybride pérovskite organique-inorganique, favorisant un contact interfacial robuste grâce à la liaison hydrogène. Un dispositif champion à base de $\text{CsPb}(\text{I}_{0,75}\text{Br}_{0,25})_3$ avec une efficacité de conversion photoélectrique de 17,0% et une tension de circuit ouvert de 1,34 V a été réalisé, ce qui implique qu'un record de plus de 65% de la limite d'efficacité de Shockley-Queisser est atteint.

Enfin, la stratégie d'ingénierie de la phase intermédiaire favoriserait la formation d'un film de pérovskite de CsPbI_3 en phase pure γ . D'après l'étude des processus de transformation de phase du CsPbI_3 pur et des différents additifs, notamment NH_4I , BAI , MAI , FAI et DMAI , nous avons constaté que la formation d'une phase intermédiaire hybride perovskite organique-inorganique 3D est essentielle pour éviter la génération d'une phase jaune indésirable et favoriser la formation d'un film de CsPbI_3 en phase noire pure. Le dispositif CsPbI_3 -DMAI optimisé permet d'obtenir un rendement champion de 17,70 % avec une puissance stabilisée de 17,58 %.

Dans l'ensemble, nous étudions donc deux scénarios possibles de doping des éléments : (1) les dopants sont incorporés dans le réseau cristallin pour améliorer la stabilité et l'efficacité des PSC inorganiques ; (2) les dopants forment des phases séparées pour induire la séparation des phases halogénures et supprimer la recombinaison non radiative des films de pérovskite. En outre, en se basant sur la formation d'une phase intermédiaire hybride perovskite organique-inorganique 3D, nous ne favorisons pas seulement la formation de la phase noire pure CsPbI_3 , mais nous favorisons également un contact interfacial robuste des couches de transport du perovskite inorganique et des oxydes métalliques.

Mots-clés: pérovskites inorganiques, cellules solaires pérovskites, dopage d'élément, phase intermédiaire, contact interfacial, transformation de phase.

List of Figures

- Figure 1.1. Structural properties of lead-based halide inorganic perovskites.** (a) Crystal structure of the different phases for CsPbI_3 and their relative phase transitions.²¹ (b) Schematic crystal structures and transition of the inorganic CsPbBr_3 perovskite and its derivatives (CsPb_2Br_5 , and Cs_4PbBr_6).³⁸ (c) Changes of lattice parameter and bandgap energy in $\text{CsPb}(\text{Br}_x\text{I}_{1-x})_3$ with increasing Br content.⁴¹ (d) Photoluminescent peak position as a function of time for $\text{CsPb}(\text{Br}_x\text{I}_{1-x})_3$ under ~ 1 sun illumination.⁴¹ 4
- Figure 1.2. Intermediate phase engineering (IPE) for phase transformation.** Chemical composition and phase evolution in dimethylammonium iodide (DMAI)-derived CsPbI_3 .⁵¹ 6
- Figure 1.3. Residual solvent modulation for inorganic film formation.** (a) Schematic illustration of CsPbI_3 -perovskite film formation procedures via solvent-controlled growth (SCG).¹⁴ SEM images of annealed CsPbI_3 perovskite precursor films without (b) and with (c) SCG, respectively.¹⁴ Scale bar: 20 μm . (d) Schematic illustration of CsPbI_2Br perovskite crystallization process via gradient thermal annealing (GTA) alone or in synergetic with antisolvent treatment (ATS).⁶² 8
- Figure 1.4. Modulation of annealing procedures for formation of inorganic perovskite films.** (a) X-ray diffraction patterns of a CsPbI_2Br films annealed at different temperature ranging from 100 to 350 $^\circ\text{C}$.⁶⁶ (b) Schematic of adsorbed oxygen molecule passivation and oxygen atom passivation for inorganic perovskite.⁶⁷ (c) Dissociation process of O_2 molecule at halide vacancy.⁶⁷ (d) Illustration of a CsPbI_2Br film with room temperature (RT) DMSO vapor annealing.⁶⁹ 9
- Figure 1.5. Two-step methods for fabrication of inorganic perovskite films.** (a) Schematic process for fabrication of a CsPbBr_3 film by the dipping method.⁷⁹ (b) Multistep solution-processing deposition of CsBr on PbI_2 film and the corresponding top-view SEM images of the corresponding all-inorganic lead halide film.³⁷ (c) The procedure of CsPbBr_3 combining with CsPb_2Br_5 and Cs_4PbBr_6 derivative-phase films via the sequential vapor deposition method.³⁸ 11
- Figure 1.6. Element doping and composition regulation for stabilization of inorganic films.** (a) Characteristics of Quasi-2D $\text{PEA}_2\text{Cs}_{n-1}\text{Pb}_n\text{X}_{3n+1}$ perovskite films and decomposition energetics using first-principles density functional theory (DFT) of perovskite with different $\langle n \rangle$ values.⁸² (b) Schematic crystal structure of CsPbI_3 .

$x\text{Sn}_x\text{I}_3$. ⁸⁵ (c) Variation of experimental (solid circle) and calculated (open circle) bandgaps as a function of x in $\text{CsPb}_{1-x}\text{Sn}_x\text{I}_3$. ⁸⁵	14
--------------------------------------------------------------------------------------------------------------------------------------------------------------------------------------------------------------------	----

Figure 1.7. Nano crystallization, organic modulation, and surface passivation for stabilization of inorganic perovskite films. (a) Schematic (with TEM image of quantum dots (QDs)) and SEM cross-section of the QD- CsPbI_3 PV cell. ⁹⁹ (b) Schematic diagram of the chemical bonding between CsPbI_3 and polyvinylpyrrolidone (PVP) molecules. PVP molecule contains of long-chain alkyls and acylaminos. The unbounded lone pairs for nitrogen/oxygen (N/O) atoms in acylaminos offer excess electrons and interact with Cs ions in CsPbI_3 . ¹⁰³ (c) Mechanism and scheme for the formation of cubic phase CsPbI_3 with the assistant of PVP in three stages. ¹⁰³ (d) Schematic illustration of gradient Br doping and phenyltrimethylammonium (PTA) organic cation passivation. ¹⁰⁷	16
---------------------------------------------------------------------------------------------------------------------------------------------------------------------------------------------------------------------------------------------------------------------------------------------------------------------------------------------------------------------------------------------------------------------------------------------------------------------------------------------------------------------------------------------------------------------------------------------------------------------------------------------------------------------------------------------------------------------------------------------------------------------------------------------------------------------------------------------------------------------------------------	----

Figure 2.1. Photovoltaic Performance of perovskite solar cells (PSCs). (a) Cross-sectional SEM image of a complete $\text{CsPb}_{0.95}\text{Eu}_{0.05}\text{I}_2\text{Br}$ inorganic PSCs. The scale bar is 400 nm. (b) J-V characteristics of inorganic perovskite solar cells fabricated using $\text{CsPb}_{1-x}\text{Eu}_x\text{I}_2\text{Br}$ ($x=0.00-0.09$) absorbers. (c) IPCE characteristics of inorganic perovskite solar cells fabricated using $\text{CsPb}_{1-x}\text{Eu}_x\text{I}_2\text{Br}$ ($x=0.00-0.09$) absorbers. (d) Stabilized power output at maximum power point tracking under working condition with 100 mW cm^{-2} irradiation. (e) Hysteresis of the one of the best $\text{CsPb}_{0.95}\text{Eu}_{0.05}\text{I}_2\text{Br}$ devices with the scan rate of 10 mV s^{-1} . (f) J-V curve of one of the best performing $\text{CsPb}_{0.95}\text{Eu}_{0.05}\text{I}_2\text{Br}$ PSCs with the highest V_{oc}	22
--------------------------------------------------------------------------------------------------------------------------------------------------------------------------------------------------------------------------------------------------------------------------------------------------------------------------------------------------------------------------------------------------------------------------------------------------------------------------------------------------------------------------------------------------------------------------------------------------------------------------------------------------------------------------------------------------------------------------------------------------------------------------------------------------------------------------------------------------------------------------------------------------------------------------------------------------------------------------------	----

Figure 2.2. Structure characterization of europium-doped CsPbI_2Br. (a) XRD patterns of perovskite thin films of $\text{CsPb}_{1-x}\text{Eu}_x\text{I}_2\text{Br}$ ($0 \leq x \leq 0.09$), * represents the FTO peaks. (b) ^{133}Cs solid-state MAS NMR spectra of mechanochemical perovskite compositions measured at 11.7 T 20 kHz MAS and 298 K. † is a transmitter artefact, * is a spinning sideband. (c) ^{133}Cs spin-lattice relaxation times, T_1 , of selected perovskite compositions (details in the text). The solid curves are stretched exponential fits. The dashed line is the best bi-exponential fit of the $\text{CsPb}_{0.95}\text{Eu}_{0.05}\text{I}_2\text{Br}$ data set. (d) HAADF-STEM image and elemental maps of $\text{CsPb}_{0.95}\text{Eu}_{0.05}\text{I}_2\text{Br}$. The white bar indicates 100 nm.....	25
---------------------------------------------------------------------------------------------------------------------------------------------------------------------------------------------------------------------------------------------------------------------------------------------------------------------------------------------------------------------------------------------------------------------------------------------------------------------------------------------------------------------------------------------------------------------------------------------------------------------------------------------------------------------------------------------------------------------------------------------------------------------------------------------------------------------------------------------------------------------------------------------------	----

Figure 2.3. Morphology Characterization. SEM images of (a) CsPbI_2Br , (b) $\text{CsPb}_{0.99}\text{Eu}_{0.01}\text{I}_2\text{Br}$, (c) $\text{CsPb}_{0.97}\text{Eu}_{0.03}\text{I}_2\text{Br}$, (d) $\text{CsPb}_{0.95}\text{Eu}_{0.05}\text{I}_2\text{Br}$, (e) $\text{CsPb}_{0.93}\text{Eu}_{0.07}\text{I}_2\text{Br}$ and (f) $\text{CsPb}_{0.91}\text{Eu}_{0.09}\text{I}_2\text{Br}$ perovskite thin films. The scale bar is 400 nm.	26
--------------------------------------------------------------------------------------------------------------------------------------------------------------------------------------------------------------------------------------------------------------------------------------------------------------------------------------------------------------------------------------------------------------------------------------------------------------------------	----

Figure 2.4. Optical characterization of CsPbI_2Br and $\text{CsPb}_{0.95}\text{Eu}_{0.05}\text{I}_2\text{Br}$ perovskite thin films. (a) Normalized UV-Vis absorption and PL emission spectra measured at 298 K, (b) Time-resolved photoluminescence decays measured at 298 K.	26
----------------------------------------------------------------------------------------------------------------------------------------------------------------------------------------------------------------------------------------------------------------------------------------------------------------------------------	----

- Figure 2.5. Optoelectronic characterization of devices.** (a) external quantum yield of electroluminescence (EQE_{EL}) measured while performing a current-voltage sweep (10 mV/s) and plotted as a function of the injection current. The curves follow a power-law, resulting in the given ideality factors n_{ID} . (b) V_{oc} as a function of the light intensity extracted from the transient experiment. The resulting n_{ID} are slightly dependent on the scan direction. (c) Ideality factor differentially deduced from (b) and corrected for transients. The arrows indicate the scan direction. 27
- Figure 2.6. Phase stability of perovskite films.** (a) Digital photographs of $CsPbI_2Br$ and $CsPb_{0.95}Eu_{0.05}I_2Br$ perovskite thin films on mesoporous TiO_2 exposed to ambient conditions over the period of time indicated below each snapshot.(relative humidity under c.a 20-40%, h: hours m: months) (b) XRD patterns of $CsPbI_2Br$ and $CsPb_{0.95}Eu_{0.05}I_2Br$ films in (b) freshly prepared (humidity under c.a 20-40%, 298 ± 5 K), (c) ambient condition for 1200 h (humidity under c.a 20-40%, 298 ± 5 K) and (d) humid condition for 100 h (humidity under c.a 50-70%, 298 ± 5 K). The evolution of UV-Vis spectra of $CsPbI_2Br$ (e) and $CsPb_{0.95}Eu_{0.05}I_2Br$ (f) perovskite thin films stored in ambient conditions (humidity under c.a 50-70%, 298 ± 5 K). 28
- Figure 2.7. Stability characterization of PSCs.** Normalized PCE of unencapsulated $CsPbI_2Br$ and $CsPb_{0.95}Eu_{0.05}I_2Br$ devices monitored under continuous white light exposure as a function of time. 29
- Figure 3.1. Digital images of the $CsPb_{1-x}Ba_xI_2Br$ ($x = 0$ to 1) inorganic perovskite films on mesoporous TiO_2 substrates.** 36
- Figure 3.2. Materials characterization of $CsPb_{1-x}Ba_xI_2Br$ with x varies from 0 to 0.4 compositions.** a) XRD patterns, b) UV-Vis absorption and c) PL emission spectra. 37
- Figure 3.3. Photovoltaic performance of PSCs.** (a) Cross-sectional SEM image of a complete inorganic PSC based on $CsPb_{0.8}Ba_{0.2}I_2Br$ film. The scale bar is 500 nm. (b) $J-V$ performance of $CsPb_{1-x}Ba_xI_2Br$ ($x = 0$ to 0.4) based inorganic PSCs. (c) $J-V$ performance of $CsPb_{0.8}Ba_{0.2}I_2Br$ -based inorganic PSCs with high V_{oc} measured under 100 mW cm^{-2} irradiation. (d) SPO and steady state J_{sc} of the $CsPb_{0.8}Ba_{0.2}I_2Br$ -based PSCs; (e) IPCE and integrated J_{sc} of the $CsPb_{0.8}Ba_{0.2}I_2Br$ -based PSCs. 38
- Figure 3.4. Non-radiative recombination analysis.** (a) TRPL spectra of $CsPbI_2Br$ and $CsPb_{0.8}Ba_{0.2}I_2Br$ inorganic perovskite films. (b) Pb 4f spectra from XPS surface analysis of $CsPbI_2Br$ and $CsPb_{0.8}Ba_{0.2}I_2Br$ perovskite films. (c) EL measured during a $J-V$ sweep from 0 to 1.6 V (1.4 V for $CsPbI_2Br$ -based PSCs) and back with a rate of 10 mV s^{-1} 39

Figure 3.5. Phase segregation analysis. (a) ^{133}Cs echo-detected solid-state MAS NMR spectra at 21.1 T, 298 K and 24 kHz MAS of bulk mechanochemical compositions (I) CsPbBr_3 , (II) $\text{CsPb}_{0.8}\text{Ba}_{0.2}\text{Br}_3$ (note that the formula designates the formal stoichiometry and does not correspond to a pure-phase material), (III) $\text{CsBr} + \text{PbBr}_2$ (1:2), (IV) $\text{CsBr} + \text{PbBr}_2$ (4:1), (V) neat CsBr , (VI) $\text{CsBr} + \text{BaBr}_2$ (2:1), (VII) $\text{CsBr} + \text{BaBr}_2$ (1:2). Asterisks indicate spinning sidebands. The 200 to 350 ppm range in panels a and b is magnified 8 times to evidence the impurity phase. The inset in panel b shows a small amount of a barium-based non-perovskite impurity phase. (b) (I) A simulated NMR spectrum using EFG parameters calculated by fully-relativistic DFT for Ba incorporated on a B-site of CsPbBr_3 . (II) ^{137}Ba echo-detected (CT-selective) solid-state MAS NMR spectrum at 21.7 T, 298 K and 20 kHz MAS of the bulk mechanochemical $\text{CsPb}_{0.8}\text{Ba}_{0.2}\text{Br}_3$ compositions. Similarly, no signal was detected with a non-selective echo. 42

Figure 3.6. Phase segregation analysis. (a) The fractional iodide concentration and barium concentration vs. the experimental band gaps. The linear fits are included in the figure. (b) XRD patterns of $\text{CsPbI}_{2.27}\text{Br}_{0.73}$ and $\text{CsPb}_{0.8}\text{Ba}_{0.2}\text{I}_2\text{Br}$ perovskite films. J - V performance of (c) $\text{CsPbI}_{2.27}\text{Br}_{0.73}$ and (d) $0.8\text{CsPbI}_2\text{Br}-0.2\text{CsI}$ based inorganic PSCs under 100 mW cm^{-2} irradiation. (e) J - V curves of CsPbI_2Br based PSCs with different amount of BaI_2 as additive (Measurement was conducted under 100 mW cm^{-2} illumination with active area of 0.16 cm^2). (f) PL spectra of CsPbBr_3 inorganic perovskite films with and without barium. 44

Figure 3.7. Phase segregation analysis. (a) Dependence of the calculated band gaps of the Ba-doped CsPbI_2Br perovskites $\text{CsPb}_{1-x}\text{Ba}_x\text{I}_2\text{Br}$ on the barium concentration ($x = 0.03375, 0.0625, 0.125$) with first-principles density functional theory approach assumed that barium was doped into the perovskite lattice. The lowest energy structure of $\text{CsPb}_{1-x}\text{Ba}_x\text{I}_2\text{Br}$ was used for the calculations. The dot line represents linear fitting of the data. (b) Calculated formation energies of the alloyed perovskite $\text{CsPb}_{1-x}\text{Ba}_x\text{I}_2\text{Br}$ ($x = 0, 0.1, 0.2, 0.3, 0.4, 1$) by using the special quasirandom structure to mimic random disorder within a 200 atom supercell. 45

Figure 3.8. Phase segregation analysis. (a) an SEM image of a selected perovskite film area, the scale bar is 500 nm. Elemental distributions of $\text{CsPb}_{0.8}\text{Ba}_{0.2}\text{I}_2\text{Br}$ inorganic perovskite film by EDS elemental mapping are shown as: (b) distribution of Pb, (c) distribution of I, (d) distribution of Ba, (e) distribution of Br and (f) distribution of Cs. The scale bars are 500 nm. 46

Figure 3.9. Perovskite film morphology. SEM images of $\text{CsPb}_{1-x}\text{Ba}_x\text{I}_2\text{Br}$ with different incorporation amount of Ba (from a to e: $x = 0, 0.1, 0.2, 0.3, 0.4$). The scale bars are

500 nm.	47
Figure 3.10. Device stability. Stability of the unencapsulated CsPbI ₂ Br and CsPb _{0.8} Ba _{0.2} I ₂ Br based PSCs under 100 mW cm ⁻² continuous irradiation.....	48
Figure 4.1. Statistics of high-performance PSCs in recent literatures. a-d, PCE (a, c) and V_{oc} (b, d) of PSCs without organic residues or modification in perovskite layers and wide band gap (1.72 eV-2.3 eV) organic-inorganic hybrid PSCs and our devices. The dashed lines were drawn according to Shockley-Queisser theory. ¹¹ (ref. Shockley, W., and Queisser, H.J. (1961). Detailed balance limit of efficiency of p-n junction solar cells. J. Appl. Phys. 32, 510-519.)	55
Figure 4.2. Morphology, structure and photoelectric performance. (a, b) Top-view scanning and cross-sectional scanning electron microscopy (SEM) images of control CsPb(I _{0.75} Br _{0.25}) ₃ film and device, respectively. Scale bar = 1 μ m for (a), and scale bar = 500 nm for (b). (c) the current density–voltage (J - V) curves of control and CsPb(I _{0.75} Br _{0.25}) ₃ -0.5FAOAc devices. The inset shows the stabilized power output (SPO) of the CsPb(I _{0.75} Br _{0.25}) ₃ -0.5FAOAc device for 240 s. (d, e) Top-view and cross-sectional SEM images of CsPb(I _{0.75} Br _{0.25}) ₃ -0.5FAOAc film and device, respectively. Scale bar = 1 μ m for (d), and scale bar = 500 nm for (e). (f) X-ray diffraction (XRD) spectra of annealed control and CsPb(I _{0.75} Br _{0.25}) ₃ -0.5FAOAc films. (g), J–V curves for a meso-device of CsPb(I _{0.75} Br _{0.25}) ₃ -0.5FAOAc measured by forward (short circuit → open circuit) and reverse (open circuit → short circuit) scans. Measurement was conducted under 100 mW cm ⁻² illumination with active area of 0.16 cm ² . (h) Incident photon-to-current conversion efficiency of a CsPb(I _{0.75} Br _{0.25}) ₃ -0.5FAOAc device (black) and the integrated short-circuit current density (red). (i-l) Statistics of PCE, V_{oc} , J_{sc} , and FF of the control devices (32 samples) and the IPE devices (46 samples) in mesoscopic structure.	57
Figure 4.3. Charge transfer properties. (a, b) Time-resolved photoluminescence spectra of control and IPE films on glass and meso-TiO ₂ substrates, respectively. (c) Electrochemical impedance spectroscopy (EIS) spectra (Nyquist plots) of control and IPE devices with bias voltage of 1 V under dark, the frequency range is 100 kHz to 0.1 Hz. (d) Recombination resistances under different bias voltage under dark derived from Nyquist plots for control and IPE devices. A simplified equivalent circuit (inset) with one resistance (R_l) and a resistance (R_{rec})–capacitance (C_l) in series where the latter R – C component, assigned to a low frequency range, was used to estimate the recombination resistance at meso-TiO ₂ /perovskite interfaces.	58
Figure 4.4. Characterizations of intermediate phase engineering (IPE) process by nuclear magnetic resonance (NMR) measurements. (a) Solid-state magic angle	

spinning (MAS) nuclear magnetic resonance (NMR) characterization of the materials. Echo-detected ^{133}Cs spectra at 21.1 T, 298 K and 20 kHz MAS of (I) CsPbBr_3 , (II) $\text{Cs}_{0.95}\text{FA}_{0.05}\text{PbBr}_3$, (III) $\text{Cs}_{0.90}\text{FA}_{0.10}\text{PbBr}_3$, (IV) $\text{Cs}_{0.75}\text{FA}_{0.25}\text{PbBr}_3$, (V) $\text{Cs}_{0.50}\text{FA}_{0.50}\text{PbBr}_3$, (VI) $\text{CsPbBr}_3\text{-}0.5\text{Pb(OAc)}_2$, (VII) CsOAc , (VIII) Initial $\text{CsPbBr}_3\text{-}0.5\text{FAOAc}$, (IX) Annealed $\text{CsPbBr}_3\text{-}0.5\text{FAOAc}$. The dagger symbol (\dagger) indicates an impurity. (b) MAS NMR characterization of the materials. Echo-detected ^{133}Cs spectra at 11.74 T, 298 K and 20 kHz MAS of CsOAc and $\text{Cs}_{0.80}\text{FA}_{0.20}\text{OAc}$. (c) Liquid-state ^1H spectra at 9.4 T and 298 K of (I) neat FAOAc in DMSO-d_6 , (II) the evaporated component formed during annealing at 280 °C of $\text{CsPbBr}_3\text{-}0.5\text{FAOAc}$, dissolved in DMSO-d_6 . The chemical shifts are as follows: (I) Ac (1.6 ppm), -OH/ NH_2 (3.5 ppm), CH (7.7 ppm), (II) Ac (1.7 ppm), -OH/ NH_2 (3.4 ppm), CH (7.7 ppm). The spectrum was referenced to the residual DMSO signal at 2.50 ppm (quintet). (d) Solid-state MAS NMR characterization of the materials. Echo-detected ^1H MAS NMR spectra at 21.1 T, 298 K and 20 kHz MAS of (I) neat FAOAc , (II) initial $\text{CsPb(I}_{0.75}\text{Br}_{0.25})_3\text{-}0.5\text{FAOAc}$ powder from solution process, (III) annealed $\text{CsPb(I}_{0.75}\text{Br}_{0.25})_3\text{-}0.5\text{FAOAc}$ powder from solution process. The dashed line is the spectrum magnified 45-fold to show the trace residual protons in the sample..... 60

Figure 4.5. Characterizations of intermediate phase engineering (IPE) process. (a) X-ray diffraction spectra of the initial $\text{CsPb(I}_{0.75}\text{Br}_{0.25})_3$ and $\text{CsPb(I}_{0.75}\text{Br}_{0.25})_3\text{-}0.5\text{FAOAc}$ films. (b, c) The real-space distribution of difference charge density at the interfaces for $\text{CsPb(I}_{0.75}\text{Br}_{0.25})_3/\text{TiO}_2$ (c) and $\text{Cs}_{0.5}\text{FA}_{0.5}\text{Pb(I}_{0.75}\text{Br}_{0.25})_3/\text{TiO}_2$ (d). The corresponding binding energies are -0.966 meV/\AA^2 and -1.313 meV/\AA^2 , respectively. 62

Figure 4.6. Characterizations of IPE process. Cross-sectional SEM images of initial control (a) and IPE (b) films. Scale bar = 500 nm. (c) Schematic illustration of the IPE process. 63

Figure 4.7. Volatile salts with different cations. (a-c) Top-view SEM images of the annealed $\text{CsPb(I}_{0.75}\text{Br}_{0.25})_3$ films with volatile salts of 0.5MAOAc, 0.5NH₄OAc, and 0.5BAOAc, respectively. Scale bar = 1 μm . (d-f) Cross-sectional SEM images of the $\text{CsPb(I}_{0.75}\text{Br}_{0.25})_3\text{-}0.5\text{MAOAc}$, $\text{CsPb(I}_{0.75}\text{Br}_{0.25})_3\text{-}0.5\text{NH}_4\text{OAc}$, and $\text{CsPb(I}_{0.75}\text{Br}_{0.25})_3\text{-}0.5\text{BAOAc}$ devices, respectively. Scale bar = 500 nm. The yellow dashed boxes show the perovskite/metal oxide interfaces. (h) J - V curves of the $\text{CsPb(I}_{0.75}\text{Br}_{0.25})_3\text{-}0.5\text{MAOAc}$, $\text{CsPb(I}_{0.75}\text{Br}_{0.25})_3\text{-}0.5\text{NH}_4\text{OAc}$, $\text{CsPb(I}_{0.75}\text{Br}_{0.25})_3\text{-}0.5\text{BAOAc}$ and $\text{CsPb(I}_{0.75}\text{Br}_{0.25})_3\text{-}0.5\text{FAI}_{0.26}\text{Br}_{0.74}$ devices, respectively. (i) Solid-state MAS NMR characterization of the materials. Echo-detected ^{133}Cs spectra at 21.1 T, 298 K and 20 kHz MAS of CsPbBr_3 , $\text{Cs}_{0.5}\text{MA}_{0.5}\text{PbBr}_3$, $\text{Cs}_{0.9}(\text{NH}_4)_{0.1}\text{PbBr}_3$, $\text{Cs}_{0.9}\text{BA}_{0.1}\text{PbBr}_3$. (j)

XRD spectra of the initial perovskite films of $\text{CsPb}(\text{I}_{0.75}\text{Br}_{0.25})_3$, and with 0.5MAOAc, 0.5 NH_4OAc , and 0.5BAOAc on meso- TiO_2 .

Figure 4.8. $\text{CsPb}(\text{I}_{0.75}\text{Br}_{0.25})_3$ -0.5 $\text{FAI}_x\text{Br}_{1-x}$. (a) Ultraviolet-visible (UV-Vis) spectra of the control and $\text{CsPb}(\text{I}_{0.75}\text{Br}_{0.25})_3$ -0.5 $\text{FAI}_x\text{Br}_{1-x}$ films with $x = 0, 0.2, 0.4, 0.6, 0.8, 1.0$. (b) The band gaps (E_g) of $\text{CsPb}(\text{I}_{0.75}\text{Br}_{0.25})_3$ -0.5 $\text{FAI}_x\text{Br}_{1-x}$ has a linear correlation with FAI content x . (c) UV-Vis spectra of the control and the $\text{CsPb}(\text{I}_{0.75}\text{Br}_{0.25})_3$ -0.5 $\text{FAI}_{0.26}\text{Br}_{0.74}$ films. (d) XRD spectra of annealed perovskite films of the control, and with volatile salts of 0.5FABr, 0.5FAI, and 0.5 $\text{FAI}_{0.26}\text{Br}_{0.74}$ on meso- TiO_2 . (e) Top-view SEM images of the annealed $\text{CsPb}(\text{I}_{0.75}\text{Br}_{0.25})_3$ -0.5 $\text{FAI}_{0.26}\text{Br}_{0.74}$ film. Scale bar = 1 μm . (f) Cross-sectional SEM images of the $\text{CsPb}(\text{I}_{0.75}\text{Br}_{0.25})_3$ -0.5 $\text{FAI}_{0.26}\text{Br}_{0.74}$ devices. Scale bar = 500 nm..... 65

Figure 4.9. PSCs of planar SnO_2 structure. (a, d) Top-view SEM images of the control and the $\text{CsPb}(\text{I}_{0.75}\text{Br}_{0.25})_3$ -0.5FAOAc perovskite films on compact tin oxide, respectively. Scale bar = 1 μm . (b,e) Cross-sectional SEM images of the control and the IPE $\text{CsPb}(\text{I}_{0.75}\text{Br}_{0.25})_3$ -0.5FAOAc films in planar structure, respectively. Scale bar = 500 nm. The yellow dashed boxes show the perovskite/metal oxide interfaces. (c,f) J - V curve of the control and champion IPE devices in planar structure, respectively. The inset in (f) shows the SPO of the IPE device for 240 s. (g) Electroluminescence quantum efficiency as a function of injection current. (h) Photoluminescence spectra of control and IPE films on glass substrates, on compact SnO_2 substrates, on glass substrates with a spiro-OMeTAD top layer, and in devices, respectively. 67

Figure 4.10. Stability. (a) The evolution of photographs over time of the annealed $\text{CsPb}(\text{I}_{0.75}\text{Br}_{0.25})_3$ and $\text{CsPb}(\text{I}_{0.75}\text{Br}_{0.25})_3$ -0.5FAOAc films in ambient condition. The relative humidity is around 40%, and the room temperature is $298 \pm 5\text{K}$. (b) Electroluminescence stability tests of control and IPE PSCs in planar structure. (c) Evolution of the power conversion efficiency (PCE) over time of an unencapsulated $\text{CsPb}(\text{I}_{0.75}\text{Br}_{0.25})_3$ -0.5FAOAc based perovskite solar cell under 100 mW cm^{-2} continuous irradiation. 68

Figure 5.1. Phase transformation of CsPbI_3 film with different additives. Digital pictures (a), X-ray diffraction spectra (XRD) (b), and UV-Vis spectra (c) of the annealed films of pure CsPbI_3 and with 1:1 mole ratio of NH_4I , BAI, MAI, FAI, and DMAI additives in precursor solutions, respectively. 78

Figure 5.2. Phase transformation of CsPbI_3 films with additives of different ratios. Digital photos (a) and XRD spectra of MAI (b), FAI (c), and DMAI (d), respectively. 79

Figure 5.3. XRD spectra of CsPbI₃ film with BAI and NH₄I additives, the mole ratio is 1:2. The insets are corresponding digital photos of annealed films.....	79
Figure 5.4. Digital photos of the phase transformation processes of pure CsPbI₃ and with 1:1 mole ratio of NH₄I, BAI, MAI, FAI, and DMAI in precursor solutions, respectively. The films were annealed with a gradient temperature at 80 °C for 2 min and 330 °C for 5 min.	81
Figure 5.5. XRD spectra of the phase transformation processes of pure CsPbI₃ and with 1:1 mole ratio of NH₄I, BAI, MAI, FAI, and DMAI in precursor solutions, respectively. The films were annealed with a two-step temperature at 80 °C for 2 min and 330 °C for 5 min.	81
Figure 5.6. Performance of devices and film Morphology. (a) Cross-sectional SEM images of the CsPbI₃-DMAI device. Scale bar = 500 nm. (b) <i>J-V</i> curves of the CsPbI₃ devices with MAI, FAI, and DMAI additives, respectively. (c) <i>J-V</i> curve of champion CsPbI₃-DMAI device. The inset shows the SPO of the device for 260 s. (d-e) Top-view SEM images of the annealed CsPbI₃ films with MAI, FAI, and DMAI additives, respectively. Scale bar = 2 μm.....	82

List of Tables

Table 2.1 Photovoltaic parameters of perovskite solar cells fabricated using CsPbI ₂ Br doped with europium, measured at 100 mW·cm ⁻² light intensity.....	22
Table 3.1 Photovoltaic parameters of CsPb _{1-x} Ba _x I ₂ Br ($x = 0$ to 0.4) based inorganic PSCs. These PSCs were illuminated under 100 mW cm ⁻² simulated sunlight.....	38
Table 4.1: ¹³³ Cs shifts and peak widths of the spectra reported in Figure 4.4 and Figure 4.7.	61
Table 4.2. The amounts of reagents taken into the synthesis for mechanosynthesis for NMR measurements.	73
Table S1.1 Perovskite materials, optimization and photovoltaic parameters of lead-based perovskite solar cells.	87
Table S3.1. DFT calculated ¹³³ Cs chemical shieldings and referenced chemical shifts of the CsBaPbBr ₃ clusters.	93
Table S4.1. Perovskite materials, band gaps and photovoltaic parameters of reported highly efficient inorganic perovskite solar cells without organic residues or modification in perovskite layers and wide band gap (1.72 eV-2.3 eV) organic-inorganic hybrid perovskite solar cells and our devices.	96

List of Abbreviations

0D	zero dimensional
2D	two-dimensional
3D	three-dimensional
ATS	antisolvent treatment
BA	butylammonium
CHI	choline iodine
c-TiO ₂	compact-TiO ₂
DMA	dimethylammonium
DMF	dimethylformamide
DMSO	dimethylsulfoxide
DSSC	Dye-sensitive solar cells
E _g	band gap
EIS	electrochemical impedance spectroscopy
ETL	electron-transport layer
FA	formamidinium
FF	fill factor
FTO	fluorine-doped oxide
GAT	gradient thermal annealing
HAADF STEM	high-angle annular dark-field scanning transmission electron microscopy
IPA	isopropanol

List of Abbreviations

IPCE	incident photon-to-current conversion efficiency
J_{sc}	short-circuit current
$J-V$	current density-voltage
MA	methyllumonium
MAS	magic angle spinning
MeOAc	Methyl acetate
Meso-	mesoscopic
NMR	nuclear magnetic resonance
OAc	acetate
OIHP	organic-inorganic hybrid perovskite
OLAM	oleylammonium
PCE	power conversion efficiency
PEO	poly(ethylene oxide)
PL	photoluminescence
PSC	perovskite solar cells
PTABr	phenyltrimethylammonium bromide
PTACl	phenyltrimethylammonium chloride
PVP	poly-vinylpyrrolidone
QD	Quantum-dot
RT	room temperature
SCG	solvent-controlled growth
spiro-	2,2',7,7'-tetrakis(N,N-di-p-methoxyphenyl-amine)-9,9'-

List of Abbreviations

OMeTAD	spirobifluorene
SPO	stabilized power output
S-Q	shockley-Queisser
ss	solid-state
t	tolerance factor
TRPL	time-resolved photoluminescence
V_{oc}	open-circuit voltage
XPS	x-ray photoelectron spectroscopy
XRD	x-ray diffraction
μ GR	micrometer-sized graphene

Contents

Abstract	i
Keywords:	ii
Resume	错误!未定义书签。
Mots-clés:	错误!未定义书签。
List of Figures	v
List of Tables	xiii
List of Abbreviations	xiv
Chapter 1 Introduction.....	1
1.1 Perovskite solar cells	1
1.2. The materials and properties of lead-based halide inorganic perovskites	2
1.2.1 CsPbI ₃ and its derivatives	2
1.2.2 CsPbBr ₃ and its derivatives	3
1.2.3 CsPbI _{3-x} Br _x	3
1.3 Formation of 3D lead-based inorganic perovskite films	4
1.3.1 One-step method.....	4
1.3.2 Two-step method	10
1.4. Stabilization of 3D inorganic perovskite phases	11
1.4.1 Composition regulation or element doping	11
1.4.2 Nanocrystals	14
1.4.3 Organic modulation	15
1.4.4 Surface passivation.....	15
1.5 Thesis objective and outline	16
Chapter 2 Europium-doped CsPbI ₂ Br for stable and highly efficient inorganic perovskite solar cells.....	19
2.1 Introduction	20
2.2 Results and discussion.....	21
2.2.1 The performance of perovskite solar cells.....	21

2.2.2 Structure characterization of europium-doped CsPbI ₂ Br	23
2.2.3 Morphology and optical characterizations of perovskite films	25
2.2.4 Optoelectronic characterization of devices.....	26
2.2.5 Stability characterization of perovskite films and PSCs.....	28
2.3 Summary	29
2.4 Experimental section	30
2.4.1 Preparation method.....	30
2.4.2 Characterization.....	30
Chapter 3 Ba-induced phase segregation and band gap reduction in mixed-halide CsPbI ₂ Br for inorganic perovskite solar cells	34
3.1 Introduction	35
3.2 Results and discussion.....	36
3.2.1 Perovskite materials characterizations and photovoltaic performance of devices	36
3.2.2 Phase segregation analysis	40
3.2.3 Perovskite film morphology and device stability	46
3.3 Summary	48
3.4 Experimental section	48
3.4.1 Preparation method.....	48
3.4.2 Characterization.....	49
Chapter 4 Intermediate phase enhances inorganic perovskite and metal oxide interface for efficient photovoltaics	53
4.1 Introduction	54
4.2 Results and discussion.....	55
4.2.1 Film morphology and photoelectric performance	55
4.2.2 Characterization of the IPE process.....	58
4.2.3 Volatile salts with different cations and anions	63
4.2.4 PSCs on planar structure	66
4.3 Summary	69

4.4 Experimental section	69
4.4.1 Preparation method.....	69
4.4.2 Characterization.....	71
Chapter 5 Intermediate phase promoting CsPbI ₃ γ -phase formation for efficient photovoltaics	76
5.1 Introduction	77
5.2 Results and discussion.....	78
5.2.1 Phase transformation of intermediate phase engineering	78
5.2.2 The process research of phase transformation.....	80
5.2.3 Performance and stability	82
5.3 Summary	82
5.4 Experimental section	83
5.4.1 Preparation method.....	83
5.4.2 Characterization.....	84
Chapter 6 Conclusion	85
6.1 Main results achieved in this thesis	85
6.2 Future development.....	86
Supplemental Information.....	87
References	99
Acknowledgements	110
Curriculum Vitae	112

Chapter 1 Introduction

1.1 Perovskite solar cells

Metal halide perovskites have attracted wide attention in solar cells, light emitting diodes and detectors, owing to their superior photoelectronic properties, such as long carrier diffusion length, broad tunability of bandgap energy (E_g), and strong light absorption capability.¹⁻⁷ The chemical formula of a typical three-dimensional (3D) halide perovskite is ABX_3 , where A refers to a monovalent cation, such as methylammonium ($CH_3NH_3^+$, MA^+), formamidinium ($HC(NH_2)_2^+$, FA^+), dimethylammonium ($(CH_3)_2NH_2^+$, DMA^+), Cs^+ or their mixtures, B represents a divalent cation such as Pb^{2+} , Sn^{2+} , Ge^{2+} or their mixtures, and X represents a halide ion such as I, Br, Cl or their mixtures.⁸ Empirically, the crystal structure of an ABX_3 compound is determined by the Goldschmidt tolerance factor t , defined as,

$$t = \frac{r_A + r_X}{\sqrt{2}(r_B + r_X)}$$

where r_A , r_B , and r_X are the ionic radii of the A-cation, B-cation, and X-anion, respectively. When t is between 0.8 and 1.0, the 3D perovskite structure is favored.

Solar cells employing perovskite absorbers have emerged from the field of dye-sensitized solar cells (DSSCs).^{1,9} In 2009, Miyasaka *et al.* have reported a PCE of 3.8% based on perovskite-sensitized solar cells with liquid electrolyte, where the $MAPbI_3$ and $MAPbBr_3$ are as absorbers.¹ But the liquid electrolyte dissolves or decomposes the perovskite absorbers, leading to the rapidly degrade of solar cells within a few minutes.^{1,4} In 2012, Park *et al.* and Snaith *et al.* developed the solid-state perovskite solar cells (PSCs) with the PCEs of 9% and 12% by employing (2,2(7,7)-tetrakis-(N,N-dimethoxyphenylamine) 9,9-(spirobifluorene)) (spiro-OMeTAD) as the hole transporter, respectively.^{3,4} Since then, organic-inorganic halide perovskites (OIHP) solar cells have drawn much research attention. Until now, the certified PCE of OIHP solar cells has increased to 25.2% in 2020.^{1,10} However, the intrinsic instability of OIHP materials, such as the degradation under thermal stress and presence of moisture, due to high volatility of organic components of MA or FA, is hindering the commercialization of OIHP solar cells.^{11,12}

By replacing the volatile organic cations with the inorganic cesium cation (Cs^+), the all-inorganic perovskites are emerging as alternative light-harvesting materials owing their comparable excellent photophysical properties (such as carrier mobility, charge lifetime, defect-tolerance, and diffusion lengths) to their OIHP counterparts as well as a better stability toward

light soaking and thermal stressing.^{12,13}

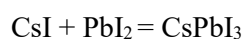
The performance of an inorganic PSC has undergone remarkable progress with the preparation of high-quality inorganic perovskite films and the stabilization of the three-dimensional phase in recent years, reaching a PCE of 19.02% with a long-term operational stability.¹⁴⁻¹⁶ The photovoltaic parameters, materials and the method of optimization in Pb-based PSCs are summarized in Table S1.1.

1.2. The materials and properties of lead-based halide inorganic perovskites

1.2.1 CsPbI₃ and its derivatives

Black-phase CsPbI₃ is the most typical and popular material in highly efficient inorganic PSCs. It has an E_g of 1.73 eV, which is the closest to the optimum value (1.35 eV) for a single-junction solar cell in lead-based inorganic halide perovskites.¹⁷ CsPbI₃ has three photoactive black phases, including cubic (α) phase (space group: $Pm\bar{3}m$), tetragonal (β) phase (space group: $P4/mbm$), and orthorhombic (γ) phase (space group: $Pbnm$) (Figure 1.1a).¹⁸ The α -phase of CsPbI₃ obtained under 360 °C transforms into the lower-symmetry β -phase under 260 °C and γ -phase under 175 °C with the increasing tilt of PbX₆ octahedra.¹⁹ At room temperature (RT), these desirable black phases spontaneously transform into a more thermodynamically stable “yellow” orthorhombic (δ) phase (space group: $Pnma$) with an E_g of 2.82 eV.²⁰ The phase instability of black CsPbI₃ mainly comes from the low t of 0.81, leading to large lattice distortion and instability of the octahedral perovskite structure.¹² However, the black CsPbI₃ perovskite film can be kept in RT after quenching. This results from substrate clamping-driven texture formation, which creates large biaxial strain to stabilize the black phase.²¹ The γ -CsPbI₃ is calculated to be a unipolar self-doped p-type material. The γ -CsPbI₃ is calculated to be a unipolar self-doped p-type material, which is different from MAPbI₃ that can change from intrinsic p-type to moderate and to n-type when its chemical potential is at Pb-poor, moderate, and Pb-rich conditions, respectively.^{22,23} γ -CsPbI₃ is also a defect-tolerant semiconductor due to the strong antibonding character of the valence band maximum.^{22,24,25} A mobility of $> 30 \text{ cm}^2 \text{ V}^{-1} \text{ s}^{-1}$, carrier lifetime of $\sim 10 \text{ }\mu\text{s}$, and carrier diffusion length of $\sim 1 \text{ }\mu\text{m}$ have been reported for CsPbI₃ films, which are comparable to those of OIHPs.^{26,27}

As a derivative of CsPbI₃, the zero-dimensional (0D) Cs₄PbI₆ (with a direct E_g of 3.44 eV) is often formed when the CsPbI₃ precursor solution contains excess CsI component during film formation process as follows:^{28,29}





1.2.2 CsPbBr₃ and its derivatives

CsPbBr₃ has a relative wide E_g of 2.3 eV, which has been applied for PSCs of high open circuit voltage (V_{oc}). It also has three photoactive perovskite phases, cubic α ($Pm3m$), tetragonal β ($P4/mbm$), and orthorhombic γ ($Pbnm$). The stable γ phase at RT can transform into β phase at 88 °C and α phase at 130 °C.³⁰ For an large 25 cm³ CsPbBr₃ single crystal, the carrier diffusion length, carrier lifetime, mobility and light absorption coefficient are as high as of 10 μm , 10.5 μs , 2000 cm² V⁻¹ s⁻¹ and 9.8×10^4 cm⁻¹, respectively, which are comparable with typical semiconductors such as GaAs, Si, and MAPbBr₃.³¹ For CsPbBr₃ films, carrier diffusion length of 82 ± 20 nm and carrier mobility of 77.9 cm² V⁻¹ s⁻¹ are reported.^{32,33}

Besides CsPbBr₃, its two derivatives, Cs₄PbBr₆ ($E_g = 3.76$ eV) and CsPb₂Br₅ (indirect E_g of 3.87 eV) have been investigated.^{34,35} Cs₄PbBr₆ exhibits a 0D structure based on the [PbBr₆]⁴⁻ octahedral framework separated by CsBr bridges. The CsPb₂Br₅ has a 2D layered structure, in which Cs⁺ cations are sandwiched between two layers of Pb-Br-coordinated polyhedrons.³⁶ The derivatives are formed with the following processes (Figure 1.1b)^{37,38}:



1.2.3 CsPbI_{3-x}Br_x

Introducing Br into CsPbI₃ to form mixed-halide inorganic perovskites CsPbI_{3-x}Br_x ($0 < x < 3$) can effectively increase the tolerance factor and therefore improve the phase stability. The E_g of CsPbI_{3-x}Br_x film increases with the increasing Br content (Figure 1c).³⁹⁻⁴¹ For CsPbI_{3-x}Br_x film with high Br content ($1.2 < x < 3$), light-induced phase segregation was observed (Figure 1.1d).⁴¹

CsPbI₂Br perovskite ($E_g = 2.05$ eV) is stable at RT while its phase segregates into I- and Br-rich phases under illumination.^{41,42} The I-rich phase mainly locates at grain boundaries, which accelerates ion migration. Mobile ions can pile up at the perovskite/TiO₂ interface, which forms injection barriers, hampers electron extraction and increases hysteresis in CsPbI₂Br-based PSCs.⁴²

CsPbI₂Br perovskite ($E_g = 1.92$ eV) has been extensively investigated as it neutralizes the stability and bandgap. The light-independence of ion migration and halide segregation has been reported for the CsPbI₂Br film.⁴³ The ion migration barrier for CsPbI₂Br perovskite is almost unchanged under dark (0.45 eV) and illumination (0.43 eV) conditions, while it reduces from

0.62 eV to 0.07 eV for MAPbI₃, which indicates the potential for long-term operation stability of inorganic PSCs.⁴³ Meanwhile, carrier mobility ranges from 5 to 15 cm² V⁻¹ s⁻¹ and charge carrier lifetime of 14 ns have been reported for CsPbI₂Br films.^{44,45}

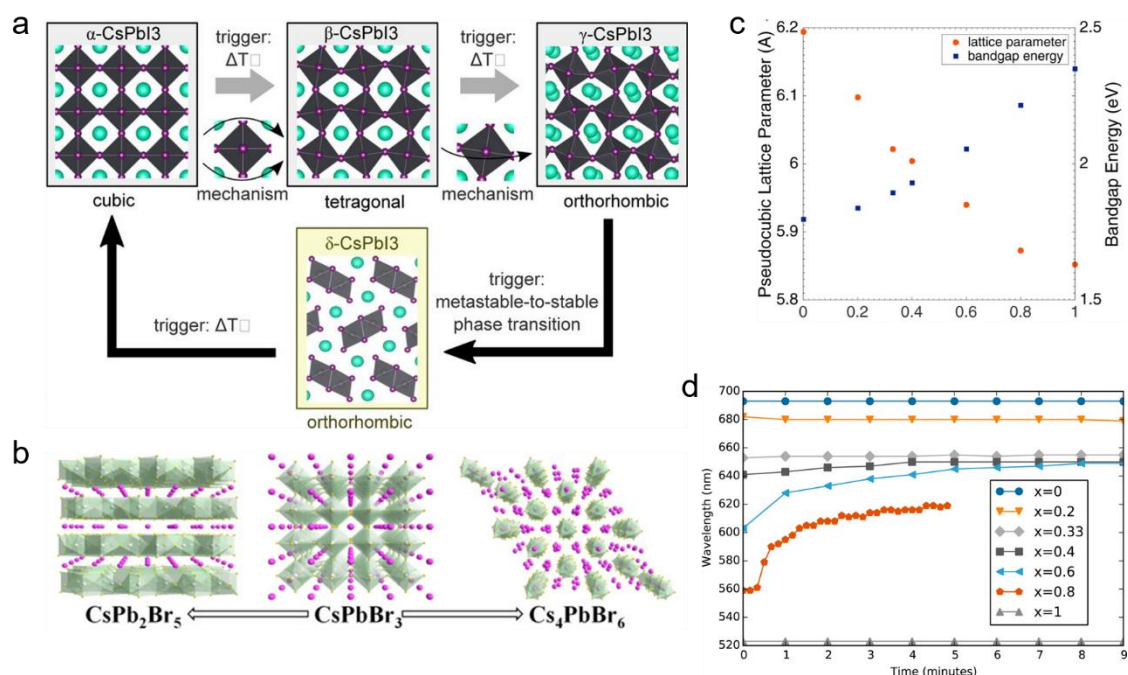


Figure 1.1. Structural properties of lead-based halide inorganic perovskites. (a) Crystal structure of the different phases for CsPbI₃ and their relative phase transitions.²¹ (b) Schematic crystal structures and transition of the inorganic CsPbBr₃ perovskite and its derivatives (CsPb₂Br₅, and Cs₄PbBr₆).³⁸ (c) Changes of lattice parameter and bandgap energy in CsPb(Br_xI_{1-x})₃ with increasing Br content.⁴¹ (d) Photoluminescent peak position as a function of time for CsPb(Br_xI_{1-x})₃ under ~1 sun illumination.⁴¹

1.3 Formation of 3D lead-based inorganic perovskite films

Formation of high-quality and pure 3D perovskite films is closely related to deposition strategies and is essential for highly efficient and stable inorganic PSCs. Here, the deposition technologies of inorganic perovskite films are classified as one-step and two-step methods depending on whether the deposition of PbX₂ and CsX (X = I, Br and Cl) precursors are synchronous or sequential.

1.3.1 One-step method

The one-step method includes one-step solution (spin-coating) method and co-vapor deposition. In the one-step solution method, we focus on the modulations of perovskite precursor solutions, residual solvent for the fresh films and annealing procedure for the formation of perovskite

films.

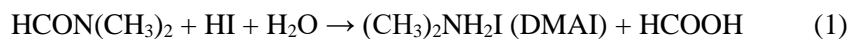
1.3.1.1 Modulations of perovskite precursor solutions

Modulations of perovskite precursor solutions mainly include changing the components of solutes and solvents. The solute modulations are composed by introducing the volatile additives to form the intermediate phase which changes the phase formation routine (named as intermediate phase engineering (IPE) hereafter), and adding non-volatile additives or element doping to improve the phase stability and adjust the formation of perovskite films (Details of the latter are shown in the section of Stabilization of 3D inorganic perovskite phases).

Intermediate phase engineering

By introducing volatile organic additives such as FAOAc, DMAI, MAI, into the CsPbX_3 precursor solutions, an OIHP intermediate phase is formed before annealing. The IPE is an emerging approach for formation of pure black phase CsPbI_3 and uniform film morphology.

Since the addition of hydriodic acid (HI) in a CsPbI_3 -dimethylformamide (DMF) precursor solution was reported to assist the formation of stable black phase CsPbI_3 films in 2015, HI additive or the so-called hydrogen lead iodide (“ HPbI_3 ”) precursor has been widely used for high-efficiency CsPbI_3 based solar cells.⁴⁶⁻⁴⁹ However, Ke *et al.* found that DMF and HI can react to generate DMAI (Reaction 1), and the so-called “ HPbI_3 ” is in fact DMAPbI_3 .⁵⁰



Thus, these as-formed CsPbI_3 perovskites annealed under less than 180 °C should be an organic-inorganic hybrid perovskite $\text{Cs}_{1-x}\text{DMA}_x\text{PbI}_3$, rather than an all-inorganic perovskite.^{50,51} Meanwhile, the PCE of $\text{Cs}_{0.7}\text{DMA}_{0.3}\text{PbI}_3$ PSCs has reached 12.62%.⁵⁰ Since then, the DMA^+ has been widely studied and used in inorganic perovskites. It has been verified by X-ray diffraction and solid-state nuclear magnetic resonance (ss-NMR) that DMA^+ can be doped into the MAPbBr_3 lattice up to 30 mol%, which leads to an increased E_g from 2.17 eV for MAPbBr_3 to ~2.23 eV for $\text{DMA}_{0.3}\text{MA}_{0.7}\text{PbBr}_3$.⁵² High-quality $\text{Cs}_{1-x}\text{DMA}_x\text{PbI}_3$ ($0 \leq x \leq 1$) perovskite films are prepared by varying the $\text{CsI}/\text{DMAPbI}_3$ ratio in precursor solutions. The optimized PCE of $\text{Cs}_{0.5}\text{DMA}_{0.5}\text{PbI}_3$ based PSCs is up to 14.3%, with over 85% of the initial efficiency retained after 20 days in air without encapsulation.⁵³ Crystalline β - CsPbI_3 film with an E_g of 1.68 eV was obtained by annealing the CsPbI_3 -DMAI fresh film at 210 °C for 5 min. The β - CsPbI_3 solar cells with choline iodide surface treatment is highly reproducible and stable with a PCE of 18.4%.¹⁵ It was further demonstrated that the final phase (β or γ) of annealed film at 210 °C is dependent on the concentration of DMAI precursor solutions. For example, CsPbI_3 -0.5DMAI and CsPbI_3 -0.75DMAI lead to the formation of γ - CsPbI_3 , while CsPbI_3 -

DMAI and CsPbI_3 -1.5DMAI promote the formation of β - CsPbI_3 .¹⁶ Meng et al. show that the CsPbI_3 -DMAI film annealed at 180 °C for 15min transforms into the thermodynamically stable $\text{DMA}_{0.15}\text{Cs}_{0.85}\text{PbI}_3$ ($E_g = 1.67$ eV) film with a small amount of Cs_4PbI_6 residue. It then transforms into γ - CsPbI_3 film and further spontaneously converts to δ - CsPbI_3 film with increasing annealing time (Figure 1.2). Meanwhile, γ - CsPbI_3 film can also be formed after annealing at 200, 220, 240 and 350 °C.⁵¹

MAI as an additive is also introduced into CsPbI_3 precursor solution. After annealing at 330 °C for 20 min in N_2 glove box, CsPbI_3 -MAI transforms into pure γ - CsPbI_3 film.⁵⁴ CsPbI_3 black perovskite film could also be obtained by annealing the precursor film ($\text{CsAc}+\text{MAI}+\text{PbI}_2$) under low crystallization temperature of 100 °C for 2 min.⁵⁵

Besides, the IPE strategy also promotes the formation of uniform and full-coverage films. An easy and scalable MA gas healing method for CsPbX_3 perovskite films by incorporating a certain amount of MAX ($X = \text{I}$ or Br) initiators into the initial film has been reported. MAX in CsPbX_3 initial films accelerated the absorption of MA gas and form a liquid intermediate phase, which leads to the formation of uniform and highly crystalline CsPbX_3 perovskite film after thermal annealing.⁵⁶ (Adamantan-1-yl) methan ammonium (ADMA) was reported to function as a soft template for controlling the nucleation and growth rate of CsPbI_3 crystals when it was introduced into precursor perovskite solution, which gives rise to a pinhole-free CsPbI_3 film with grain sizes on a micrometer scale after annealing under 350 °C.⁵⁷ The all-inorganic solar cell with the architecture fluorine-doped tin oxide (FTO)/ NiO_x / CsPbI_3 /ZnO/indium-doped tin oxide (ITO) exhibits a PCE of 16.04% and it retained 90% of the initial efficiency after 3000 h of continuous light soaking and heating.⁵⁷

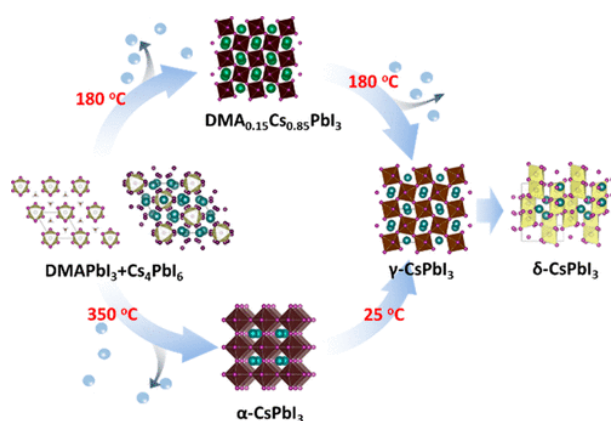


Figure 1.2. Intermediate phase engineering (IPE) for phase transformation. Chemical composition and phase evolution in dimethylammonium iodide (DMAI)-derived CsPbI_3 .⁵¹

Solvent modulation

In one-step solution deposition, dimethylsulfoxide (DMSO), DMF or their mixture are the most widely used solvents for inorganic perovskites. Compared to DMF, DMSO have stronger polarity, higher boiling point, stronger binding energy with Pb and high solubility of perovskites. A mixed DMSO/DMF solvent ($V_{\text{DMF}}:V_{\text{DMSO}} = 2:1$) retarded the perovskite crystallization process by forming CsI-PbX₂-DMSO intermediate phase and leads to the increase of CsPbI₂Br grain size from 100 nm to ~150-200 nm.^{58,59} Excessive or pure DMSO in the precursor solutions leads to the formation of pinholes in annealed films due to rapid evaporation of the large amount of residual DMSO during annealing. Finally, based on the optimized solvent, PSC with low temperature (100 °C) annealed CsPbI₂Br achieved PCE of 14.31% with over 90% of its original efficiency retained under continuous light soaking for 500 h in a N₂ glove box.⁵⁸ Lewis base adducts PbI₂(DMSO) and PbBr₂(DMSO) were used as precursors to slow down the crystallization for high-quality CsPbI₂Br films with large crystalline grains, flat surface, low defects, and long carrier lifetime. The PCE of CsPbI₂Br devices is up to 14.78%.⁶⁰

One-step solution processing of CsPbBr₃ is challenging due to the low solubility of CsPbBr₃ in most commonly used solvents. Recently, a novel precursor engineering strategy with cesium acetate (CsAc) and ionic liquid methylammonium acetate (MAOAc) has been developed to increase the concentration of CsPbBr₃ in precursor solution to 1.0 M. Uniform and pinhole-free CsPbBr₃ films with large-size crystalline grains are prepared. The champion CsPbBr₃ PSC achieves an efficiency of 7.37% with good stability, presenting negligible decay over a period of 1500 h under an ambient atmosphere (RH = 30-35%).⁶¹

1.3.1.2 Modulation of residual solvent

In one-step solution deposition, the fresh film obtained after spin-coating often contains DMSO residues. The fast evaporation of residual DMSO under high annealing temperature (160 °C, 280 °C or 350 °C) often leads to a rough surface and poor coverage with severe crystal aggregation.^{14,62} Modulation of residual solvent can effectively control the crystallization process for uniform films.

The fresh CsPbI_{3-x}Br_x films after spin-coating are rested tens of minutes before annealing in N₂ glove box (named as solvent-controlled growth (SCG) method) transforming into uniform and pinhole-free CsPbI_{3-x}Br_x films (Figure 1.3a-c) in 2018.¹⁴ The resting helps to remove most excess DMSO in fresh films and avoids the irregular growth and severe crystal aggregation of perovskite films during high-temperature annealing. A PCE of 15.7% is obtained for CsPbI₃ solar cells, which is the highest reported for inorganic PSCs at that time.¹⁴

Gradient thermal annealing (GAT) method has been used for uniform perovskite films with high-crystallinity.^{62,63} The low-temperature treatment slows down the evaporation of residual DMSO, avoids severe aggregation and triggers the crystallization of fresh perovskite films. The further high-temperature treatment leads to further evaporation of residual DMSO and elimination of unfavorable δ -phase, and promotes the further crystallization of the perovskite film.⁶²

Blowing the fresh inorganic perovskite film directly with dry-air (>100 °C air gun temperature) during spin-coating (named as dynamic hot-air casting process) accelerates the evaporation of excess DMSO and results in the formation of a uniform initial film consisting of PbX_2 -DMSO-CsI intermediate phase. It then transforms into a dense and highly crystallized CsPbI_2Br film after annealing at 280 °C. With this dynamic hot-air casting process, CsPbI_2Br -based cells (with 0.5mol% BaI_2) achieved PCE of 14.85% for small exposure area of 0.09 cm^2 and 13.78% for a large area of $1 \times 1\text{ cm}^2$.⁶⁴

Anti-solvent method is a popular deposition technology for forming inorganic perovskite films.^{62,65} The anti-solvents, such as diethyl ether, chlorobenzene, and toluene, can rapidly extract the residual DMSO molecules without dissolving inorganic perovskites and result in the formation of homogeneously dispersed inorganic perovskite films. A synergetic process of gradient thermal annealing and anti-solvent method was reported to precisely control the crystallinity process for high-quality film with a low root-mean-square roughness of 25.9 nm and an average grain size of $1\text{ }\mu\text{m}$ (Figure 1.3d). Isopropanol (IPA) is used as a green anti-solvent with proper volatility and viscosity to reduce the solvent edge effect compared to toluene. A champion PSCs with PCE of 16.07% (stabilized power output of 15.75%) and V_{oc} of 1.23 V is realized, which is the highest efficiency reported in CsPbI_2Br -based PSCs until now.⁶²

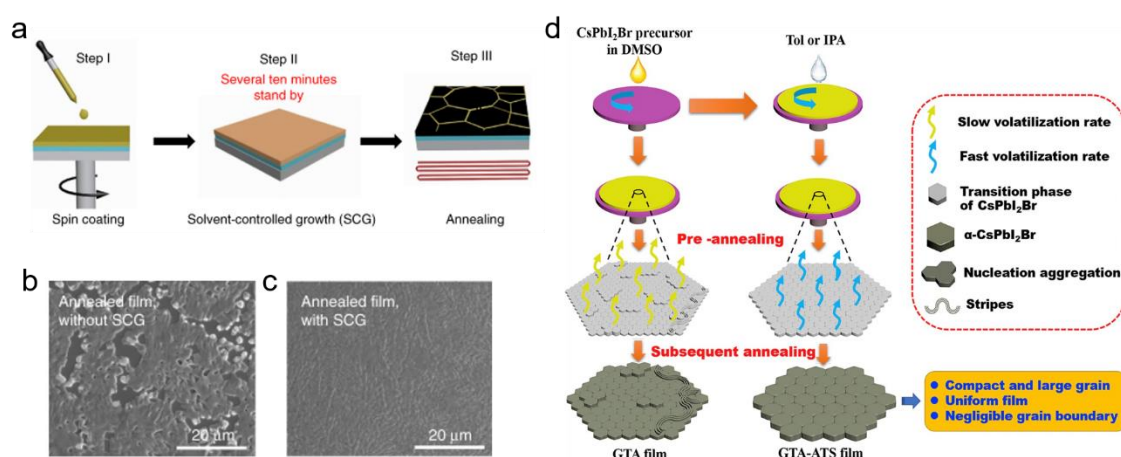


Figure 1.3. Residual solvent modulation for inorganic film formation. (a) Schematic illustration of CsPbI_3 -perovskite film formation procedures via solvent-controlled growth (SCG).¹⁴ SEM images of annealed

CsPbI₃ perovskite precursor films without (b) and with (c) SCG, respectively.¹⁴ Scale bar: 20 μm . (d) Schematic illustration of CsPbI₂Br perovskite crystallization process via gradient thermal annealing (GTA) alone or in synergetic with antisolvent treatment (ATS).⁶²

1.3.1.3 Modulation of annealing procedures: temperature, atmosphere and methods

The annealing temperature, atmosphere and methods greatly influence the phase formation, morphology and crystallinity of inorganic perovskite films.

With increasing annealing temperature, the CsPbI₂Br film transforms into a non-perovskite δ -phase at 100 $^{\circ}\text{C}$, mixed δ and black phases at 230 $^{\circ}\text{C}$, and a low-defect, uniform and pure black phase at 280 $^{\circ}\text{C}$ (Figure 1.4a). With excessive annealing temperature at 350 $^{\circ}\text{C}$, the CsPbI₂Br phase segregates into I- and Br-rich regions with some CsI or CsBr.⁶⁶

The PCE of CsPbI₂Br-based device fabricated in dry air glovebox is higher than that fabricated in N₂ glovebox (15.7% vs. 13.32%).⁶⁷ It is attributed to the dissociation of O₂ into O during the annealing which passivates halide vacancy through strong interaction with perovskite (Figure 4b-c).⁶⁷

Besides traditional annealing with a hotplate, a pulsed flash infrared annealing method was developed to fabricate uniform and highly crystallized CsPbI_xBr_(3-x) films by adjusting the flash pulses.⁶⁸ Low-temperature preparation of a black phase CsPbI₂Br film was also reported by a RT solvent (DMSO) vapor annealing treatment (Figure 1.4d).⁶⁹

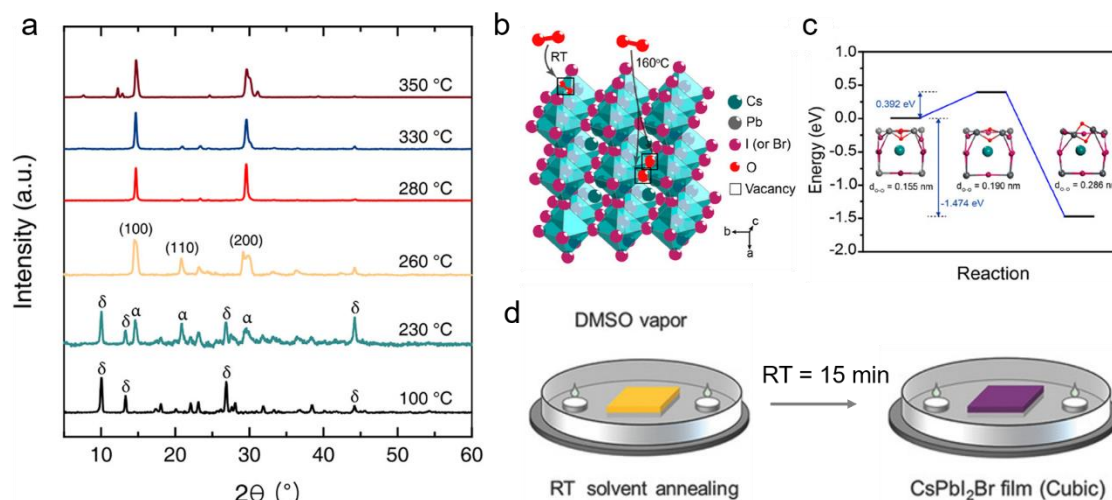


Figure 1.4. Modulation of annealing procedures for formation of inorganic perovskite films. (a) X-ray diffraction patterns of a CsPbI₂Br films annealed at different temperature ranging from 100 to 350 $^{\circ}\text{C}$.⁶⁶ (b) Schematic of adsorbed oxygen molecule passivation and oxygen atom passivation for inorganic perovskite. ⁶⁷ (c) Dissociation process of O₂ molecule at halide vacancy.⁶⁷ (d) Illustration of a CsPbI₂Br film with room temperature (RT) DMSO vapor annealing. ⁶⁹

1.3.1.4 Co-vapor evaporation

High-quality inorganic perovskite films, such as CsPbI₃, CsPbIBr₂ and CsPbBr₃, have been reported to be fabricated by co-evaporation of CsI, CsBr, PbBr₂ or PbI₂ precursors.⁷⁰⁻⁷² The co-evaporation method can precisely control the film thickness and benefit large-scale film fabrication with good uniformity and reproducibility.⁷⁰⁻⁷³

1.3.2 Two-step method

The two-step method refers to a sequential fabrication of PbX₂ film (by spin-coating or vapor deposition methods) and CsX film (by dipping into precursor solutions, two (or multi)-step spin-coating, or vapor deposition methods). As Br-rich inorganic perovskites, such as CsPbBr₃ and CsPbIBr₂, have low solubility in most solvents, two-step methods are widely applied for their fabrication.

In fabrication of CsPbBr₃ film by dipping method, as the low solubility of CsBr in methanol (<17 mg ml⁻¹) and the high formation enthalpy of CsPbBr₃, long dipping time (~15 min) and thermal assistance (~50 °C) during the dipping process are often necessary (Figure 1.5a).^{38,74,75} PSCs based on CsPbBr₃, CsPbIBr₂ and CsPb_{0.9}Sn_{0.1}IBr₂ films by the dipping method have achieved PCE of 6.7%, 8.25% and 11.33%, respectively.^{76,77} In recent, high-quality CsPbI₃ films with Br⁻ and In³⁺ doping were fabricated by the dipping method, and PSCs with a configuration of fluorine doped tin oxide (FTO)/compact TiO₂ (c-TiO₂)/mesoporous TiO₂ (m-TiO₂)/perovskite/carbon exhibited a large V_{oc} of 1.20 V and a remarkable PCE of 12.04%. The encapsulated PSC shows no degradation even after storage in ambient atmosphere for more than two months.⁷⁸

A multistep spin-coating method was reported to fabricate pure-phase CsPbBr₃ films (Figure 1.5b).³⁷ By tuning the spin-coating cycles (n) of CsBr methanol precursor solution (0.07M), the composition of the as-prepared film converts from CsPb₂Br₅ ($n \leq 3$) to CsPbBr₃ ($n = 4$) and Cs₄PbBr₆ ($n \geq 5$). When $n = 4$, a film with vertical- and monolayer-aligned grains was obtained. Upon interfacial modification with graphene quantum dots, a HTM-free all-CsPbBr₃ PSC achieved PCE of 9.72% and retained 87% of its initial efficiency under RH = 90% at 25 °C after over 130 days.³⁷

A sequential vapor deposition of PbI₂ and CsI powders was reported to form CsPbI₃ perovskite films. The obtained film has a mobility of 25 cm²V⁻¹s⁻¹ and a carrier lifetime of 10 μs, which are comparable with its OIHP counterpart.²⁶ A graded heterojunction device with a CsPbBr₃/CsPbBr₃-CsPb₂Br₅/CsPbBr₃-Cs₄PbBr₆ photosensitive layer was also fabricated by the sequential vapor deposition method (Figure 1.5c). It exhibits a PCE of 10.17% with excellent stability against humidity and heat.³⁸

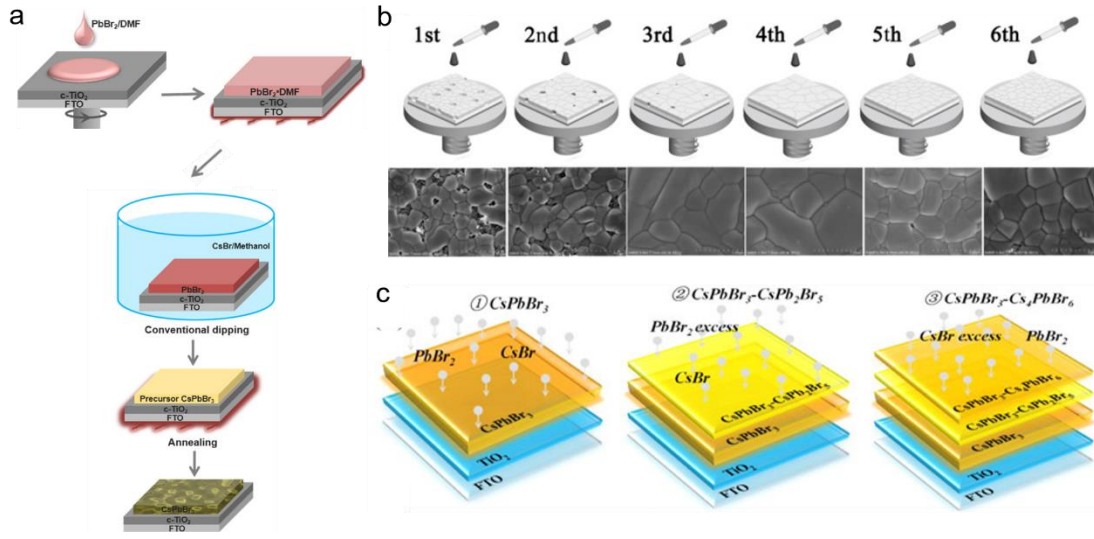


Figure 1.5. Two-step methods for fabrication of inorganic perovskite films. (a) Schematic process for fabrication of a CsPbBr₃ film by the dipping method.⁷⁹ (b) Multistep solution-processing deposition of CsBr on PbI₂ film and the corresponding top-view SEM images of the corresponding all-inorganic lead halide film.³⁷ (c) The procedure of CsPbBr₃ combining with CsPb₂Br₅ and Cs₄PbBr₆ derivative-phase films via the sequential vapor deposition method.³⁸

1.4. Stabilization of 3D inorganic perovskite phases

Regulation of tolerance factor, modulation of perovskite surface energy and formation of a surface capping layer by composition regulation (or element doping), nanocrystals formation, organic modulation and surface passivation are all effective to improve the 3D phase stability of inorganic perovskites.

1.4.1 Composition regulation or element doping

Increasing the r (A^+), or reducing the r (B^{2+}) and r (X^-) in the ABX₃ crystal structure will increase the relative low t of inorganic perovskites and therefore the phase stability. In fact, three possible scenarios can be used to depict element doping or composition regulation: (1) the dopants are incorporated into the crystal lattice, (2) the dopants promote the formation of low-dimensional perovskites (such as 2D), and (3) the dopants induce separate phases and modify the surface or grain boundaries of the perovskite crystals.

1.4.1.1 X-site

As mentioned previously, the smaller-size Br^- can substitute I^- in CsPbI_3 in any ratio to form $\text{CsPbI}_{3-x}\text{Br}_x$ alloys, which improves the perovskite black phase stability but also has an undesired blue shift of the absorption edge giving an the enlarged E_g for high-efficiency photovoltaics.⁴⁰ By replacing I^- with a pseudo halide SCN^- , a 2D $\text{Cs}_2\text{PbI}_2(\text{SCN})_2$ all-inorganic perovskite material with an E_g of 2.05 eV was obtained, showing an improved stability in comparison with CsPbI_3 .⁸⁰

1.4.1.2 A-site

As Cs is the largest nonradioactive element in Group IA of the periodic table, there is no suitable monovalent inorganic cation (larger than Cs^+) available for doping into perovskite lattice to increase the t . The organic molecular DMA^+ ($r = 0.272$ nm) was reported to be incorporated into the perovskite lattice to form $\text{Cs}_{1-x}\text{DMA}_x\text{PbI}_3$, which has increased t and stability in comparison with CsPbI_3 as mentioned in previous chapter.^{50,51,53}

Besides, layered Ruddlesden-Popper or Dion-Jacobson halide perovskite phases, so-called ‘quasi-2D’ perovskites, can be formed by introducing large organic cations into CsPbI_3 perovskite. BA^+ was introduced into CsPbI_3 to form a $\text{BA}_2\text{CsPb}_2\text{I}_7$ quasi-2D perovskite which shows increased phase stability against humidity and heat in comparison with CsPbI_3 .⁸¹ Ethylenediammonium diiodide (EDAI_2) was introduced into CsPbI_3 to form a 2D EDAPbI_4 perovskite which stabilizes the CsPbI_3 phase and avoids the undesired formation of δ -phase. The $\text{CsPbI}_3 \cdot 0.025\text{EDAPbI}_4$ film is stable at RT for months and can stand 100 °C for over 150 hours in dry box.⁴⁷ Phenylethylammonium iodide (PEAI) was introduced into CsPbI_3 precursor solution to form a quasi-2D $\text{PEA}_2\text{Cs}_{n-1}\text{Pb}_n\text{I}_{3n+1}$ perovskite ($1 \leq n \leq \infty$) (Figure 1.6a). The PCE of the device based on $n = 60$ perovskite reached 12.4% with much improved performance longevity.⁸²

Moreover, alkali metal cations (such as Rb^+ , K^+ , Na^+ and Li^+) doping into CsPbBr_3 perovskite have also been reported to improve the PCE of CsPbBr_3 -based PSCs.^{45,83}

1.4.1.3 B-site

Sn^{2+} exhibits similar chemical properties with Pb^{2+} and its ionic radius (118 pm) is slightly smaller than that of Pb^{2+} (119 pm). Thus, substituting Pb^{2+} with Sn^{2+} to form $\text{CsPb}_{1-x}\text{Sn}_x\text{X}_3$ ($\text{X} = \text{I}$ and Br) alloys can effectively increase t and adjust bandgaps.¹² A $\text{CsPb}_{0.9}\text{Sn}_{0.1}\text{IBr}_2$ film ($E_g = 1.79$ eV) prepared by the two-step method in ambient atmosphere shows a long-term stability in heat, moisture and air.⁷⁷ Moreover, the $\text{CsPb}_{1-x}\text{Sn}_x\text{IBr}_2$ ($x = 0, 0.25, 0.50, 0.75$, and 1.00) perovskite films present tunable E_g from 2.04 to 1.64 eV. The $\text{CsPb}_{0.75}\text{Sn}_{0.25}\text{IBr}_2$ -based device

shows a remarkable PCE of 11.53% and a high V_{oc} of 1.21 V with a much improved phase and illumination stability.⁸⁴ $\text{CsPb}_{0.6}\text{Sn}_{0.4}\text{I}_3$ ($E_g = 1.38$ eV) have been reported to exhibit improved phase stability compared to CsPbI_3 (Figure 1.6b-c).⁸⁵ $\text{CsPb}_{0.6}\text{Sn}_{0.4}\text{I}_3$ also shows better resistance to oxidation compared to its hybrid counterparts, as the smaller Cs^+ leads to stronger antibonding of Sn 5s with I 5p, which results in the smaller formation energy of Sn-defects in inorganic perovskites. With the functionalization of grain boundaries and surfaces by antioxidative $\text{SnF}_2 \cdot 3\text{FACl}$ and organic (aminomethyl) piperidinium diiodide ((4AMP) I_2), respectively, the $\text{CsPb}_{0.6}\text{Sn}_{0.4}\text{I}_3$ device achieved a PCE of 13.37% without obvious degradation in dry N_2 atmosphere at RT for over 2800 h.⁸⁵

Moreover, Mn^{2+} can be doped into CsPbBr_3 and CsPbCl_3 perovskite lattice up to at least 8 mol% and 3 mol%, respectively.⁸⁶ The incorporation of Mn^{2+} stabilizes the black phase of either CsPbX_3 film or CsPbX_3 nanocrystals, which promotes the improvement of PCE of solar cells.^{87,88}

Also, Sr^{2+} incorporation into CsPbI_2Br forms Sr-enriched surface of the perovskite film, which passivates the defects, stabilizes the perovskite phase of perovskite films and increases the PCE of devices.⁸⁹ Ni^{2+} and Cu^{2+} have also been introduced into CsPbI_2Br films to improve the PCE and stability of PSCs.^{90,91} Mg^{2+} , Ca^{2+} , Sr^{2+} and Ba^{2+} were reported to be introduced into CsPbBr_3 to enlarge grain sizes and suppressed formation of point defect (vacancies) within perovskite films.⁹²

Aliovalent Bi^{3+} (103 pm) could be doped into MAPbBr_3 and CsPbBr_3 crystals to narrow the E_g and improve the electrical conductivity.^{93,94} The incorporation of Bi^{3+} in CsPbI_3 have also been reported to reduce the E_g , and improve the phase stability, which may be a result from Bi^{3+} -induced the micro strain and slight distortion of perovskite structure.⁹⁵ The PCE of $\text{CsPb}_{0.96}\text{Bi}_{0.04}\text{I}_3$ based solar cells is up to 13.21% and it maintains 68% after 168 h under illumination in ambient condition without encapsulation. In^{3+} , Eu^{3+} and Sb^{3+} were also incorporated in CsPbI_2Br or CsPbI_3 respectively, to increase the phase stability of the films and the PCE of devices.^{78,96,97} Moreover, the lattice doping of lanthanide ions ($\text{Ln}^{3+} = \text{Sm}^{3+}$, Tb^{3+} , Ho^{3+} , Er^{3+} , and Yb^{3+}) into CsPbBr_3 films could increase grain size and prolong carrier lifetime. The PCE of $\text{CsPb}_{0.97}\text{Sm}_{0.03}\text{Br}_3$ based solar cells is up to 10.14% with V_{oc} of 1.594 V.⁹⁸

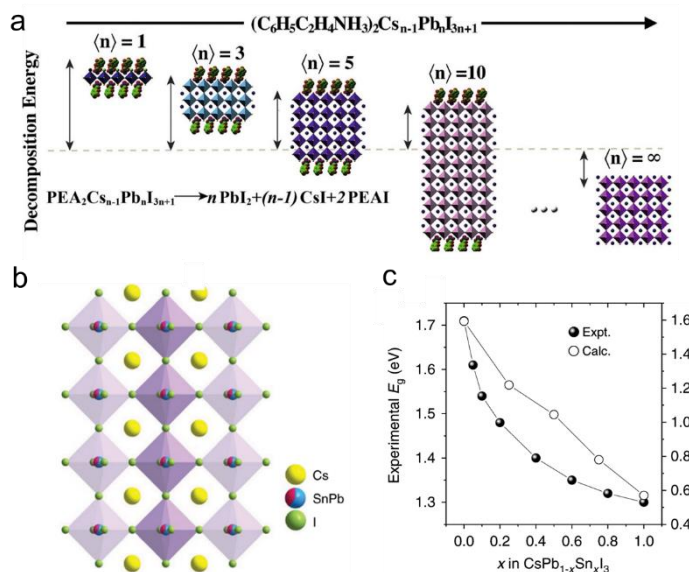


Figure 1.6. Element doping and composition regulation for stabilization of inorganic films. (a) Characteristics of Quasi-2D PEA₂Cs_{n-1}Pb_nX_{3n+1} perovskite films and decomposition energetics using first-principles density functional theory (DFT) of perovskite with different $\langle n \rangle$ values.⁸² (b) Schematic crystal structure of CsPb_{1-x}Sn_xI₃.⁸⁵ (c) Variation of experimental (solid circle) and calculated (open circle) bandgaps as a function of x in CsPb_{1-x}Sn_xI₃.⁸⁵

1.4.2 Nanocrystals

While bulk CsPbI₃ can easily transform into the yellow phase, black phase CsPbI₃ nanocrystals with size of 4 to 15 nm have been reported to be stable due to the large contribution of surface energy (Figure 1.7a).⁹⁹

During fabrication of perovskite nanocrystals, ligands play an important role as capping layers to protect them from segregation or coarsening into large-size nanocrystals. However, they may also block carrier transport to some extent. An α -CsPbI₃ quantum-dot (QD)-based device with a record PCE of 10.77% and a V_{oc} of 1.23 V was reported in 2016.⁹⁹ In fabricating α -CsPbI₃ QD film, the short methyl acetate (MeOAc) ligand was used to remove the long oleylammonium (OLAM) ligand, which effectively improves the carrier transport. The black phase CsPbI₃ QD film is stable for more than two months in ambient air.⁹⁹ Crosslinking micrometer-sized graphene (μ GR) to CsPbI₃ QDs can not only provide an effective channel for carrier transport, but also suppress the thermal or moisture-induced QD agglomeration. The PCE of μ GR/CsPbI₃ based solar cell is 11.4%.¹⁰⁰ The charge transport and mobility of CsPbI₃ QD films could be improved by tuning the coupling of QDs with A-site cation halide salts (AX, such as FAI, MAI, FABr, MABr and CsI) treatment. The PSC based on FAI treated CsPbI₃ QD film has a record certified efficiency of 13.43% with increased photocurrent.¹⁰¹

1.4.3 Organic molecule modulation

Long-chain ammonium cations, polymers and polar organic molecules have been introduced into perovskite precursor solutions. They improve the phase stability of inorganic perovskite films by reducing crystal grain size, forming passivation layer (or nanoscale encapsulation) or tuning the surface energy.

OLAM and phenylethylammonium additives in the precursor solution can act as surface capping ligands and lead to the formation of metastable bulk α - and β -CsPbI₃ films, respectively. On one hand, the ligands prevent grain growth and aggregation, and maintain the reduced grain size. On the other hand, they prevent the interaction of moisture and perovskite films. Thus, both black phase films remain intact after more than 4 months in ambient condition.¹⁰²

Polymers, such as poly-vinylpyrrolidone (PVP), was introduced into CsPbI₃ precursor solutions to synthesize extra-long-term stable CsPbI₃ perovskite films (Figure 1.7b-c). The acylamino groups of PVP induce electron cloud density enhancement on the surface of CsPbI₃, which lowers surface energy, and stabilizes black phase CsPbI₃. The CsPbI₃ PSC has a PCE of 10.74%, and it remained 75% of its origin efficiency under ambient condition for 500 h without encapsulation.¹⁰³ Moreover, adding a small quantity of poly(ethylene oxide) (PEO) to the CsPbI₃ precursor solution effectively promotes the formation of black phase at a low crystallization temperature, and inhibits the transformation into the yellow δ -phase. PEO effectively reduces the grain size during crystallization and enhances the phase stability for CsPbI₃ perovskite film. As the PEO chains are sequestered during crystal impingement, they may coordinate with the ionic surfaces of the CsPbI₃ grains, and therefore passivate the grain boundaries in the intergrain regions.¹⁰⁴

Sulfobetaine zwitterion added into the CsPbI₃ precursor solution impedes the crystallization of CsPbI₃ films via electrostatic interaction between zwitterion and PbI₂-DMSO colloids in precursor solution, and results in the formation of a CsPbI₃ film with average grain size of 30 nm. The PCE of solar cells based on zwitterion-stabilized CsPbI₃ film is up to 11.4%.¹⁰⁵

1.4.4 Surface passivation

Organic molecules, such as PEAI, Phenyltrimethylammonium bromide (PTABr), choline iodine (CHI), phenyltrimethylammonium chloride (PTACl), have been applied to improve the stability of inorganic perovskite film by forming a stable surface layer, or passivating the defects.

PEAI can act as a passivation layer on CsPbI₃ film and form a defect-passivating organic cation terminated surface, which improves phase stability and moisture resistance.¹⁰⁶ PTABr could enhance the phase stability of CsPbI₃ through simultaneous gradient Br doping and surface passivation of organic PTA cation (Figure 1.7d). PSCs based on PTABr treated CsPbI₃ is highly

reproducible with a champion efficiency of 17.06% and an SPO of 16.3%. It retains 91% of its initial PCE after being stored in a N_2 glovebox under continuous white light LED illumination for 500 h.¹⁰⁷ CHI as a surface layer is effective for mitigating the cracks and pinholes in the perovskite layer, and passivating the surface trap states, which leads to a better match of the energy levels between the β -CsPbI₃ perovskite and the TiO₂ electron-transport layer (ETL), as well as with the spiro-OMeTAD hole-transport layer. With this approach, the efficiency of β -CsPbI₃-based PSCs was improved to 18.4%.¹⁵ Recently, with optimal DMAI additive content and PTACl passivation, a PTACl-CsPbI₃ based inorganic PSCs with a champion efficiency of 19.03% was achieved, which is the record for inorganic PSCs until now.¹⁶

A graded E_g CsPbI_{2+x}Br_{1-x} perovskite solar cells with a stable CsPbI₃ QD film as a surface layer has been achieved. The stable CsPbI₃ QD film not only protects the black phase of CsPbI_{2+x}Br_{1-x}, but also achieves proper band-edge bending as a graded E_g for improved carrier collection.¹⁰⁸

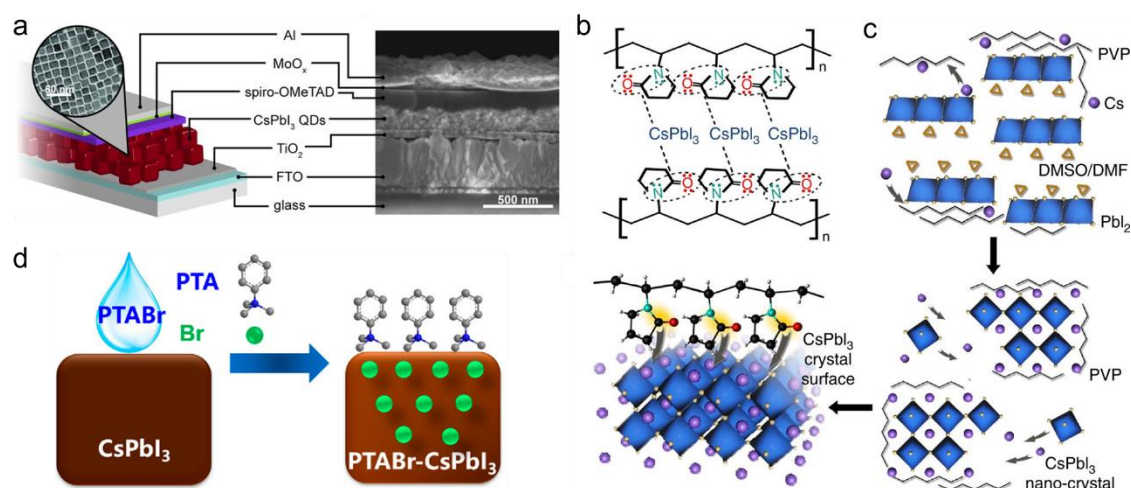


Figure 1.7. Nano crystallization, organic modulation, and surface passivation for stabilization of inorganic perovskite films. (a) Schematic (with TEM image of quantum dots (QDs)) and SEM cross-section of the QD-CsPbI₃ PV cell.⁹⁹ (b) Schematic diagram of the chemical bonding between CsPbI₃ and poly-vinylpyrrolidone (PVP) molecules. PVP molecule contains of long-chain alkyls and acylaminos. The unbounded lone pairs for nitrogen/oxygen (N/O) atoms in acylaminos offer excess electrons and interact with Cs ions in CsPbI₃.¹⁰³ (c) Mechanism and scheme for the formation of cubic phase CsPbI₃ with the assistant of PVP in three stages.¹⁰³ (d) Schematic illustration of gradient Br doping and phenyltrimethylammonium (PTA) organic cation passivation.¹⁰⁷

1.5 Thesis objective and outline

Although huge developments have been achieved for inorganic PSCs recently, the desirable narrow-bandgap inorganic perovskites (such as CsPbI₃ and CsPbI₂Br) are still suffering from the thermodynamic phase instability, as the photoactive black phase (α , β , or γ phase)

spontaneously transforms into a more thermodynamically stable yellow phase (δ -phase) in ambient condition. In the thesis, the stabilization of the black phase and the formation of high-quality perovskite films are studied for improving performance and stability of inorganic perovskite solar cells.

In the chapters 2 and 3, we show two roles of element doping for improving the phase stability of inorganic perovskite films.

In chapter 2, europium is incorporated into the CsPbI_2Br perovskite lattice, which improves the phase stability to 6 months in ambient condition. A maximum PCE of 13.71% for an inorganic PSC with the $\text{CsPb}_{0.95}\text{Eu}_{0.05}\text{I}_2\text{Br}$ perovskite is achieved with a stable power output of 13.34%. Meanwhile, the device retains 93% of the initial efficiency after 370 hours under $100 \text{ mW}\cdot\text{cm}^{-2}$ continuous white light illumination under maximum power point tracking measurement.

In chapter 3, we demonstrate that barium cannot be incorporated into the perovskite lattice but induce phase segregation, resulting in a change in the iodide/bromide ratio compared with the precursor stoichiometry and consequently a reduction in the band gap energy of the perovskite phase. The device with $\text{CsPb}_{0.8}\text{Eu}_{0.2}\text{I}_2\text{Br}$ film ($E_g = 1.86\text{eV}$) shows a PCE of 14.0% with a high open-circuit voltage of 1.33 V and an external quantum efficiency of electroluminescence of 10^{-4} .

In chapters 4 and 5, intermediate phase engineering is studied to improve the interfacial contact of inorganic perovskite and metal oxide transport layer, and promote the formation of CsPbI_3 perovskite phase for high-quality perovskite films.

In chapter 4, the effect of introduction of organic cation (such as methylammonium and formamidinium) salts into $\text{CsPb}(\text{I}_{0.75}\text{Br}_{0.25})_3$ is described where leads to the formation of an organic-inorganic hybrid perovskite intermediate phase, promoting a robust interfacial contact of inorganic perovskite and metal oxide through hydrogen bonding. A champion $\text{CsPb}(\text{I}_{0.75}\text{Br}_{0.25})_3$ -based device with a power conversion efficiency of 17.0% and an open-circuit voltage of 1.34 V was realized, implying that a record of over 65% of the Shockley-Queisser efficiency limit is achieved.

In chapter 5, according to the investigation of the phase transformation processes of pure CsPbI_3 with different additives, including NH_4I , BAI, MAI, FAI and DMAI, we found that the formation of a 3D organic-inorganic hybrid perovskite intermediate phase is essential for avoiding the generation of the undesired yellow phase and promoting the formation of pure black-phase CsPbI_3 film. A champion efficiency of 17.70% with a stabilized power output of 17.58% based on the optimized CsPbI_3 -DMAI device is achieved.

In the last chapter, the main conclusions of the thesis and future developments of inorganic PSCs are described.

Chapter 2 Europium-doped CsPbI₂Br for stable and highly efficient inorganic perovskite solar cells

This chapter was adapted from the following article with the permission of all co-authors and the journal.

Postprint version of the article: Xiang, W. [#]; **Wang, Z.** [#]; Kubicki, D. J.; Tress, W.; Luo, J.; Prochowicz, D.; Akin, S.; Emsley, L.; Zhou, J.; Dietler, G.; Grätzel, M.; Hagfeldt, A., Europium-doped CsPbI₂Br for stable and highly efficient inorganic perovskite solar cells. *Joule* 2019, 3 (1), 205-214.

[#]These authors contributed equally to this work.

My contribution: W. X. and Z. W. designed the project. W. X. and Z. W. analyzed and discussed the XRD, SEM and (HAADF) STEM data. W. X. and Z. W. wrote the manuscript.

All-inorganic perovskite films hold promise for improving stability of perovskite solar cells. However, the three-dimensional phase of narrow band gap inorganic perovskites is thermodynamically unstable at room temperature, limiting the development of high-performance inorganic PSCs. In this chapter, we show that europium doping of CsPbI₂Br stabilizes the 3D phase of the inorganic perovskite at room temperature. We rationalize it by using solid-state nuclear magnetic resonance and high-angle annular dark-field scanning transmission electron microscopy, which show that europium is incorporated into the perovskite lattice. We demonstrate a maximum power-conversion efficiency of 13.71% for an inorganic PSC with the CsPb_{0.95}Eu_{0.05}I₂Br perovskite in the mesoscopic architecture and a stable power output of 13.34%. Stability tests show that the devices retain 93% of the initial efficiency after 370 hours under 100 mW•cm⁻² continuous white light illumination under maximum power point tracking measurement.

2.1 Introduction

The past several years have witnessed rapid development of perovskites as excellent light absorbers for low-cost and solution-processable photovoltaics (PV).^{1,3,4,109,110} To date, the highest certified power conversion efficiency (PCE) reported for a perovskite solar cell (PSCs) has reached 25.2%,¹⁰ making it a viable competitor to silicon solar cells.¹⁷ However, organic components in these high efficiency inorganic-organic hybrid PSCs, such as methylammonium (MA) and formamidinium (FA), are intrinsically unstable due to the volatility of the haloid salts with these organic cations, leading to long-term stability issues.^{111,112} The replacement of these volatile organic components by inorganic cation Cs in all-inorganic perovskite materials may fundamentally improve the stability of PSCs.^{41,113} However, the key problem associated with narrow bandgap inorganic perovskites (such as CsPbI₃ and CsPbI₂Br) is their thermodynamic phase instability, whereby the desirable three-dimensional phase (“black phase”) of the narrow bandgap material spontaneously transforms into the orthorhombic, more thermodynamically stable δ -phase (“yellow phase”) at room temperature.^{2,46} This undesired phase transition is currently one of the bottle-neck limiting the development of high performance inorganic PSCs.

The stabilization of all-inorganic perovskite phases can be realized by either tailoring the perovskite grain size (i.e. by creating quantum dots) due to the large contribution of the surface energy,⁹⁹⁻¹⁰⁸ or by incorporation of other components into the perovskite material.^{47,82,89,95} In the latter case, three possible scenarios can be invoked to describe the resulting microstructure: (1) the dopant forms a separate phase and does not affect the atomic-level structure of the perovskite phase,^{114,115} (2) dopants modify the surface of the perovskite crystal,⁸⁸⁻¹¹⁶ and (3) the dopants are incorporated into the crystal lattice replacing one of its substituents.⁷⁷ The first scenario can lead to a complex mixture of phases, as is the case for addition of rubidium and potassium into organic-inorganic lead halide perovskites.¹¹⁴ The second scenario might affect the growth rate to reduce the crystal size and passivate the surface⁸⁸ while the third can substantially increase the entropy of the perovskite lattice and lead to thermodynamic stabilization, thereby solving the key problem of all-inorganic perovskites.^{77,114,117}

Europium has been reported as an efficient sensitizer of photoluminescence in perovskites and related materials.¹¹⁸ Compared to lead ion, the slightly smaller europium ion is expected to be incorporated into the perovskite lattice to increase the tolerance factor and result in an enhancement of the perovskite stability.¹¹⁹ Here we show that stoichiometric europium doping of the CsPbI₂Br all-inorganic perovskite leads to thermodynamically stable inorganic PSCs with excellent photovoltaic metrics and a PCE of 13.71% and a stable power output of 13.34%. We use solid-state nuclear magnetic resonance (NMR) and high-angle annular dark-field scanning transmission electron microscopy (HAADF STEM) to show that europium is

incorporated into the perovskite lattice at the atomic-level. Electroluminescence and time-resolved photoluminescence decay measurements show that incorporation of europium suppresses non-radiative charge carrier recombination. The cells of Eu doping maintained 93% of their initial performance under full illumination and maximum power point tracking.

2.2 Results and discussion

2.2.1 The performance of perovskite solar cells

We used the one-step spin-coating technique to deposit perovskite films from CsPb_{1-x}Eu_xI₂Br ($0 \leq x \leq 1$) precursor solutions. Spin-coated precursor films were then annealed at 280 °C for 10 min to form perovskite films. We employed the deposited films to fabricate PSCs in the following architecture: glass/fluorine-doped tin oxide (FTO)/compact TiO₂/mesoporous TiO₂/perovskite/2,2',7,7'-tetrakis(N,N-di-p-methoxyphenylamine)-9,9'-spirobifluorene (Spiro-OMeTAD)/Au. Figure 2.1a shows cross-sectional scanning electronic microscope (SEM) images of a full device with the estimated thickness of the perovskite layer of 150 nm. Figure 2.1b shows the J - V characteristics measured under 100 mW•cm⁻² light intensity for varying europium content. The corresponding photovoltaic parameters are listed in Table 2.1. The europium-doped devices ($x=0.01, 0.03, 0.05, 0.07$ and 0.09) show outstanding performance compared to those based on pure CsPbI₂Br owing to the striking improvement in short-circuit current density (J_{sc}), open-circuit voltage (V_{oc}) and fill factor (FF). The best solar cells made with CsPb_{0.95}Eu_{0.05}I₂Br show a champion PCE of up to 13.71% at a scan rate of 10 mV s⁻¹ (Figure 2.1b). The stabilized output power of the best device was recorded as 13.34% at full sun illumination with a stable J_{sc} of 13.94 mA cm⁻² (Figure 2.1c). Incident photon-to-current conversion efficiency (IPCE) measurements carried out on this cell show over 80% efficiency in the range between 420 nm and 650 nm, leading to an integrated current density of 14.3 mA•cm⁻², consistent with the J_{sc} in the J - V measurement (Figure 2.1d). The cells fabricated using CsPb_{0.95}Eu_{0.05}I₂Br show moderate hysteresis with a hysteresis factor of 0.06 (Figure 2.1e). Besides, a CsPb_{0.95}Eu_{0.05}I₂Br device with the highest V_{oc} of 1.27 V is achieved (Figure 2.1f).

Table 2.1 Photovoltaic parameters of perovskite solar cells fabricated using CsPbI₂Br doped with europium, measured at 100 mW cm⁻² light intensity.

Perovskite composition	V_{oc} (mV)	J_{sc} (mA·cm ⁻²)	FF	PCE (%)
CsPbI ₂ Br	1.120	12.57	0.725	10.21
CsPb _{0.99} Eu _{0.01} I ₂ Br	1.160	14.16	0.753	12.37
CsPb _{0.97} Eu _{0.03} I ₂ Br	1.208	14.64	0.745	13.18
CsPb _{0.95} Eu _{0.05} I ₂ Br	1.223	14.63	0.766	13.71
CsPb _{0.93} Eu _{0.07} I ₂ Br	1.100	14.59	0.776	12.45
CsPb _{0.91} Eu _{0.09} I ₂ Br	1.070	13.95	0.735	10.97

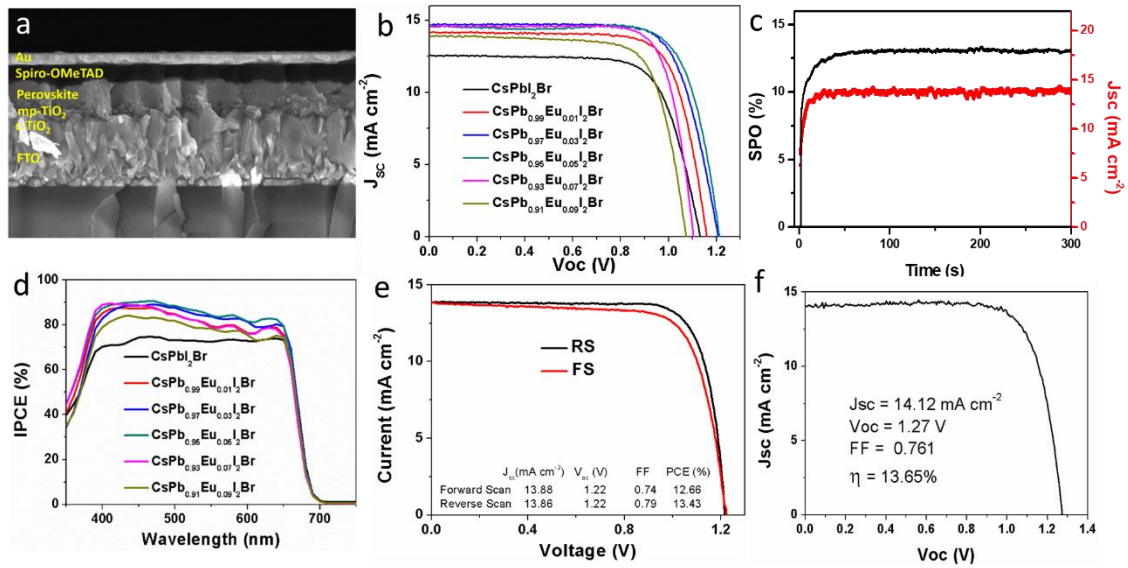


Figure 2.1. Photovoltaic Performance of perovskite solar cells (PSCs). (a) Cross-sectional SEM image of a complete CsPb_{0.95}Eu_{0.05}I₂Br inorganic PSCs. The scale bar is 400 nm. (b) J-V characteristics of inorganic perovskite solar cells fabricated using CsPb_{1-x}Eu_xI₂Br (x=0.00-0.09) absorbers. (c) IPCE characteristics of inorganic perovskite solar cells fabricated using CsPb_{1-x}Eu_xI₂Br (x=0.00-0.09) absorbers. (d) Stabilized power output at maximum power point tracking under working condition with 100 mW cm⁻² irradiation. (e) Hysteresis of the one of the best CsPb_{0.95}Eu_{0.05}I₂Br devices with the scan rate of 10 mV s⁻¹. (f) J-V curve of one of the best performing CsPb_{0.95}Eu_{0.05}I₂Br PSCs with the highest V_{oc} .

2.2.2 Structure characterization of europium-doped CsPbI₂Br

We performed X-ray diffraction (XRD) analysis of the thin films to evaluate the effect of europium doping on the crystal structure of CsPbI₂Br (Figure 2.2a). Pristine CsPbI₂Br shows characteristic perovskite peaks at 14.6° and 29.7°. The XRD peak intensities of perovskite films are reduced with the addition of europium, indicating a decrease in the crystallite size.⁹⁵ In order to evaluate europium incorporation into the perovskite lattice, it is necessary to apply atomic-level methods.

We have recently shown that solid-state NMR allows probing the atomic-level microstructure of lead-halide perovskites, both in bulk and as thin films.^{114,120-122} Here, using ¹³³Cs solid-state MAS NMR we show that europium is incorporated into the parent CsPbI₂Br perovskite lattice.

Figure 2.2b shows solid-state ¹³³Cs MAS NMR of the bulk mechanoperovskites studied in this work. The paramagnetic phase synthesized by grinding and annealing of an equimolar mixture of caesium iodide and europium iodide exhibits a single peak at 171 ppm (full width at half maximum [FWHM] 1155 Hz) and a very short spin-lattice relaxation time, *T*₁, of about 10 ms, characteristic of paramagnetic compounds.¹²³ In the diamagnetic compounds, CsPbBr₃, CsPbI₃ and CsPbI₂Br, relaxation is 3 to 4 orders of magnitude slower (29.5, 95.8 and 44.6 s, respectively). The reference perovskite material of this study, CsPbI₂Br, exhibits a relatively broad peak at 142 ppm (fwhm: 5759 Hz) whose breadth is caused by disorder owing to the presence of caesium environments with a varying number of iodide and bromide closest neighbours. This notion is clearly illustrated by comparing it to CsPbBr₃ and CsPbI₃, which give relatively narrow lines (fwhm: 219 and 367 Hz, respectively), since in these compounds caesium only has one type of neighbour anions. As for CsPb_{0.95}Eu_{0.05}I₂Br, the ¹³³Cs resonance shifts very slightly (from 142 to 146 ppm), which can conceivably be caused either by (1) a paramagnetic shift resulting from the hyperfine interaction of europium f electrons with caesium, (2) phase separation of caesium europium mixed halides (Br-I), which would lead to a change in the original iodide-to-bromide ratio in CsPbI₂Br, similarly to what we and Hu et al. have previously observed in rubidium- and caesium-doped mixed-cation lead halide perovskites,^{114,124} or (c) bulk magnetic susceptibility effects caused by the presence of a paramagnetic phase, leading to inhomogeneity of the magnetic field inside the sample.

To establish which of these two scenarios applies, it suffices to analyse the spin-lattice relaxation of the europium-doped material (Figure 2.2c). If the material was to undergo a phase separation, one would expect to observe a bi-exponential *T*₁ build-up curve with a very quickly relaxing component corresponding to the purely paramagnetic caesium europium halide phase, and a slowly relaxing component corresponding to the unchanged diamagnetic perovskite (Figure 2.2c, dashed line). Experimentally, we observe a stretched exponential behaviour (solid

lines) with stretching factors β of 0.69, 0.44 and 0.38 for 3, 5 and 8 mol% stoichiometric Pb replacement in CsPbI₂Br. This result indicates the presence of a distribution of caesium relaxation times in the material, corresponding to caesium sites at different distances from the paramagnetic europium ions (the PRE effect scales approximately as inverse cube of the distance).¹²⁵ These results taken together confirm that europium is incorporated into the CsPbI₂Br perovskite lattice on the atomic level.

We applied high-angle annular dark-field (HAADF) STEM imaging and electron diffraction spectra (EDS,) elemental mapping to evaluate uniformity of europium distribution inside the perovskite grains (Figure 2.2d). The elemental maps indicate that europium is uniformly distributed within the sample, presenting negligible difference in element distribution throughout the grains. The uniformity is the same for all the other elements.

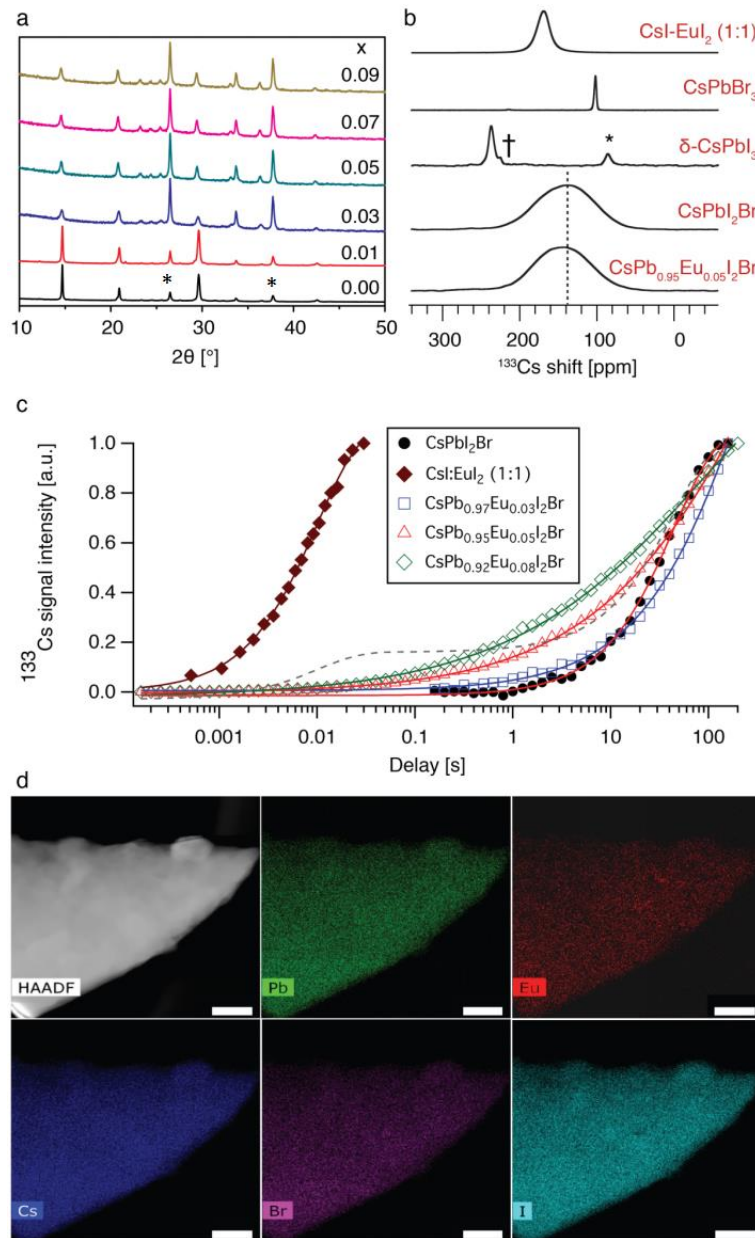


Figure 2.2. Structure characterization of europium-doped CsPbI₂Br. (a) XRD patterns of perovskite thin films of CsPb_{1-x}Eu_xI₂Br ($0 \leq x \leq 0.09$), * represents the FTO peaks. (b) ¹³³Cs solid-state MAS NMR spectra of mechanochemical perovskite compositions measured at 11.7 T 20 kHz MAS and 298 K. † is a transmitter artefact, * is a spinning sideband. (c) ¹³³Cs spin-lattice relaxation times, T₁, of selected perovskite compositions (details in the text). The solid curves are stretched exponential fits. The dashed line is the best bi-exponential fit of the CsPb_{0.95}Eu_{0.05}I₂Br data set. (d) HAADF-STEM image and elemental maps of CsPb_{0.95}Eu_{0.05}I₂Br. The white bar indicates 100 nm.

2.2.3 Morphology and optical characterizations of perovskite films

The plan-view scanning electron microscopy (SEM) images of the inorganic perovskite thin films are shown in Figure 2.3. The CsPbI₂Br film (Figure 2.3a) exhibits a relatively uniform surface coverage with crystal domains and clear pinholes. Upon incorporation of 1 mol% of europium (CsPb_{0.99}Eu_{0.01}I₂Br), the size of perovskite cubic crystals is decreased and new pinholes are generated. The film quality is again improved for increasing europium doping ratio, and the CsPb_{0.95}Eu_{0.05}I₂Br (Figure 2.3b) film is fully uniform. Consequently, uniform coverage may be one of the reasons behind the improved photovoltaic performance of europium-doped perovskites. On the other hand, the grain size decreases for increasing europium concentration, with the average particle size less than 50 nm in the CsPb_{0.95}Eu_{0.05}I₂Br film. Higher concentration of europium ($x=0.07$ and 0.09) does not lead to further improvement in the film morphology.

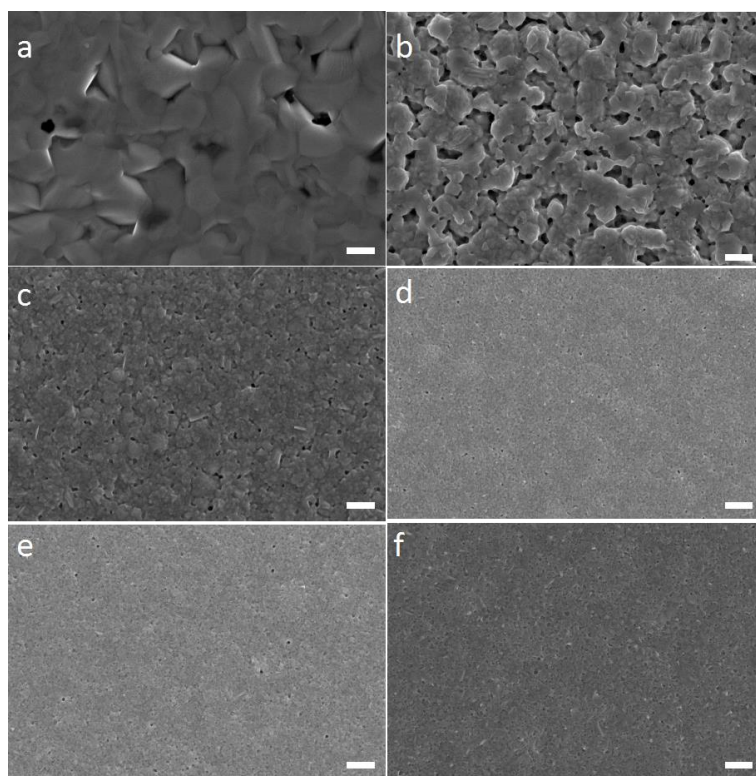


Figure 2.3. Morphology Characterization. SEM images of (a) CsPbI₂Br, (b) CsPb_{0.99}Eu_{0.01}I₂Br, (c) CsPb_{0.97}Eu_{0.03}I₂Br, (d) CsPb_{0.95}Eu_{0.05}I₂Br, (e) CsPb_{0.93}Eu_{0.07}I₂Br and (f) CsPb_{0.91}Eu_{0.09}I₂Br perovskite thin films. The scale bar is 400 nm.

Figure 2.4a shows UV-Vis absorption spectra and photoluminescence (PL) spectra of the perovskite thin films with CsPbI₂Br and CsPb_{0.95}Eu_{0.05}I₂Br perovskite thin films. The absorption intensity of the CsPb_{0.95}Eu_{0.05}I₂Br films within the measuring range is higher than that of CsPbI₂Br, probably due to the improvement in the film morphology. A small blue shift is visible in the photoluminescence (PL) spectrum with the maxima at 649 and 644 nm for 0 and 5 mol% europium, respectively. This may be caused by a change in the band structure upon europium incorporation or, more trivially, by the reduction in crystallinity and grain size, consistent with the SEM images.⁴⁷ Time resolved photoluminescence (TRPL) measurements (Figure 2.4b) show increased photoluminescence lifetimes upon europium incorporation. This result suggests suppression of non-radiative recombination pathways, consistent with the improved V_{oc} measured on europium-doped PSCs.

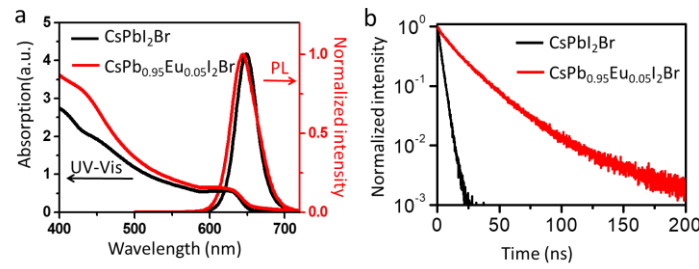


Figure 2.4. Optical characterization of CsPbI₂Br and CsPb_{0.95}Eu_{0.05}I₂Br perovskite thin films. (a) Normalized UV-Vis absorption and PL emission spectra measured at 298 K, (b) Time-resolved photoluminescence decays measured at 298 K.

2.2.4 Optoelectronic characterization of devices

To gain more insight into how europium incorporation suppresses charge recombination within the films, the V_{oc} was measured as a function of light intensity, and electroluminescence (EL) was recorded as a function of the injection current by measuring a CsPb_{0.95}Eu_{0.05}I₂Br device with the highest V_{oc} of 1.27 V as well as the best CsPbI₂Br device. EL measurements can be used to characterize recombination at a full solar-cell device, which is kept in the dark and a forward bias is applied to drive a current by injection of electrons at the FTO/TiO₂ and holes at the spiro-OMeTAD/Au contact. They recombine and the fraction of radiative recombination is measured in EL emission. Figure 2.5a shows the external EL yield of CsPbI₂Br and CsPb_{0.95}Eu_{0.05}I₂Br devices. The EL intensity recorded at a current close to J_{sc} gives external EL yields of roughly 1×10^{-7} and 2×10^{-6} , showing a considerable decrease in non-radiative

recombination upon europium doping. This result predicts an increase of 80 mV in the V_{oc} (1.19 to 1.27 V) according to the calculation approach used, for example, in Tress et al. (band gap of 1.92 eV).¹²⁶ Another difference is visible in the power-law coefficient (slope of the semilogarithmic plot). It decreases from 2 to approximately 0.8, implying a reduction of the ideality factor from 3 to 1.8.¹²⁷ To verify whether this trend is also present under illumination, we analyzed the V_{oc} as a function of the light intensity. Figure 2.5b shows the V_{oc} measured for two consecutive stepwise intensity sweeps from 0 to 1 sun (forward and backward). The common slow transient response known from the J-V hysteresis,¹²⁸ makes it difficult to accurately determine the ideality factor. Therefore, the values deduced from this plot contain a large error and depend on how fast the intensity sweep is performed. To avoid the direct influence of the transients, we propose to determine the ideality factor for each intensity step at the voltage response within 1 s (Figure 2.5c). This reproduces well the trend of the ideality factor seen in EL, although with slightly lower average values. The high ideality factor (>2) for the reference CsPbI₂Br device cannot be explained in the framework of the established recombination theory, where values less than or equal to 2 are expected. Larger values have been explained by the presence of large defect distributions¹²⁹ or coupled multi-level defect recombination. The latter has been observed in particular at certain positions in the device such as local shunts, which is consistent with the pinholes observed in the SEM images (Figure 2.3a). Upon europium incorporation, this effect disappears, and the ideality factor ≤ 1.5 is indicative of Shockley-Read-Hall recombination at regions with high background charge carrier densities, such as interfaces.¹²⁷ Also this stepwise determination of the ideality factor yields differences between forward and backward intensity sweeps, indicating that recombination varies dynamically. Taken together, these results suggest that incorporation of europium into the CsPbI₂Br lattice significantly reduces non-radiative recombination and leads to a more stable V_{oc} .

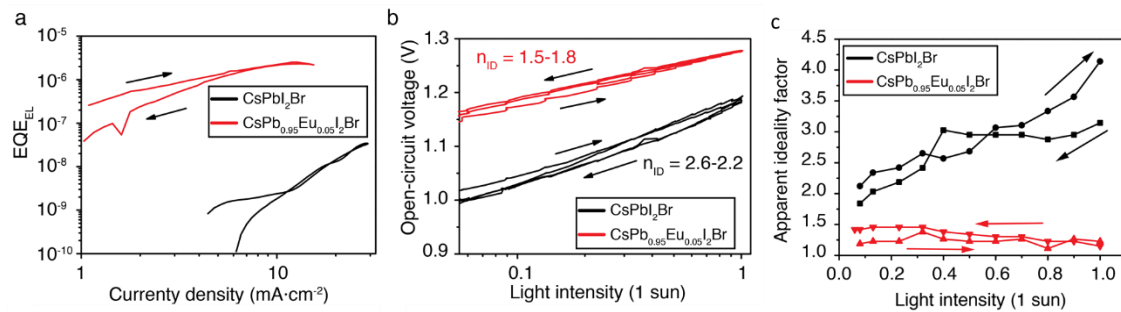


Figure 2.5. Optoelectronic characterization of devices. (a) external quantum yield of electroluminescence (EQE_{EL}) measured while performing a current-voltage sweep (10 mV/s) and plotted as a function of the injection current. The curves follow a power-law, resulting in the given ideality factors n_{ID} . (b) V_{oc} as a function of the light intensity extracted from the transient experiment. The resulting n_{ID} are slightly dependent on the scan direction. (c) Ideality factor differentially deduced from (b) and corrected for transients. The arrows indicate the scan direction.

2.2.5 Stability characterization of perovskite films and PSCs

In order to examine the long-term stability of the materials, we prepared thin films of CsPbI₂Br and CsPb_{0.95}Eu_{0.05}I₂Br and exposed them to ambient air at room temperature and under c.a. 40% relative humidity. Figure 2.6a shows photographs of the two films monitored over the course of 6 months. We found that CsPb_{0.95}Eu_{0.05}I₂Br remained dark during the whole monitoring period, while the CsPbI₂Br film became yellow-white in less than 50 h. After 1200 h we examined the two perovskite films by XRD (Figure 2.6c). Sharp perovskite peaks at 14.2° and 29.6° are visible for CsPb_{0.95}Eu_{0.05}I₂Br and none of them are present in the undoped CsPbI₂Br film, indicating that the perovskite phase has completely disappeared in the latter case. In order to study the phase of degraded CsPb_{0.95}Eu_{0.05}I₂Br, the film was storage in humid condition for 100h (humidity under c.a.50-70%, 298 ± 5 K) and we eventually got the completely degraded δ -perovskite phase (Figure 2.6d). We also monitored the evolution of UV-Vis spectra of CsPbI₂Br and CsPb_{0.95}Eu_{0.05}I₂Br perovskite films under relative humidity of 50-70% (Figure 2.6e and 6f). Although both films degraded into yellow phase eventually with no photoactivity in the visible range, the europium doped sample demonstrated better stability. At the same time, there is no shift of absorption onset during the measurement.

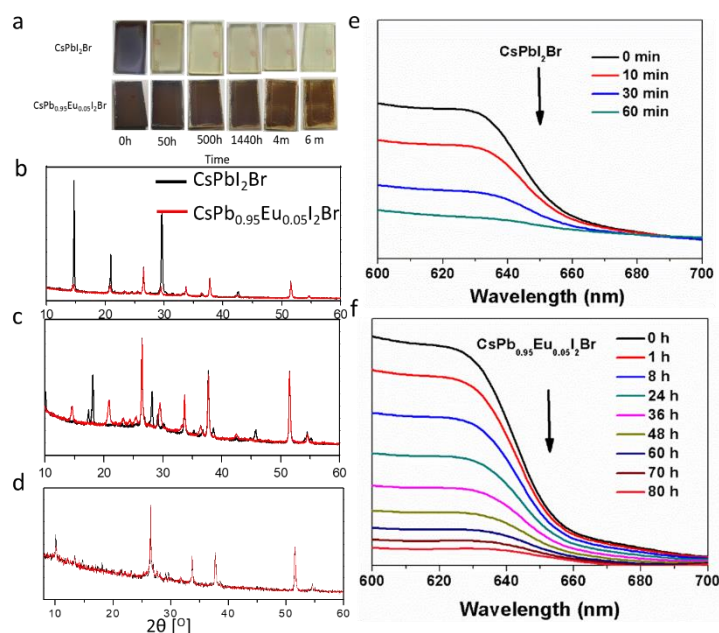


Figure 2.6. Phase stability of perovskite films. (a) Digital photographs of CsPbI₂Br and CsPb_{0.95}Eu_{0.05}I₂Br perovskite thin films on mesoporous TiO₂ exposed to ambient conditions over the period of time indicated below each snapshot (relative humidity under c.a. 20-40%, h: hours m: months) (b) XRD patterns of CsPbI₂Br and CsPb_{0.95}Eu_{0.05}I₂Br films in (b) freshly prepared (humidity under c.a. 20-40%, 298±5 K), (c) ambient condition for 1200 h (humidity under c.a. 20-40%, 298±5 K) and (d) humid condition for 100 h (humidity under c.a. 50-70%, 298±5 K). The evolution of UV-Vis spectra of CsPbI₂Br (e) and CsPb_{0.95}Eu_{0.05}I₂Br (f) perovskite thin films stored in ambient

conditions (humidity under c.a 50-70%, 298±5 K).

We subjected one of the best performing, unencapsulated CsPb_{0.95}Eu_{0.05}I₂Br-based devices to a long-term stability test under continuous white light LED illumination at 100 mW·cm⁻² with N₂ gas flow during 370 hours (Figure 2.7). An undoped CsPbI₂Br device was monitored under identical conditions as a reference. The CsPb_{0.95}Eu_{0.05}I₂Br device showed no signs of degradation during the first 300 h and maintained 93% of its initial efficiency at the end of the test. Conversely, the efficiency of the CsPbI₂Br device dropped to half of its initial value in less than 30 hours and retained only about 20% of its initial value at the end of the test, probably due to thermodynamic instability of this perovskite phase. The exceptional stability of the CsPb_{0.95}Eu_{0.05}I₂Br device can be explained by the excellent thermodynamic phase stability of the europium-doped perovskite. This may be due to the increase of tolerance factor after europium doping, which could induce less distortion of the perovskite lattice.¹¹⁹ In addition, the increase of surface to volume ratio leads to the increase of surface energy. Therefore, more energy is required to conquer the barrier for the transformation from black perovskite phase to δ non-perovskite phase.¹³⁰

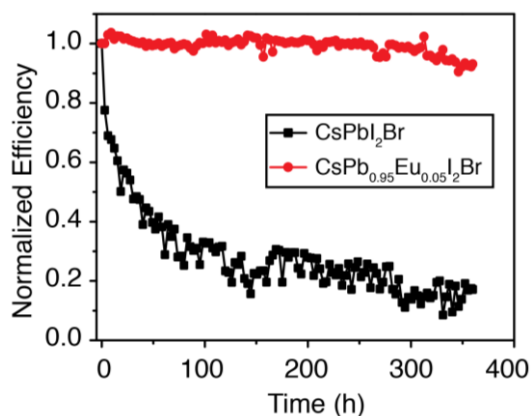


Figure 2.7. Stability characterization of PSCs. Normalized PCE of unencapsulated CsPbI₂Br and CsPb_{0.95}Eu_{0.05}I₂Br devices monitored under continuous white light exposure as a function of time.

2.3 Summary

In conclusion, we have reported an all-inorganic europium-doped CsPbI₂Br perovskite for photovoltaic applications. It is used as an absorber layer in mesoscopic solar cells which obtained power conversion efficiencies of up to 13.71% and a stable power output of 13.34%. Using solid-state NMR and STEM-HAADF, we have shown that europium is incorporated into the perovskite lattice at the atomic level. Meanwhile, europium doping leads to exceptionally high thermodynamic stability of the CsPbI₂Br perovskite, which translates to excellent operational stability of the resulting solar cells.

2.4 Experimental section

2.4.1 Preparation method

Preparation of the substrate The FTO conducting glass is from Nippon with the square resistance of 10 Ω /sq. 2% Hellmanex solution, acetone and ethanol were used for cleaning the glass by sonication for 30 min, 10 min and 10 min, separately. The 30 nm thick TiO₂ compact layer was deposited on top of cleaned FTO glass by spray pyrolysis at 450 °C from a precursor solution containing titanium diisopropoxide bis(acetylacetonate) (0.6 ml) and acetoacetate (0.4 ml) in 9 ml anhydrous ethanol. The 150 nm thick mesoporous TiO₂ was then deposited by spin-coating a diluted TiO₂ paste (30 nm particle size, Dyesol) in absolute ethanol at the speed of 5000 rpm for 15 s. These TiO₂ films were dried at 80 °C for 5 min and further sintered at 450 °C for 30 min under continuous dry air flow. After cooling down to approximately 150 °C, these films were immediately transferred into glovebox filled with dry air.

Perovskite solution preparation 1 M CsPbI₂Br perovskite precursor solution was prepared by stoichiometrically mixing 259.8 mg CsI (Merck), 183.5 mg PbBr₂ (TCI) and 230.5 mg PbI₂ (TCI) in 1 ml anhydrous DMSO. This solution was heated overnight at 75 °C to form a clear mixture. The CsPb_{1-x}Eu_xI₂Br perovskite precursor was prepared by mixing 1 M CsPbI₂Br solution, 1 M CsBr formamide solution and 1 M EuI₂ DMF: DMSO (v:v=4:1) solution stoichiometrically in dry air box.

Device fabrication The perovskite films were prepared by spin-coating the precursor solutions in a two steps program at 1000 rpm and 3000 rpm for 10 s and 30 s in dry air box, respectively. The films were then left for 5 min before applying annealing treatment at 280 °C for 10 min. After cooling down to room temperature, the solution of spiro-OMeTAD (Merck) in chlorobenzene (90 mg ml⁻¹) with 20.6 μ l bis(trifluoromethylsulfonyl)imide lithium salt (LiTFSI, Sigma-Aldrich, 520 mg ml⁻¹ in acetonitrile) and 35.5 μ l 4-tert-butylpyridine (t-BP, Sigma-Aldrich) was spun on top of the perovskite film at 4000 rpm for 20 s. Finally, an 80 nm thick Au back-contact metal electrode was thermally evaporated to complete the device fabrication.

2.4.2 Characterization

Photovoltaic measurements The PSCs were tested with a 450 W xenon light source (Oriel). The light intensity was calibrated by a silicon photodiode equipped with an IR-cutoff filter (KG3, Schott) and was recorded for each measurement. The current-voltage curves (*J-V* curves) of the devices were recorded by applying an external voltage bias with a digital source meter (Keithley 2400) to give the corresponding current response. A black metal mask with an area of 0.16 cm² was applied to define the active area of the cells and to avoid the overestimation of

the light input. The hysteresis factor is defined using the following equation from literature : ¹³¹

$$\text{Hysteresis factor} = \frac{PCE_{reverse} - PCE_{forward}}{PCE_{reverse}}$$

Incident photon-to-current conversion efficiency Incident photon-to-current conversion efficiency (IPCE) measurements were carried out from monochromated visible photons, from a Gemini-180 double monochromator (Jobin Yvon Ltd. (UK)), powered by a 300 W xenon light source (ILC Technology, USA) superimposed on a 1 mW·cm⁻² LED light. The monochromatic incident light was passed through a chopper running at 8 Hz frequency and the on/off ratio was measured by an operational amplifier.

Solid-state nuclear magnetic resonance

Perovskite mechanosynthesis The starting materials were stored inside a glove box under argon. Bulk perovskite powders were synthesized by grinding the starting materials in an electric ball mill (Retsch Ball Mill MM-200, 10 ml grinding jar and a ø10 mm ball) for 30 min at 25 Hz. ¹³² The resulting perovskite powders were annealed at 280 °C for 5 minutes to reproduce the thin-film synthetic procedure. All materials were characterized using powder X-ray diffraction (pXRD).

0.106 g of CsBr (0.50 mmol) and 0.183 g of PbBr₂ (0.50 mmol) were mixed to prepare CsPbBr₃ (orange powder). 0.212 g of CsBr (1.00 mmol) and 0.461 g of PbI₂ (1.00 mmol) were mixed to prepare CsPbI₂Br (black powder). 0.129 g of CsI (0.50 mmol) and 0.202 g of EuI₂ (0.50 mmol) were mixed to prepare a paramagnetic caesium europium iodide (yellow powder). In this case, a new phase was formed, as evidenced by the absence of CsI in the ¹³³Cs NMR spectra and full transformation into a single paramagnetic ¹³³Cs environment. We were unable to assign this phase to any of the caesium europium iodides previously described in the ICDD database. Here we use it only to estimate the order of magnitude of spin-lattice relaxation of ¹³³Cs nuclei in paramagnetic caesium europium iodide phases.

Perovskite solution processing The CsPb_{1-x}Eu_xI₂Br perovskite precursors were prepared by mixing above mentioned 1 M CsPbI₂Br solution, 1 M CsBr formamide solution and 1 M EuI₂ DMF: DMSO (v:v=4:1) solution. The perovskite films were prepared by spin-coating the precursor solutions on a glass substrate. After annealing at 280 °C for 10 min, these films were cool down and scratched off for ss-NMR characterization.

Powder X-ray Diffraction Diffractograms were recorded on an X'Pert MPD PRO (Panalytical) diffractometer equipped with a ceramic tube (Cu anode, λ = 1.54060 Å), a secondary graphite (002) monochromator and an RTMS X'Celerator (Panalytical) in an angle range of 2θ = 5° to 40°, by step scanning with a step of 0.02 degree.

NMR measurements Room-temperature (298 ± 3) K solid-state ¹³³Cs (65.6 MHz) MAS NMR

spectra were acquired on a Bruker Avance III 11.7 T spectrometer equipped with a 3.2 mm MAS probe. The spin-lattice relaxation times, T_1 , were measured using a saturation-recovery pulse sequence and fitted using a stretched exponential model: $I[t] = I[0] + A \cdot \exp\left(-\frac{t}{T_1}\right)^\beta$, where $I[t]$ is the integrated intensity of the spectrum acquired for a time delay t , $I[0]$ and A are adjustable parameters and β is the stretching parameter. When $\beta=1$ the equation simplifies to a monoexponential model (a single T_1 value describes all nuclei) whereas for $0 < \beta < 1$ it corresponds to a distribution of T_1 values in the material, with lower β corresponding to a broader distribution of spin-lattice relaxation times.

X-ray diffraction The perovskite films on mesoporous TiO₂ substrates were prepared as described in the device fabrication section. X-ray diffraction (XRD) patterns were acquired with a PANalytical Empyrean diffractometer in the transmission-reflection mode, using the Cu K α radiation and the Ni β -filter.

Scanning electron microscopy The perovskite films were deposited on mesoporous TiO₂ substrates to reflect the film morphology in complete PSCs. SEM micrographs were acquired on a Zeiss Merlin microscope with an in-lens detector at 5 kV acceleration voltage and 150 pA probe current. The working distance was 4.0 mm and no tilt was used.

Transmission electron microscope The perovskite samples for TEM characterization were prepared as follows. The perovskite films on plain glass substrates were first prepared by spin coating, as described above. These films were then scratched off from the substrate to a glass vial and appropriate amount of anhydrous toluene was added. After sonicating for several seconds, the dispersed solution was dropped onto a gold mesh and the solvent was evaporated in air naturally. Transmission electron microscopy was performed on a Technai Osiris (FEI) microscope. Energy-dispersive X-ray (EDX) elemental mapping was carried out in the scanning transmission electron microscopy (STEM) mode. The contrast against the background of HAADF-STEM image of Eu mapping has been modified to make it clearer to be seen.

Atomic force microscope The perovskite films were deposited on mesoporous TiO₂ substrates. AFM images were collected on a NX-10 Atomic Force Microscope (Park Systems, South Korea) with non-contact Amplitude Modulation (NC-AM) in ambient condition. The AFM images with a resolution of 256×256 pixels in square areas of 9 × 9 μm^2 were obtained, using the non-contact cantilevers (PPP-NCHR, Park systems, South Korea) with a resonance frequency of 330 kHz and a force constant of 42 N/m. To precisely control the cantilever in each measurement, a weak tip-sample interaction is carefully achieved by monitoring a low AFM phase images in the range of $\pm 5^\circ$. AFM images were processed by XEI software (Park System, South Korea) for flattening. To compare the data from each measurement, every AFM image was flattened by a plane in 2nd order.

Optical characterization UV-Vis measurements were performed on a Varian Cary 5 spectrophotometer. Photoluminescence spectra were obtained with Fluorolog 322 spectrofluorometer (Horiba Jobin Yvon Ltd) with the range of wavelength from 500 nm to 800 nm by exciting at 450 nm with a standard 450-W Xenon CW lamp. The samples were mounted at 60° and the emission recorded at 90° from the incident beam path. Time-resolved photoluminescence was performed using Fluorolog 322 spectrofluorometer (Horiba Jobin Yvon Ltd.). A NanoLED-405L (Horiba) laser diode (peak wavelength 405 nm) was used for excitation. The detection monochromator was set to 650 nm and the photoluminescence was recorded using a picosecond photodetection module (TBX-04, Horiba Scientific).

Electroluminescence (EL) EL was measured by performing cyclic voltammetry using a Biologic SP300 potentiostat while measuring the short-circuit current of a Hamamatsu Silicon photodiode (area 1 cm²) placed in close vicinity of the sample. An estimation of the external quantum yield of EL is obtained by dividing this current corrected for the spectral response of the photodiode by the driving current of the tested PSC.

V_{oc} vs. light intensity measurements The voltage was tracked with a Biologic MPG2 potentiostat and the illumination was provided by an LED solar simulator (Verasol-2, Newport Corporation) with adjustable intensity. The intensity was monitored simultaneously using a silicon photodiode.

Stability test Stability measurements were performed with a Biologic MPG2 potentiostat under a full AM 1.5 Sun-equivalent white LED lamp. The devices were masked to 0.16 cm² and were connected to a separate channel of a potentiostat. A continuous flow of dry nitrogen gas was flushed into the custom-built airtight weathering chamber as the sample holder. The devices were measured *in situ* with a maximum power point (MPP) tracking routine under continuous illumination. The MPP was updated every 10 s by a standard perturb-and-observe method. A Peltier element in direct contact with the films was used to control the temperature of the devices. A Pt100 thermometer inserted between the Peltier element and the film was used to measure the temperature of the devices. Every 30 minutes a J-V curve was recorded in order to track the evolution of individual J-V parameters. The setup is centrally-controlled through a LabView interface allowing for automatic programming of experiments (temperature, illumination, atmosphere, electronic measurements).

Chapter 3 Ba-induced phase segregation and band gap reduction in mixed-halide CsPbI₂Br for inorganic perovskite solar cells

This chapter was adapted from the following article with the permission of all co-authors and the journal.

Postprint version of the article: Xiang, W. [#]; Wang, Z. [#]; Kubicki, D. J.; Wang, X.; Tress, W.; Luo, J.; Zhang, J.; Hofstetter, A.; Zhang, L.; Emsley, L.; Gratzel, M.; Hagfeldt, A., Ba-induced phase segregation and band gap reduction in mixed-halide inorganic perovskite solar cells. Nat. Commun. 2019, 10 (1), 4686.

[#]These authors contributed equally to this work.

My contribution: W. X. and Z. W. designed the project. W. X., Z. W. and J. L. carried out SEM imaging. W. X., Z. W. performed the XPS measurements and analyzed the XRD and SEM data. J. Z., W. X and Z. W. performed PL measurements and analysed the resulting data. W. X. and Z. W. wrote the manuscript.

All-inorganic metal halide perovskites are showing promising development towards efficient long-term stable materials and solar cells. Element doping, especially on the lead site, has been proved to be a useful strategy to obtain the desired film quality and material phase for high efficient and stable inorganic perovskite solar cells. Here, we demonstrate a function by adding barium in CsPbI₂Br. We find that barium is not incorporated into the perovskite lattice but induces phase segregation, resulting in a change in the iodide/bromide ratio compared to the precursor stoichiometry and consequently a reduction in the band gap energy of the perovskite phase. The device with 20 mol% barium shows a high power conversion efficiency of 14.0% and a great suppression of non-radiative recombination within the inorganic perovskite, yielding a high open circuit voltage of 1.33 V and an external quantum efficiency of electroluminescence of 10⁻⁴.

3.1 Introduction

Lead halide perovskites have the advantage of relatively high charge carrier diffusion lengths, high light harvesting efficiency and band gap (E_g) tunability, making them ideal materials for photovoltaic applications.² In less than 10 years, the certified power conversion efficiency (PCE) of perovskite solar cells (PSCs) has reached 25.2%, which is higher than that of polycrystalline silicon solar cells.^{1,3,4,10,109} Despite these advances, the use of organic components (e.g. methylammonium (MA) and formamidinium (FA)) in perovskite materials generates stability concerns due to the volatility of the organic components.^{111,112,133,134} Therefore, the development of all-inorganic perovskites for photovoltaic devices is currently extensively explored, as the replacement of organic components by their inorganic counterpart (Cs^+) could solve the stability issue.^{99,113}

Nevertheless, the inorganic lead halide perovskite solar cells are still facing large challenges in the improvement of PCE and phase stability, due to large E_g (1.7 eV-2.3 eV) relative to the ideal E_g of approximately 1.35 eV for single-junction solar cells,^{17,40} and instability of the cubic phase or black phase for I-based narrow band gap inorganic perovskites.^{12,135} Element doping, especially on the lead site, has been proved to be a useful strategy to solve the above problems as well as reduce the usage amount of toxic lead.¹³⁶ For example, Sn^{2+} and Ge^{2+} , belonging to the same (IV) group as Pb^{2+} , seem to be the most promising candidates to replace Pb^{2+} while also exhibiting band gap tunability.^{137,138} However, the fast oxidation of Sn^{2+} and Ge^{2+} when exposed to ambient atmosphere limits the fabrication of Sn/Ge-based PSCs to inert environments.¹³⁹ Other divalent cations such as Mn^{2+} , Sr^{2+} , Eu^{2+} , etc, have been explored as dopants for inorganic perovskites,^{88,89,140,141} but they are generally at low doping ratios (typically around 5% on the lead site) and do not alter the band gap substantially. In addition, there is no consensus in terms of whether these cations are being incorporated into the perovskite lattice and the exact action mechanism of these dopants to improve the PSC performance is still under debate.⁸⁶

Here, we show that barium can be added in large quantities (the molar ratio of barium and lead up to 4:6 in the perovskite precursor solutions) during the synthesis of the inorganic CsPbI₂Br perovskite, leading to the reduction of the perovskite band gap. The open-circuit voltage (V_{oc}) of the inorganic PSCs with the addition of 20 mol% barium to the precursor solution is significantly improved to 1.33 V, yielding a PCE of 14.0%. To the best of our knowledge, this is the highest reported V_{oc} for all-inorganic PSCs with a band gap lower than 2 eV. Solid-state nuclear magnetic resonance (ss-NMR) measurements evidence that there is no incorporation of barium into the perovskite lattice. Rather, barium segregates into barium-based non-perovskite phases with concomitant halide segregation. As a consequence, the perovskite phase is enriched

in iodide, leading to changes in the lattice parameter and band gap compared to the undoped CsPbI₂Br. The I-rich perovskite acts as the light harvesting species and its band gap is linearly dependent on the amount of added barium, while the barium-based non-perovskite phases prohibit non-radiative recombination and are responsible for the high V_{oc} .

3.2 Results and discussion

3.2.1 Perovskite materials characterizations and photovoltaic performance of devices

The perovskite precursor solutions were prepared by mixing CsI, PbI₂, PbBr₂, CsBr and BaI₂ in the required stoichiometric molar ratios in anhydrous dimethylsulfoxide (DMSO). The perovskite films were deposited from precursor solutions on mesoporous TiO₂ substrates at a spinning speed of 3000 rpm with the conventional one-step spin coating method. The films were subsequently annealed at 280 °C for 10 min in dry air. For convenience, we refer to these films using their precursor solution stoichiometry: CsPb_{1-x}Ba_xI₂Br ($x = 0$ to 1). Figure 3.1 shows the photographs of these perovskite films for different barium concentration. The color of the films gradually changes from dark into light brown as the barium fraction is increased. The pure CsBaI₂Br film is colourless, confirming negligible absorption of visible light. Therefore, in the following we restrict ourselves to barium molar fraction $x \leq 0.4$ for PSCs fabrication.

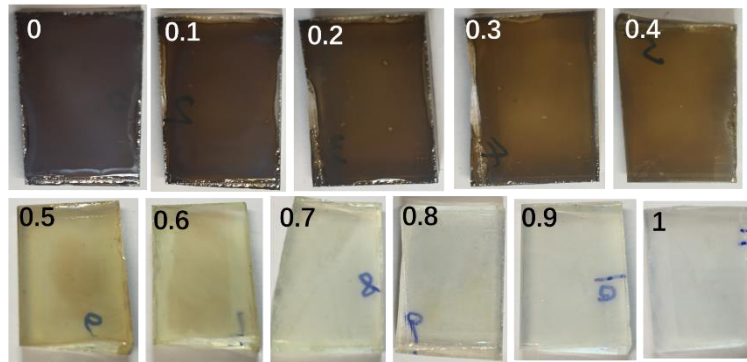


Figure 3.1. Digital images of the CsPb_{1-x}Ba_xI₂Br ($x = 0$ to 1) inorganic perovskite films on mesoporous TiO₂ substrates.

We first investigated the X-ray diffraction (XRD) of the CsPb_{1-x}Ba_xI₂Br ($x = 0$ to 0.4) thin films. The XRD patterns are shown in Figure 3.2a. The addition of barium resulted in a gradual decrease of the perovskite peak intensities (diagnostic peaks: 14.5°, 21.1°, 29.7°), which can still be reserved for $x \leq 0.4$. A close scrutiny of the reflection peaks (Figure 3.2a) revealed a noticeable shift to lower angles. According to the Bragg's law, the low-angle shift reflects an expansion of the unit-cell volume.⁴⁰ Its effect on the optoelectronic properties was further examined by ultraviolet-visible (UV-Vis) spectroscopy (Figure 3.2b). We found a significant

shift in the absorption onset to longer wavelength with increasing barium concentration. Meanwhile, a gradual decrease of the absorption intensity with constant film thickness indicates that the introduction of barium leads to a deterioration of the light harvesting capacity. An analogous red-shift trend was observed in photoluminescence (PL) emission spectra (Figure 3.2c). These results show that the introduction of barium alters the band gap of the parent CsPbI₂Br perovskite.

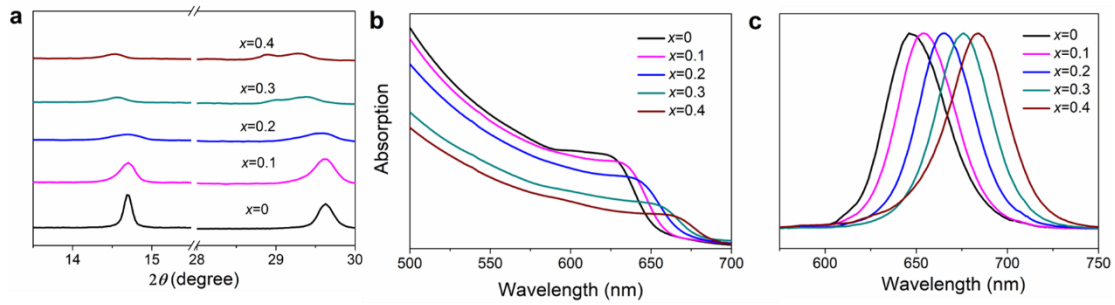


Figure 3.2. Materials characterization of CsPb_{1-x}Ba_xI₂Br with x varies from 0 to 0.4 compositions. a) XRD patterns, b) UV-Vis absorption and c) PL emission spectra.

The Ba-Pb mixed perovskites were then used to fabricate all-inorganic PSCs in the following device configuration: Fluoride-doped tin oxide (FTO) glass/compact-TiO₂ (c-TiO₂)/mesoporous TiO₂ (mp-TiO₂)/CsPb_{1-x}Ba_xI₂Br/2,2',7,7'-tetrakis(N,N-di-p-methoxyphenyl-amine) 9,9'-spirobifluorene (spiro-OMeTAD)/Au (for the cross sectional scanning electron microscope (SEM) image of a complete device, please refer to Figure 3.3a). The thickness of the perovskite layer is estimated to be around 170 nm. The photovoltaic parameters for $x = 0, 0.1, 0.2, 0.3$ and 0.4 are reported in Table 3.1 and the J - V curves are plotted in Figure 3.3b. The champion PSC fabricated using CsPbI₂Br (without barium) exhibits a V_{oc} of 1.12 V, a short circuit current (J_{sc}) of 13.4 mA cm⁻², a fill factor (FF) of 73.8%, yielding a PCE of 11.1%, which is comparable to those previously reported in the literatures.^{14,135} As the barium fraction increases to $x \geq 0.1$, the V_{oc} enhanced dramatically from 1.12 V to around 1.27 V, which accounts for roughly 15% of the total improvement. The highest obtained V_{oc} from one of the best performing devices fabricated using the CsPb_{0.8}Ba_{0.2}I₂Br composition exhibited a value of 1.33 V (Figure 3.3c). To the best of our knowledge, this is the highest reported V_{oc} for all-inorganic PSCs with a band gap lower than 2 eV. J_{sc} also shows a moderate increase as the barium concentration increases until $x = 0.2$, benefiting from the red-shifted absorption, in line with the UV-Vis characterization. Further increase of the barium concentration to $x = 0.3$ leads to a dramatic decrease of J_{sc} . The best PCE of 14.0% under one sun illumination was obtained for $x = 0.2$. The stabilized power output (SPO) at maximum power point tracking of the best device shows a value of 13.6% along with a steady state current of 13.8 mA cm⁻² (Figure 3.3d). The incident photon-to-current conversion efficiency (IPCE, Figure 3.3e) measurement

demonstrates a broad absorption range from 640 nm to 380 nm with the absorption onset at 680 nm. The integrated J_{sc} of 14.1 mA cm⁻² also agrees with the measured value.

Table 3.1 Photovoltaic parameters of CsPb_{1-x}Ba_xI₂Br ($x = 0$ to 0.4) based inorganic PSCs. These PSCs were illuminated under 100 mW cm⁻² simulated sunlight.

Barium molar fraction, x	V_{oc} (V)	J_{sc} (mA cm ⁻²)	FF (%)	PCE (%)
0	1.12	13.4	73.8	11.1
0.1	1.27	13.9	75.3	13.3
0.2	1.28	14.0	78.2	14.0
0.3	1.29	12.8	70.8	11.7
0.4	1.27	10.1	66.1	8.4

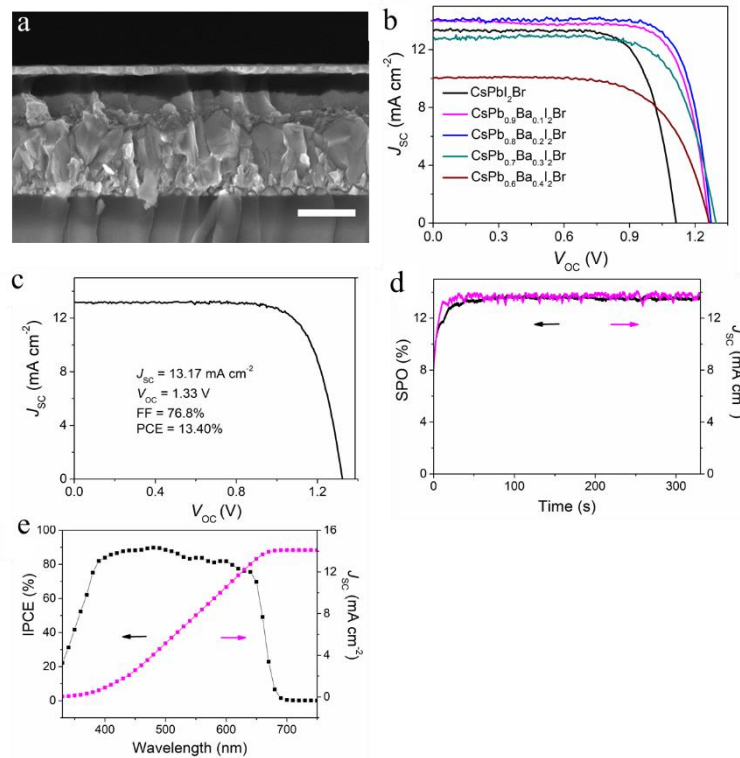


Figure 3.3. Photovoltaic performance of PSCs. (a) Cross-sectional SEM image of a complete inorganic PSC based on CsPb_{0.8}Ba_{0.2}I₂Br film. The scale bar is 500 nm. (b) J - V performance of CsPb_{1-x}Ba_xI₂Br ($x = 0$ to 0.4) based inorganic PSCs. (c) J - V performance of CsPb_{0.8}Ba_{0.2}I₂Br-based inorganic PSCs with high V_{oc} measured under 100 mW cm⁻² irradiation. (d) SPO and steady state J_{sc} of the CsPb_{0.8}Ba_{0.2}I₂Br-based PSCs; (e) IPCE and integrated J_{sc} of

the CsPb_{0.8}Ba_{0.2}I₂Br-based PSCs.

In order to elucidate the substantial enhancement of V_{oc} upon the addition of barium, we investigated the charge recombination behavior within the bulk perovskite by time-resolved photoluminescence (TRPL, Figure 3.4a). The plots show increased photoluminescence lifetimes upon barium addition. This result suggests suppression of non-radiative recombination pathways, consistent with the improved V_{oc} measured in barium-containing PSCs. In addition, the X-ray photoelectron spectra (XPS, Figure 3.4b) of Pb 4f from CsPbI₂Br show two small peaks at 136.9 eV and 141.7 eV, which are ascribed to the existence of metallic Pb. These two peaks completely disappear at 20% barium addition, implying that the introduction of barium can effectively suppress the formation of metallic Pb, which acts as non-radiative recombination centers and degrades PSCs performance. Thus, elimination of metallic Pb by barium can suppress the deep-level defects in PSCs.¹⁴²

This spectacular improvement in V_{oc} was further elucidated using electroluminescence (EL) by studying the device with the champion V_{oc} shown in Figure 3.3c. We can indeed observe an increase of the external EL quantum efficiency by three orders of magnitude when comparing the CsPb_{0.8}Ba_{0.2}I₂Br with a device without barium (Figure 3.4c). It reaches 10^{-4} for currents similar to J_{sc} , which corresponds to a non-radiative loss of 240 mV.¹²⁶ Considering the theoretical maximum V_{oc} of 1.56 V for a solar cell based on a material with a band gap of 1.86 eV, we calculate a V_{oc} of 1.32 V, which is consistent with the experimental data.¹²⁶ Figure 3.4c shows that with the increase of the EL, the slope decreases, indicative of a reduced ideality factor, which approaches 2 for the barium containing device.¹²⁸ These results indicate that addition of barium into the CsPbI₂Br precursor solution significantly reduces non-radiative recombination, which leads to a much improved V_{oc} .

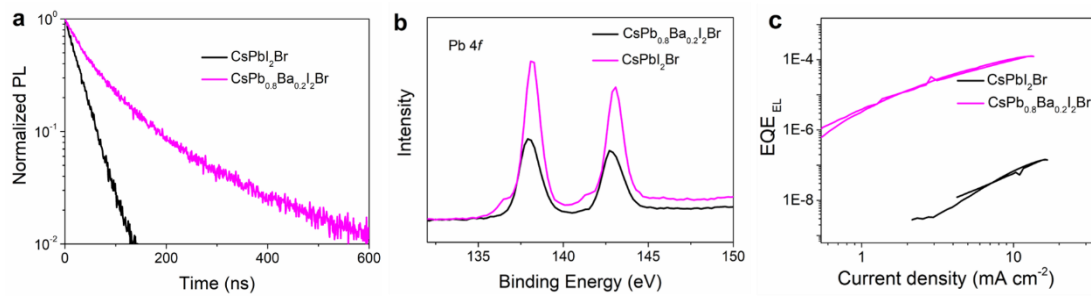


Figure 3.4. Non-radiative recombination analysis. (a) TRPL spectra of CsPbI₂Br and CsPb_{0.8}Ba_{0.2}I₂Br inorganic perovskite films. (b) Pb 4f spectra from XPS surface analysis of CsPbI₂Br and CsPb_{0.8}Ba_{0.2}I₂Br perovskite films. (c) EL measured during a J - V sweep from 0 to 1.6 V (1.4 V for CsPbI₂Br-based PSCs) and back with a rate of 10 mV s⁻¹.

3.2.2 Phase segregation analysis

We have recently shown that solid-state magic angle spinning (MAS) NMR is a suitable probe of the atomic-level microstructure in multi-component lead halide perovskites.^{114,120,122} In particular, ¹³³Cs can be used to probe cesium-containing phases in organic-inorganic and all-inorganic halide perovskites.^{114,132} To evidence whether or not barium is incorporated into the material described here, we carried out ¹³³Cs MAS NMR measurements on barium-containing CsPbBr₃ as a model compound (Figure 3.5a). We chose the single-halide 3D perovskite since simultaneous introduction of bromides and iodides causes halide disorder leading to very broad ¹³³Cs resonances.^{132,135} The reference mechanochemical CsPbBr₃ material shows a nearly pure perovskite phase (100.5 ppm, Figure 3.5a (I)). It contains 4% of a secondary impurity phase (226.6 ppm). The material with 20 mol% barium contains a perovskite phase (85%), whose spectrum is indistinguishable from that of CsPbBr₃ (100.5 ppm), and impurity phases at 216.8 ppm (14%) and 336.5 ppm (1%). Since the ¹³³Cs shift of the main perovskite phase is, to within error, unchanged, it strongly suggests that there is negligible barium substitution of lead in the CsPbBr₃. This is expected from the substantially larger ionic radius of Ba²⁺ (135 pm) compared to Pb²⁺ (119 pm). For further confirmation we have carried out fully-relativistic NMR shift calculations confirming that lead substitution by barium would lead to a ¹³³Cs shift with respect to CsPbBr₃ of *ca* +3 ppm for each closest barium cation on an A- or B-site (Supplementary Table S3.1), which would lead to a clear change in the spectra. There are a number of known non-perovskite cesium lead bromides and cesium barium bromides with different stoichiometries. We have mechanochemically prepared 1:2 and 4:1 CsBr:PbBr₂ and 2:1 and 1:2 CsBr:BaBr₂ materials (Figure 3.5a (III), (IV), (VI), (VII)). The 1:2 ratio of CsBr:PbBr₂ yielded a mixture of CsPb₂Br₅ (224.6 ppm, 83%) and CsPbBr₃ (100.5 ppm, 17%). The 4:1 ratio of CsBr:PbBr₂ yielded a mixture of unreacted CsBr (57%, 249.6 ppm), CsPbBr₃ (17%, 100.5 ppm) and two other phases, which we did not attempt to identify (216.8 ppm, 19% and 335.9 ppm, 6%). The two latter non-perovskite structures correspond perfectly to the impurity phases identified in the CsPb_{0.8}Ba_{0.2}Br₃ composition (Figure 3.5a (II)). Both CsBr:BaBr₂ mixtures yielded a small amount of a new cesium barium bromide (227.0 ppm, 28% and 8% for the 1:2 and 2:1 ratios, respectively) and a corresponding amount of unreacted CsBr (Figure 3.5a (V-VII)). The barium-based non-perovskite phase is present in the CsPb_{0.8}Ba_{0.2}Br₃ composition (Figure 3.5a (II), inset) albeit at a very low concentration (around 1%). Taken together, the ¹³³Cs spectra show that there is no incorporation of barium into the model CsPbBr₃.

Barium incorporation could also conceivably be probed using barium-137 NMR. Substitutional doping of barium on the A- or B-site should lead to a very symmetric (cubic or nearly cubic) ligand environment of barium and as a consequence to small electric-field gradient (EFG) tensors of the ¹³⁷Ba nucleus and thus relatively narrow ¹³⁷Ba NMR signals, as is the case for

BaTiO₃.¹⁴³ We have carried out fully-relativistic EFG calculations for ¹³⁷Ba incorporated on an A- and B-site of CsPbBr₃ and confirmed that it should lead to a full-width-at-half-maximum (fwhm) of about 15 ppm (1.5 kHz). We were unable to detect any ¹³⁷Ba signal on the CsPb_{0.8}Ba_{0.2}Br₃ composition over 12 hr using an RF strength of 125 kHz, which should be sufficient to detect such a narrow resonance (Figure 3.5b), suggesting that the barium species present in the composition have very large EFGs, consistent with asymmetric non-perovskite barium environments.¹⁴⁴ Taken together, the ¹³³Cs and ¹³⁷Ba NMR results are compelling evidence for no barium incorporation into the CsPbBr₃ perovskite lattice. We expect them to carry over to the CsPbI₂Br composition since the chemical propensity of a cation to participate in substitutional doping has been shown to be halide-independent.^{120,121} Thus, we conclude that the changes in band gap observed using optical spectroscopies are entirely due to the changes in the I/Br ratio in the final perovskite composition rather than barium incorporation.

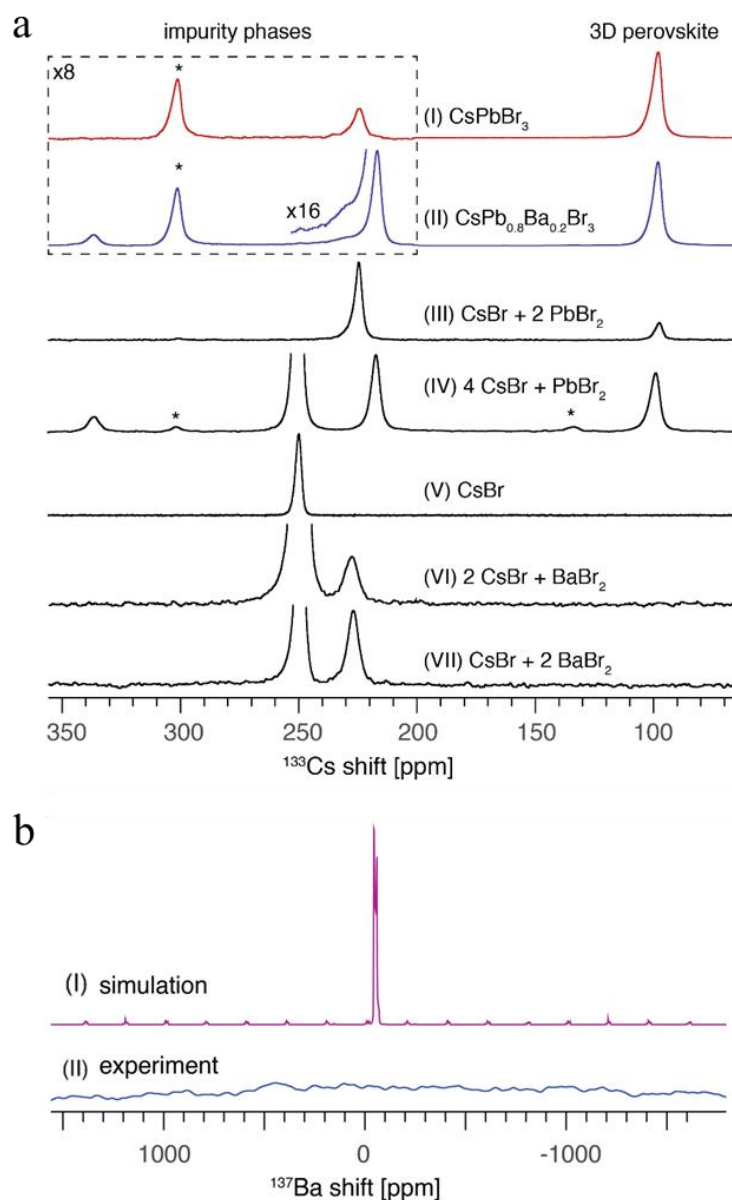


Figure 3.5. Phase segregation analysis. (a) ^{133}Cs echo-detected solid-state MAS NMR spectra at 21.1 T, 298 K and 24 kHz MAS of bulk mechanochemical compositions (I) CsPbBr_3 , (II) $\text{CsPb}_{0.8}\text{Ba}_{0.2}\text{Br}_3$ (note that the formula designates the formal stoichiometry and does not correspond to a pure-phase material), (III) $\text{CsBr} + \text{PbBr}_2$ (1:2), (IV) $\text{CsBr} + \text{PbBr}_2$ (4:1), (V) neat CsBr , (VI) $\text{CsBr} + \text{BaBr}_2$ (2:1), (VII) $\text{CsBr} + \text{BaBr}_2$ (1:2). Asterisks indicate spinning sidebands. The 200 to 350 ppm range in panels a and b is magnified 8 times to evidence the impurity phase. The inset in panel b shows a small amount of a barium-based non-perovskite impurity phase. (b) (I) A simulated NMR spectrum using EFG parameters calculated by fully-relativistic DFT for Ba incorporated on a B-site of CsPbBr_3 . (II) ^{137}Ba echo-detected (CT-selective) solid-state MAS NMR spectrum at 21.7 T, 298 K and 20 kHz MAS of the bulk mechanochemical $\text{CsPb}_{0.8}\text{Ba}_{0.2}\text{Br}_3$ compositions. Similarly, no signal was detected with a non-selective echo.

To quantify the effect of barium addition on the band gap, we plot the band gaps as a function

of barium concentration x in CsPb_{1-x}Ba_xI₂Br. The band gaps are estimated from the wavelength of the maxima in the PL spectra in Figure 3.1c. We observe a linear dependence between the band gaps and barium concentration x (Figure 3.6a), which is described in Equation (1):

$$E_g = 1.92 - 0.27 x \quad (1)$$

Since the photoactive phase in the barium-containing material is still a cesium lead iodide-bromide, we prepared a series of CsPb(I_yBr_{1-y})₃ ($y = 0$ to 1) films with different Br/I ratio, recorded their PL peak wavelengths and converted them to the corresponding band gaps. We plot these band gaps against the iodide fraction y , and again observe a linear relationship as shown in Equation (2):

$$E_g = 2.32 - 0.60 y \quad (2)$$

The empirical equation relating the barium fraction (x) in CsPb_{1-x}Ba_xI₂Br and the iodide fraction (y) in CsPb(I_yBr_{1-y})₃ therefore has Equation (3):

$$y = 0.45 x + 0.667 \quad (3)$$

From this equation, we find that the band gap of the composition formally corresponding to the formula CsPb_{0.8}Ba_{0.2}I₂Br is identical to that of the CsPbI_{2.27}Br_{0.73} perovskite. The XRD characteristic peaks of CsPbI_{2.27}Br_{0.73} and CsPb_{0.8}Ba_{0.2}I₂Br perovskites also both occur at 14.5° and 29.7° (Figure 3.6b). To further clarify the advantage of barium addition on the photovoltaic performance of cesium lead halide PSCs, we prepared devices based on CsPbI_{2.27}Br_{0.73} and 0.8CsPbI₂Br-0.2CsI (i.e. CsPbI₂Br doped with 20 mol% CsI) as references. Their efficiencies were 8.82% and 8.64%, respectively. Both types of PSCs show significantly lower J_{sc} and V_{oc} compared to CsPb_{0.8}Ba_{0.2}I₂Br based solar cells (Figure 3.6c, d). Furthermore, the recorded J - V performance of the devices based on CsPbI₂Br + x BaI₂ ($x = 0, 0.1, 0.2$) shows that the addition of BaI₂ increases the V_{oc} and the PCE (Figure 3.6e), indicating that Ba plays an important role in the improvement of photoelectric property of the corresponding devices. Besides, we found that no PL shift was observed for CsPbBr₃ perovskites by barium addition (Figure 3.6f).

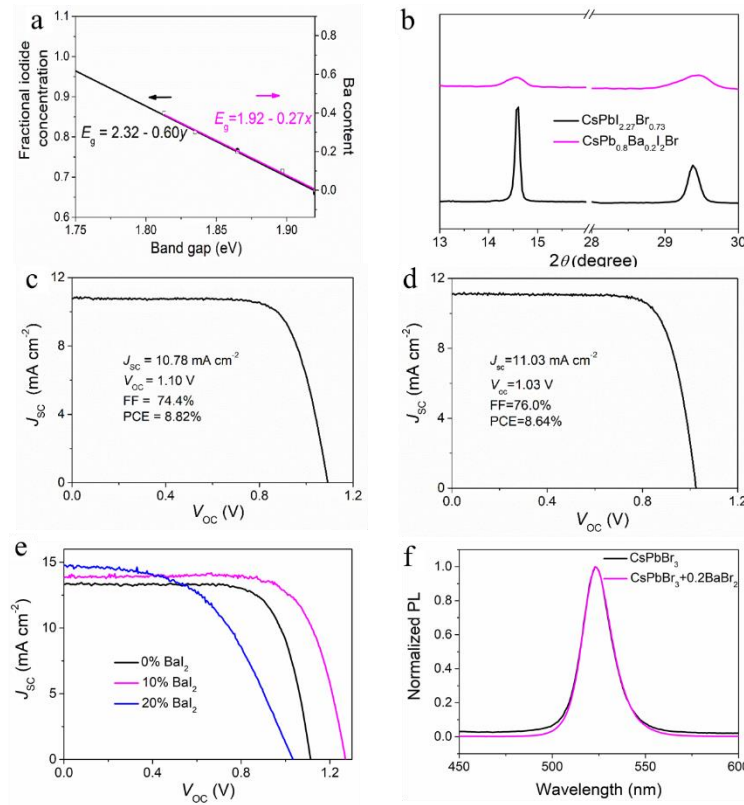


Figure 3.6. Phase segregation analysis. (a) The fractional iodide concentration and barium concentration vs. the experimental band gaps. The linear fits are included in the figure. (b) XRD patterns of CsPbI_{2.27}Br_{0.73} and CsPb_{0.8}Ba_{0.2}I₂Br perovskite films. *J-V* performance of (c) CsPbI_{2.27}Br_{0.73} and (d) 0.8CsPbI₂Br-0.2CsI based inorganic PSCs under 100 mW cm⁻² irradiation. (e) *J-V* curves of CsPbI₂Br based PSCs with different amount of BaI₂ as additive (Measurement was conducted under 100 mW cm⁻² illumination with active area of 0.16 cm²). (f) PL spectra of CsPbBr₃ inorganic perovskite films with and without barium.

Meanwhile, based on first-principles electronic structure calculations (Figure 3.7), we found that the band gaps of barium-doped perovskites CsPb_{1-x}Ba_xI₂Br should increase, rather than decrease. This is expected from the much larger band gap of CsBaI₂Br than that of CsPbI₂Br and the type-I bands alignment between them. In addition, simulation of hypothetical alloys of CsPb_{1-x}Ba_xI₂Br ($x = 0, 0.1, 0.2, 0.3, 0.4, 1$) gives positive formation energies with respect to decomposition into CsPbI₂Br and CsBaI₂Br (see Methods section and Supplementary Figure 3.12). This indicates solid-solution miscibility gap and phase-separation behavior at low and room temperatures, consistent with the inability of Ba doped into perovskite lattice demonstrated experimentally. According to the Hume-Rothery rules,³⁶ formation of solid solution needs similar atomic radii, same crystal structures, same electronegativities, same valence states of constituted components. Except for the crystal structure and valence state, the substantial mismatches in the other two factors between Pb and Ba (ionic radii: 1.19 and 1.35 Å for Pb²⁺ and Ba²⁺; electronegativities) are responsible for the phase-separation behavior.

Taken together, the results show that the shift of the XRD peak to higher angles in Figure 3.1a and the red-shifts of PL and UV-Vis spectra in Figure 3.1b and c are entirely due to the change of the I/Br ratio in the perovskite, resulting from barium-induced anion exchange.

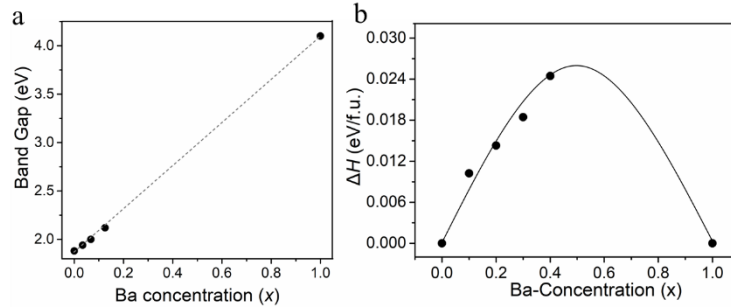


Figure 3.7. Phase segregation analysis. (a) Dependence of the calculated band gaps of the Ba-doped CsPbI₂Br perovskites CsPb_{1-x}Ba_xI₂Br on the barium concentration ($x = 0.03375, 0.0625, 0.125$) with first-principles density functional theory approach assumed that barium was doped into the perovskite lattice. The lowest energy structure of CsPb_{1-x}Ba_xI₂Br was used for the calculations. The dot line represents linear fitting of the data. (b) Calculated formation energies of the alloyed perovskite CsPb_{1-x}Ba_xI₂Br ($x = 0, 0.1, 0.2, 0.3, 0.4, 1$) by using the special quasirandom structure to mimic random disorder within a 200 atom supercell.

In order to map the distribution of the segregated phases in the perovskite films, we conducted energy-dispersive spectroscopy (EDS)-based elemental mapping (Figure 3.8). The CsPb_{0.8}Ba_{0.2}I₂Br perovskite film characterized by SEM (Figure 3.8a) shows a uniform coverage of the perovskite on the substrate and an average crystal size of about 200 nm. The surface is covered with a large number of bright spots (in the white circle). EDS mapping shows that these bright parts contain higher ratio of Ba and Br than the rest, while the dark areas possess more I and Pb. These results are consistent with the phenomenon of phase segregation evidenced by solid-state NMR. Thus, the formal CsPb_{1-x}Ba_xI₂Br stoichiometry does not represent a pure phase material but a mixture of perovskite and barium-rich non-perovskite phases.

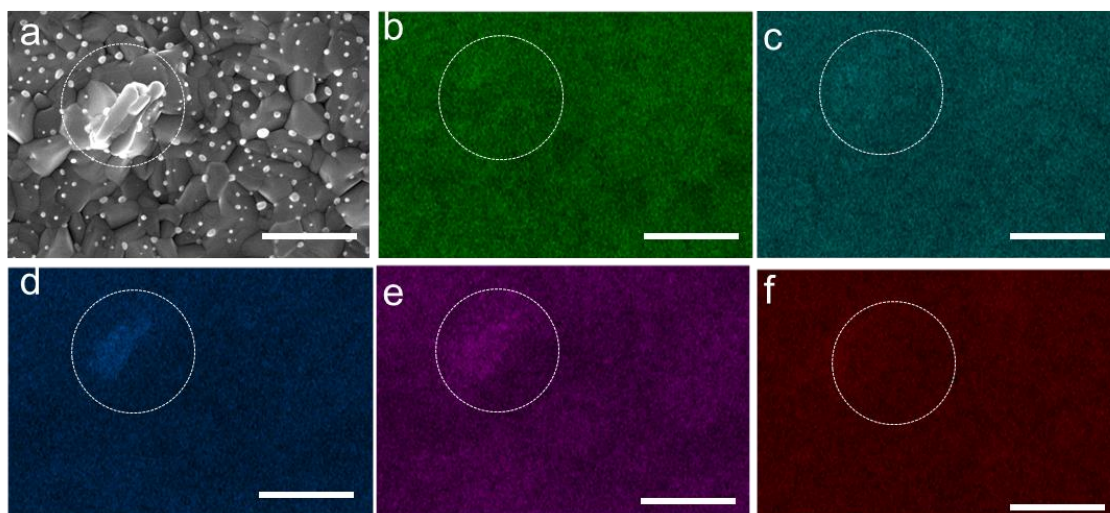


Figure 3.8. Phase segregation analysis. (a) an SEM image of a selected perovskite film area, the scale bar is 500 nm. Elemental distributions of CsPb_{0.8}Ba_{0.2}I₂Br inorganic perovskite film by EDS elemental mapping are shown as: (b) distribution of Pb, (c) distribution of I, (d) distribution of Ba, (e) distribution of Br and (f) distribution of Cs. The scale bars are 500 nm.

3.2.3 Perovskite film morphology and device stability

We also analyze the top-view film morphology by SEM after introducing barium during fabrication of CsPbI₂Br on a mesoporous TiO₂ substrate (Figure 3.9). A pinhole-free and dense pristine CsPbI₂Br film was obtained by carefully controlling the deposition conditions, as described in the experimental section. Upon addition of 10% barium, the perovskite grains become well resolved and the grain boundaries become clear. However, bare TiO₂ surface is visible underneath, evidencing incomplete coverage of the substrate. For a barium molar fraction x of 0.2, we observe full coverage of the substrate with closely packed grains and numerous dots on the film surface. Further increase in the barium content generates pinholes and makes the grain profile blurry, leading to less dense films. Apparently, morphology reconstruction takes place when barium is added into the composition, with $x = 0.2$ leading to optimal morphology for obtaining high performance solar cells.

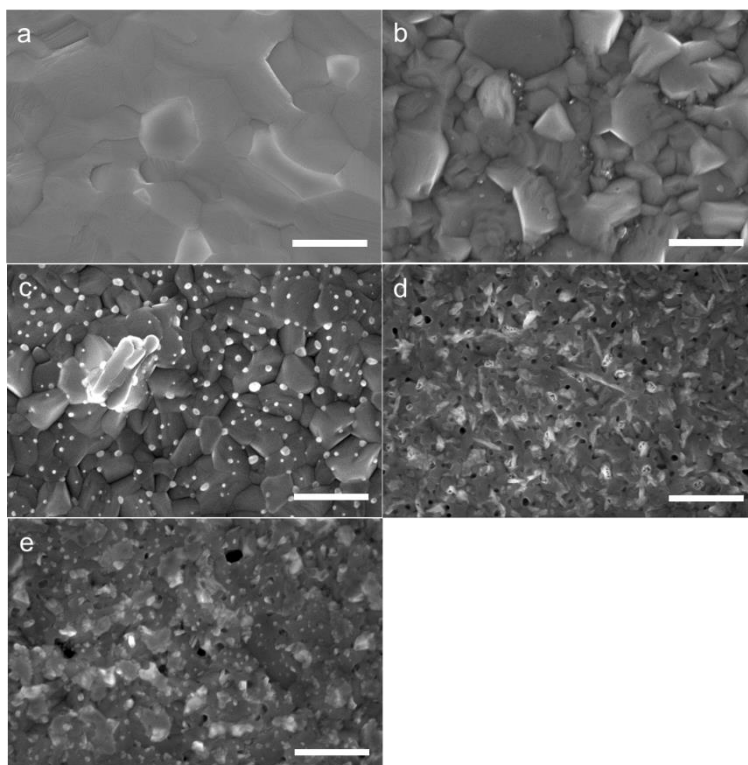


Figure 3.9. Perovskite film morphology. SEM images of CsPb_{1-x}Ba_xI₂Br with different incorporation amount of Ba (from a to e: $x = 0, 0.1, 0.2, 0.3, 0.4$). The scale bars are 500 nm.

To evaluate the stability of the complete devices, one of the best performing and unencapsulated CsPb_{0.8}Ba_{0.2}I₂Br based inorganic PSCs was illuminated under continuous 100 mW cm⁻² white light emitting diode (LED) irradiation in an N₂ atmosphere with maximum power point tracking. The control CsPbI₂Br-based PSC was monitored under identical conditions (Figure 3.10). The CsPb_{0.8}Ba_{0.2}I₂Br based device showed a slow decrease of PCE over time, maintaining approximately 80% of the initial efficiency after 450 hr. During the same testing period, the PCE of CsPbI₂Br based PSC dropped dramatically to 40% of the initial value within 90 hr and eventually less than 20% after 350 hr of illumination. These results indicate that the CsPb_{0.8}Ba_{0.2}I₂Br based PSCs demonstrate better stability than CsPbI₂Br-based devices. Since iodide-rich all-inorganic perovskites are known to be rather sensitive to moisture, we conclude that the enhanced stability of CsPb_{0.8}Ba_{0.2}I₂Br based PSCs is probably due to protection of the film surface with the barium-rich phases or defects reduction within the device.¹⁴⁵

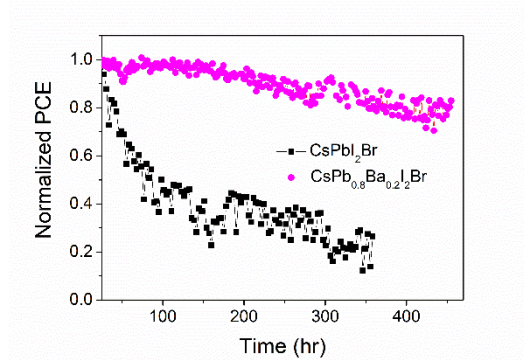


Figure 3.10. Device stability. Stability of the unencapsulated CsPbI₂Br and CsPb_{0.8}Ba_{0.2}I₂Br based PSCs under 100 mW cm⁻² continuous irradiation.

3.3 Summary

In conclusion, we report a function of adding barium to the all-inorganic CsPbI₂Br perovskite and its use as an absorber layer in inorganic PSCs that achieves a PCE of 14.0% under one sun illumination. By applying solid-state NMR, we have shown that barium cannot be incorporated into the perovskite lattice. Rather, it segregates into barium-based non-perovskite phases. This in turn leads to a change in the iodide-to-bromide ratio in the photoactive perovskite layer. This atomic-level insight provides a full explanation of the changes observed in the optical spectra and XRD patterns. Electroluminescence measurements indicate that the non-radiative recombination is effectively inhibited upon the addition of barium, yielding a much higher V_{oc} of 1.33 V and a high electroluminescence EQE value. The addition of barium also improves the quality of perovskite films and leads to an increase in PCE. Our study highlights that phase segregation is a critical design criterion, which should be taken into account and investigated for other additives.

3.4 Experimental section

3.4.1 Preparation method

Preparation of perovskite solutions 259.8 mg CsI, 183.5 mg PbBr₂, 230.5 mg PbI₂ were mixed with 1 ml anhydrous dimethylsulfoxide (DMSO) with continuous heating at 80 °C for 6 hr until a completely clear CsPbI₂Br solution was formed. 391.2 mg BaI₂ and 212.8 mg CsBr were dissolved into a mixture of 1.4 ml DMSO and formamide (v:v=1:1) to form a clear CsBaI₂Br solution. The CsPb_{1-x}Ba_xI₂Br ($x = 0$ to 1) perovskite solutions were prepared by mixing the above two solutions with appropriate ratio in a nitrogen-filled glovebox and alloyed overnight. The 1M solutions of CsPbI_{2.27}Br_{0.73}, 0.8CsPbI₂Br-0.2CsI and CsPbI₂Br + x BaI₂ ($x =$

0.1, 0.2) were also prepared stoichiometrically.

Device fabrication The perovskite device was fabricated with the following procedure. The fluorine-doped tin oxide (FTO) conducting glass (Nippon Cor. Japan) with the square resistance of $10 \Omega \text{ sq}^{-1}$ was cleaned with 2% Hellmanex solution, acetone and ethanol by sonication for 15 min, 10 min and 10 min, separately. The 40 nm thick TiO₂ compact layer was deposited on top of cleaned FTO glass by spray pyrolysis at 450 °C from a precursor solution containing 0.6 ml titanium diisopropoxide bis(acetylacetonate) and 0.4 ml acetoacetate in 9 ml anhydrous ethanol. The 150 nm thick mesoporous TiO₂ layer was then deposited by spin-coating a diluted TiO₂ paste (30 nm particle size, Dyesol) in absolute ethanol at the speed of 5000 rpm for 10 s. These TiO₂ films were dried at 80 °C for 5 min and further sintering process at 450 °C for 1 hr under continuous dry air flow. After cooling down to approximately 100 °C, these films were immediately transferred into glovebox filled with dry air. The CsPb_{1-x}Ba_xI₂Br ($x = 0$ to 1) perovskite films were prepared by spin-coating the aforementioned precursor solutions in a two steps program at 1000 rpm and 3000 rpm for 10 s and 30 s, respectively. The films were then left for 5 min before being annealed at 280 °C for 10 min. After cooling down to room temperature, the spiro-OMeTAD (Merck) chlorobenzene solution (90 mg ml⁻¹) with 20.6 μl bis(trifluoromethylsulfonyl)imide lithium salt (LiTFSI, Sigma-Aldrich, 520 mg ml⁻¹ in acetonitrile) and 35.5 μl 4-tert-butylpyridine (t-BP, Sigma-Aldrich) was spun on top of the perovskite film at 4000 rpm for 20 s. An 80 nm thick Au back-contact metal electrode was finally thermal-evaporated to complete the device construction.

3.4.2 Characterization

X-ray diffraction The perovskite films on mesoporous TiO₂ substrates were prepared exactly as described in the device fabrication section. X-ray diffraction (XRD) patterns were acquired with a PANalytical Empyrean diffractometer in the transmission-reflection mode, using the Cu K α radiation and the Ni β -filter.

Scanning electron microscope The perovskite films were deposited on mesoporous TiO₂ substrates to exactly reflect the true film morphology. A high-resolution scanning electron microscope (SEM) (Zeiss Merlin) with in-lens detector was used for morphology characterization. Energy-dispersive spectroscopy (EDS) was carried out in SEM mode.

Optical characterization UV-Vis measurements were performed on a Varian Cary 5. Photoluminescence spectra were obtained with Fluorolog 322 (Horiba Jobin Yvon Ltd) with the range of wavelength from 500 nm to 800 nm by exciting at 450 nm with a standard 450-W Xenon CW lamp. The samples were mounted at 60° and the emission recorded at 90° from the incident beam path. Time-resolved photoluminescence was performed using Fluorolog 322 spectrofluorometer (Horiba Jobin Yvon Ltd.). A NanoLED-405L (Horiba) laser diode (405 nm)

was used for excitation. The samples were mounted at 60° and the emission collected at 90° from the incident beam path. The detection monochromator was set to 650 nm and the photoluminescence was recorded using a picosecond photodetection module (TBX-04, Horiba Scientific).

Perovskite mechanosynthesis Starting materials were stored inside a glove box under argon. Perovskite powders were synthesized by grinding the reactants in an electric ball mill (Retsch Ball Mill MM-200 using a grinding jar (10 ml) and a ball (ø10 mm) for 30 min at 25 Hz. The resulting powders were annealed at 280 °C for 10 minutes to reproduce the thin-film synthetic procedure. The amounts of reagents taken into the synthesis were as follows:

CsPb_{0.8}Ba_{0.2}Br₃: 0.213 g CsBr (1.00 mmol), 0.059 g BaBr₂ (0.20 mmol), and 0.294 g PbBr₂ (0.80 mmol).

CsPbBr₃: 0.213 g CsBr (1.00 mmol) and 0.367 g PbBr₂ (1.00 mmol).

CsBr + 2 PbBr₂: 0.107 g CsBr (0.50 mmol) and 0.367 g PbBr₂ (1.00 mmol).

4 CsBr + PbBr₂: 0.213 g CsBr (1.00 mmol) and 0.092 g PbBr₂ (0.25 mmol).

2 CsBr + BaBr₂: 0.213 g CsBr (1.00 mmol) and 0.149 g BaBr₂ (0.5 mmol).

1 CsBr + 2 BaBr₂: 0.107 g CsBr (0.50 mmol) and 0.297 g BaBr₂ (1 mmol).

Solid-state NMR measurements Room temperature ¹³³Cs (181.1 MHz) and ¹³⁷Ba (100.0 MHz) NMR spectra were recorded on a Bruker Avance Neo 21.1 T spectrometer equipped with a 3.2 mm CPMAS probe. ¹³³Cs shifts were referenced to 1 M aqueous solution of CsCl, using solid CsI ($\delta = 271.05$ ppm) as a secondary reference.¹⁴⁶ ¹³⁷Ba shift were referenced to solid BaZrO₃ using BaO as a secondary reference (481 ppm).¹⁴³ Quantitative ¹³³Cs spectra were acquired using a recycle delay of 450 s.

Electronic structure calculations of Ba-doped CsPbI₂Br perovskites

Electronic band structure calculations of Ba-doped CsPbI₂Br perovskites were within the framework of density functional theory (DFT) by using plane-wave pseudopotential methods as implemented in the Vienna Ab initio Simulation Package.^{147,148} The electron-ion interactions were described by the projected augmented wave pseudopotentials with the 6s (Cs), 5s and 5p (Br), 5s and 5p (I), 6s and 6p (Pb) electrons treated as valence electrons. We used the generalized gradient approximation of Perdew-Burke-Ernzerhof (PBE) form¹⁴⁹ as exchange-correlation functional. The kinetic energy cutoff for the plane wave basis of 300 eV was used and the *k*-point meshes of spacing were set to $2\pi \times 0.04 \text{ \AA}^{-1}$ for electronic Brillouin zone integration. The structures of Ba-doped perovskites CsPb_{1-x}Ba_xI₂Br ($x = 0.03375, 0.0625, 0.125$) were constructed through the 2x2x2, 2x1x2, 1x1x2 supercells of the CsPbI₂Br unit cell, in which Pb atoms are randomly substituted by Ba atoms according to Ba concentration *x*. The

structures are optimized through total energy minimization with the residual forces on the atoms converged to below 0.05 eV/Å. The spin-orbit coupling was included in the electronic structure calculations. Though the DFT-PBE approach is known to underestimate the band gaps of semiconductors due to the self-interaction error issue, but in the current case it is reliable to predict the correct trend on the calculated band gaps of Ba-doped perovskites CsPb_{1-x}Ba_xI₂Br changing with Ba concentration x .

The hypothetical alloys of CsPb_{1-x}Ba_xI₂Br ($x = 0, 0.1, 0.2, 0.3, 0.4, 1$) were simulated through the special quasirandom structure¹⁵⁰ to mimic random disorder within a 200 atom supercell. The alloy formation energy is defined as $\Delta H = E(\text{CsPb}_{1-x}\text{Ba}_x\text{I}_2\text{Br}) - xE(\text{CsPbI}_2\text{Br}) - (1-x)E(\text{CsBaI}_2\text{Br})$, where $E(\text{CsPb}_{1-x}\text{Ba}_x\text{I}_2\text{Br})$, $E(\text{CsPbI}_2\text{Br})$, and $E(\text{CsBaI}_2\text{Br})$ refer to the free energy of CsPb_{1-x}Ba_xI₂Br, CsPbI₂Br, and CsBaI₂Br phases, respectively. We assumed the 3D perovskite as the structure of CsBaI₂Br to evaluate ΔH . The resulted value is positive, indicating a phase separation condition. If there was the ground-state structure with the even lower energy of CsBaI₂Br, we can expect that the ΔH would be even larger in the positive magnitude. Therefore, with the assumption of CsBaI₂Br being 3D perovskite, our calculations give a reasonable evaluation of the phase separation condition. The positive ΔH for all the Ba fractions indicates that there is no stable configuration for the alloyed perovskites at 0 K, and phase separation will occur. This may be attributed to the substantial ionic radius and electronegativity mismatch between Pb and Ba.

X-ray photoelectron spectroscopy The perovskite films were deposited on plain glass substrates as described above. X-Ray Photoelectron Spectroscopy (XPS) measurements were carried out using a PHI VersaProbe II scanning XPS microprobe (Physical Instruments AG, Germany). Analysis was performed using a monochromatic Al K α X-ray source of 24.8 W power with a beam size of 100 μm . The spherical capacitor analyser was set at 45° take-off angle with respect to the sample surface. The pass energy was 46.95 eV yielding a full width at half maximum of 0.91 eV for the Ag 3d 5/2 peak. Curve fitting was performed using the PHI Multipak software.

Photovoltaic performance The PSCs were tested with a 450 W xenon light source (Oriel). The light intensity was calibrated by a silicon photodiode equipped with an IR-cutoff filter (KG3, Schott) and was recorded for each measurement. The current-voltage curves (J - V curves) of the devices were recorded by applying an external voltage bias with Keithley 2400 to give the corresponding current response. A black metal mask with an area of 0.16 cm² was applied to define the active area of the cells and to avoid the overestimation of the light input.

Incident photon-to-current conversion efficiency (IPCE) measurements were carried from the monochromatic visible photons, from Gemini-180 double monochromator Jobin Yvon Ltd. (UK), powered by a 300 W xenon light source (ILC Technology, USA) superimposed on a 1

mW cm⁻² LED light. The monochromatic incident light was passed through a chopper running at 8 Hz frequency and the on/off ratio was measured by an operational amplifier.

Stability Stability measurements were performed with a Biologic MPG2 potentiostat under a full AM 1.5 Sun-equivalent white LED lamp. The devices were masked to 0.16 cm² and were connected to a separate channel of a potentiostat. A continuous flow of dry nitrogen gas was flushed into the custom-built airtight weathering chamber as the sample holder. The devices were measured *in situ* with a maximum power point (MPP) tracking routine under continuous illumination. The MPP was updated every 10 s by a standard perturb-and-observe method. A Peltier element in direct contact with the films was used to control the temperature of the devices. A Pt100 thermometer inserted between the Peltier element and the film was used to measure the temperature of the devices. Every 30 minutes a *J-V* curve was recorded in order to track the evolution of individual *J-V* parameters. The setup is centrally-controlled through a LabView interface allowing for automatic programming of experiments (temperature, illumination, atmosphere, electronic measurements).

Chapter 4 Intermediate phase enhances inorganic perovskite and metal oxide interface for efficient photovoltaics

This chapter was adapted from the following article with the permission of all co-authors and the journal.

Postprint version of the article: Zhang, J.[#]; Wang, Z.^{*#}; Mishra, A.; Yu, M.; Shasti, M.; Tress, W.; Kubicki, D. J.; Avalos, C. E.; Lu, H.; Liu, Y.; Carlsen, B. I.; Agarwalla, A.; Wang, Z.; Xiang, W.; Emsley, L.; Zhang, Z.; Grätzel, M.; Guo, W.^{*}; Hagfeldt, A.^{*}, Intermediate phase enhances inorganic perovskite and metal oxide interface for efficient photovoltaics. *Joule* 2020, 4 (1), 222-234.

[#] These authors contributed equally to this work. ^{*} The corresponding authors

My contribution: Z. W. and J. Z. conceived the idea of this project, designed the experiments and wrote the manuscript. J. Z., Z. W. and M. S. performed the fabrication, optimization and characterization of films and devices. W. T., Z. S. W and Z. W. performed EL, PL measurements and analyzed the data. Z. W. and J. Z. performed SEM imaging, XRD measurements, and XPS measurements. Z. W. and Y. L. analyzed the XPS data. Z. W. and A. A. performed the stability test. B. I. C. and Z. W. performed TRPL measurements and analyzed the data.

Interfacial modification is crucial to fully develop the potential of semiconductor devices, including the revolutionary halide perovskite-based optoelectronics, such as photovoltaics, light-emitting diodes, and photodetectors. The all-inorganic halide perovskites, potential long-term stable photovoltaic materials, are suffering from poor interfacial contact with metal oxide charge selective layer, severely limiting the power conversion efficiency and stability of inorganic perovskite solar cells. Here, we proposed an intermediate phase engineering strategy to improve the inorganic perovskite/metal oxide interface by utilizing volatile salts. The introduction of organic cations (such as methylammonium and formamidinium), which can be doped into the perovskite lattice, leads to the formation of an organic-inorganic hybrid perovskite intermediate phase, promoting a robust interfacial contact. A champion CsPb(I_{0.75}Br_{0.25})₃-based device with a power conversion efficiency of 17.0% and an open-circuit voltage of 1.34 V was realized, implying that a record of over 65% of the Shockley-Queisser efficiency limit is achieved.

4.1 Introduction

The unique properties of halide perovskite materials including long charge carrier diffusion length, high light-harvesting efficiency, and tunable band gap make them ideal materials for photoelectronic applications.^{1,2,5-7,17,151} To date, the certified power conversion efficiency (PCE) of organic-inorganic hybrid perovskite solar cells (PSCs) has reached 25.2%, which is higher than that of polycrystalline silicon solar cells.^{1,3,4,10,65,73,109,110,152,153} Despite the encouraging PCE, the intrinsic instability of organic-inorganic hybrid perovskite (OIHP) materials, such as the degradation under moisture and heat, is hindering further industrialization of PSCs.^{111,134} By replacing the volatile organic cations with an inorganic cesium cation (Cs^+), the all-inorganic cesium lead halide perovskites, denoted as CsPbX_3 ($\text{X} = \text{Br}, \text{I}$), are attracting extensive research due to their potential to improve the stability of PSCs intrinsically.^{12,55,61,99,101,112} Our statistics show that the reported PCE of high-performance inorganic PSCs without organic residues or modification in perovskite layers ($\leq 60\%$ of the Shockley-Queisser (S-Q) efficiency limit) is lower than that of organic-inorganic hybrid PSCs ($\leq 65\%$ of the S-Q efficiency limit) in the band gap range between 1.72 eV to 2.3 eV (Figure 4.1 and Table S4.1).^{14,16,107,109,135,154,155}

Interfacial contact plays an important role in high performance organic-inorganic PSCs.^{156,157} However, it has not been thoroughly studied in inorganic PSCs, especially the interfacial contact of inorganic perovskite and the metal oxide charge transport layer, such as titanium oxide (TiO_2) and tin oxide (SnO_2). The interfacial contact is closely related to the chemical interaction between the perovskite and metal oxide layers.¹⁵⁶ This leads to a potentially larger challenge in the inorganic perovskite/metal oxide interfacial contact compared to that of OIHP. Various organic additives have been employed to modify the interfacial contact and improve the efficiency in PSCs.^{158,159} However, in inorganic perovskites, the existence of organic components compromises the original premise of outstanding thermal stability.⁴⁷

Here, we report an intermediate phase engineering (IPE) strategy by introducing volatile organic salts into the inorganic perovskite precursor solution, leading to the formation of an OIHP intermediate phase with strong hydrogen bonding at the perovskite/metal oxide interface. It optimizes the interfacial contact between all-inorganic perovskite and metal oxide of mesoscopic (meso-) and planar architectures, and also retains the thermal stability of all-inorganic perovskite without organic residues. With this strategy, the PCE of the champion device based on $\text{CsPb}(\text{I}_{0.75}\text{Br}_{0.25})_3$ is 17.0%. It corresponds to 66% of the S-Q efficiency limit, which is higher than that of high-performance inorganic PSCs without organic residues or modification in perovskite layers from previous literature ($\leq 60\%$) and comparable to that of organic-inorganic PSCs ($\leq 65\%$) with a similar band gap (1.72 eV to 2.3 eV). The open-circuit voltage (V_{oc}) of 1.34 V for the champion device in planar tin oxide (SnO_2) architecture is up to

86% of the theoretical V_{oc} , which is also the highest reported ratio in inorganic PSCs.

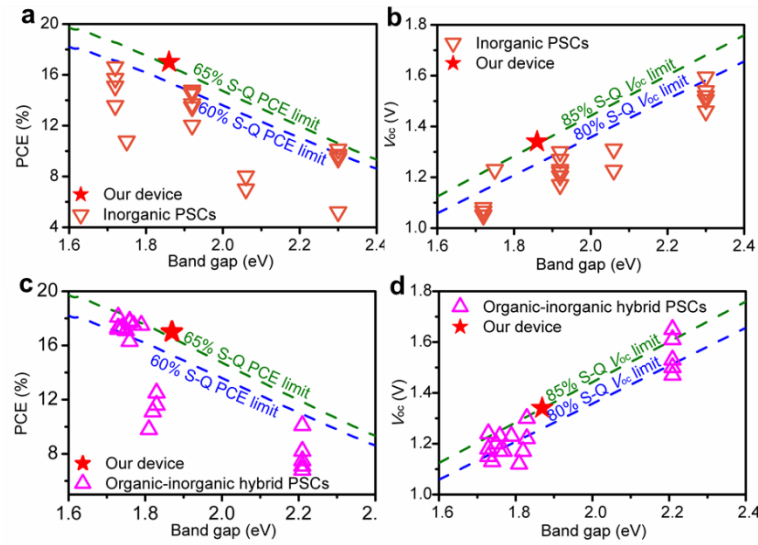


Figure 4.1. Statistics of high-performance PSCs in recent literatures. a-d, PCE (a, c) and V_{oc} (b, d) of PSCs without organic residues or modification in perovskite layers and wide band gap (1.72 eV-2.3 eV) organic-inorganic hybrid PSCs and our devices. The dashed lines were drawn according to Shockley-Queisser theory. ¹¹(ref. Shockley, W., and Queisser, H.J. (1961). Detailed balance limit of efficiency of p-n junction solar cells. J. Appl. Phys. 32, 510-519.)

4.2 Results and discussion

4.2.1 Film morphology and photoelectric performance

The perovskite photoactive layer $\text{CsPb}(\text{I}_{0.75}\text{Br}_{0.25})_3$ was obtained by a one-step spin-coating method and further rested 60 min at room temperature followed by 330 °C for 5min in glove box. Uniform and pinhole-free film is obtained (Figure 4.2a.). However, based on this film, a PCE of only 10.5% was achieved from a meso-device with an architecture of Fluorine-doped tin oxide (FTO)/compact- TiO_2 (c- TiO_2)/meso- TiO_2 /CsPb($\text{I}_{0.75}\text{Br}_{0.25}$)₃/2,2',7,7'-tetrakis(N,N-di-p-methoxyphenyl-amine)-9,9'-spirobifluorene (spiro-OMeTAD)/Au (Figure 4.2c). Cross-sectional scanning electron microscopy (SEM) of the device (Figure 4.2b) shows visible voids at the perovskite/meso- TiO_2 interface which reveals poor interfacial contact. Previous reports prove that enhancing the perovskite/meso- TiO_2 interaction benefits the interfacial contact.¹⁵⁶ Thus, a volatile organic salt, formamidinium acetate (FAOAc), is introduced into CsPb($\text{I}_{0.75}\text{Br}_{0.25}$)₃ precursor solution as FA^+ interacts with TiO_2 via strong hydrogen bonding.¹⁶⁰ FA^+ can be doped into the inorganic perovskite lattice and the initial film is present, as an OIHP intermediate phase. Then FAOAc can be fully removed during annealing at 280 °C and an all-inorganic perovskite film is obtained (details in the following characterization of the IPE

process of main context). For simplicity, the preparation process of the perovskite films is named as IPE. The optimized $\text{CsPb}(\text{I}_{0.75}\text{Br}_{0.25})_3\text{-0.5FAOAc}$ film (IPE film) is uniform and pinhole-free, and the meso- TiO_2 is penetrated completely by perovskite as shown in Figure 4.2d-e, which suggests a high-quality perovskite/meso- TiO_2 interfacial contact. According to X-ray diffraction (XRD) measurements, the characteristic peaks of the $\text{CsPb}(\text{I}_{0.75}\text{Br}_{0.25})_3\text{-0.5FAOAc}$ film are identical to those of the control $\text{CsPb}(\text{I}_{0.75}\text{Br}_{0.25})_3$ film at $2\theta = 14.62^\circ$ and 29.47° , which demonstrates the formation of a pure $\text{CsPb}(\text{I}_{0.75}\text{Br}_{0.25})_3$ perovskite phase (Figure 4.2f). The champion meso-device shows a PCE of 15.0% with a stabilized power output (SPO) of 14.1% and a moderate hysteresis (Figure 4.2c-g). The V_{oc} increases significantly from 1.03 V for the control device to 1.20 V for the $\text{CsPb}(\text{I}_{0.75}\text{Br}_{0.25})_3\text{-0.5FAOAc}$ device and the short-circuit current (J_{sc}) also increases from 14.2 mA cm^{-2} to 15.6 mA cm^{-2} . Incident photon-to-current conversion efficiency (IPCE) measurements carried out on the $\text{CsPb}(\text{I}_{0.75}\text{Br}_{0.25})_3\text{-0.5FAOAc}$ device shows an integrated current density of 15.5 mA cm^{-2} , which agrees with the current density–voltage (J - V) scanning result (Figure 4.2h). The fill factor (FF) was also improved to 79.9% for the IPE device compared to 72.0% for the control device. A statistical analysis of the photovoltaic parameters of 46 devices demonstrates the good reproducibility of high-performance IPE devices (Figure 4.2i-l).

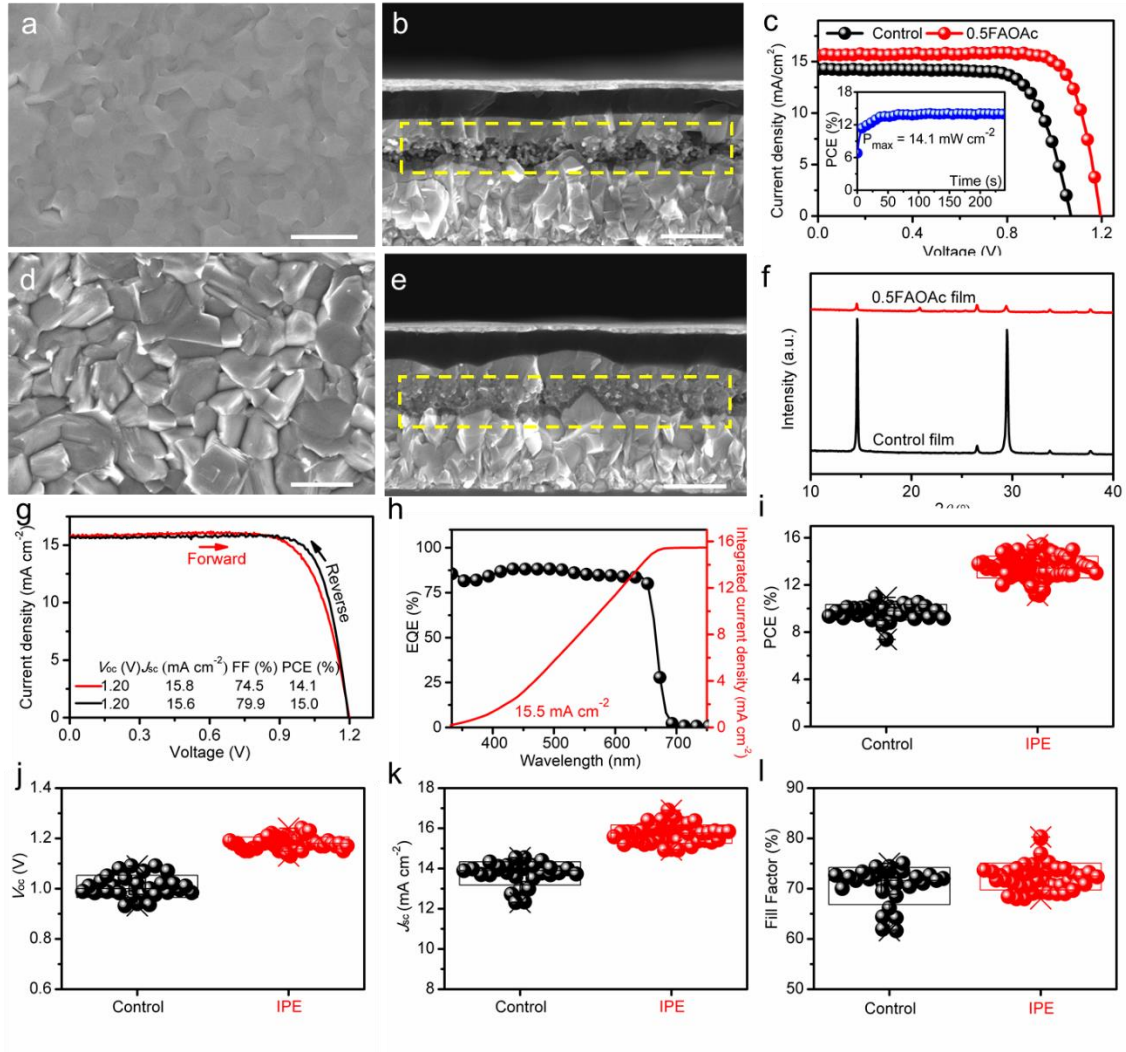


Figure 4.2. Morphology, structure and photoelectric performance. (a, b) Top-view scanning and cross-sectional scanning electron microscopy (SEM) images of control $\text{CsPb}(\text{I}_{0.75}\text{Br}_{0.25})_3$ film and device, respectively. Scale bar = 1 μm for (a), and scale bar = 500 nm for (b). (c) the current density–voltage (J - V) curves of control and $\text{CsPb}(\text{I}_{0.75}\text{Br}_{0.25})_3$ -0.5FAOAc devices. The inset shows the stabilized power output (SPO) of the $\text{CsPb}(\text{I}_{0.75}\text{Br}_{0.25})_3$ -0.5FAOAc device for 240 s. (d, e) Top-view and cross-sectional SEM images of $\text{CsPb}(\text{I}_{0.75}\text{Br}_{0.25})_3$ -0.5FAOAc film and device, respectively. Scale bar = 1 μm for (d), and scale bar = 500 nm for (e). (f) X-ray diffraction (XRD) spectra of annealed control and $\text{CsPb}(\text{I}_{0.75}\text{Br}_{0.25})_3$ -0.5FAOAc films. (g), J - V curves for a meso-device of $\text{CsPb}(\text{I}_{0.75}\text{Br}_{0.25})_3$ -0.5FAOAc measured by forward (short circuit \rightarrow open circuit) and reverse (open circuit \rightarrow short circuit) scans. Measurement was conducted under 100 mW cm^{-2} illumination with active area of 0.16 cm^2 . (h) Incident photon-to-current conversion efficiency of a $\text{CsPb}(\text{I}_{0.75}\text{Br}_{0.25})_3$ -0.5FAOAc device (black) and the integrated short-circuit current density (red). (i-l) Statistics of PCE, V_{oc} , J_{sc} , and FF of the control devices (32 samples) and the IPE devices (46 samples) in mesoscopic structure.

Time-resolved photoluminescence spectra (TRPL) of control film and IPE film on glass and meso- TiO_2 were conducted to evaluate the quality of films and interfaces, respectively. As

shown in Figure 4.3a-b, the carrier life time of IPE film on glass is comparable to that of control film, while the carrier life time of IPE film on meso-TiO₂ is lower than that of control film, which indicates a better interfacial contact.

Moreover, electrochemical impedance spectroscopy (EIS) was carried out in the dark to investigate the charge recombination. Figure 4.3c-d shows that the recombination resistance of IPE device is one order of magnitude larger than that of the control device at a bias voltage (forward bias) from 0.8 V to 1.0 V, which is attributed to the reduction of non-radiative recombination and traps.¹⁶¹ The XRD in Figure 4.3f shows that the crystallinity of control film is stronger than that of IPE film. Thus, we attribute the improvement of PCE and the reduction of traps for IPE devices to interfacial improvement rather than the change of bulk film.

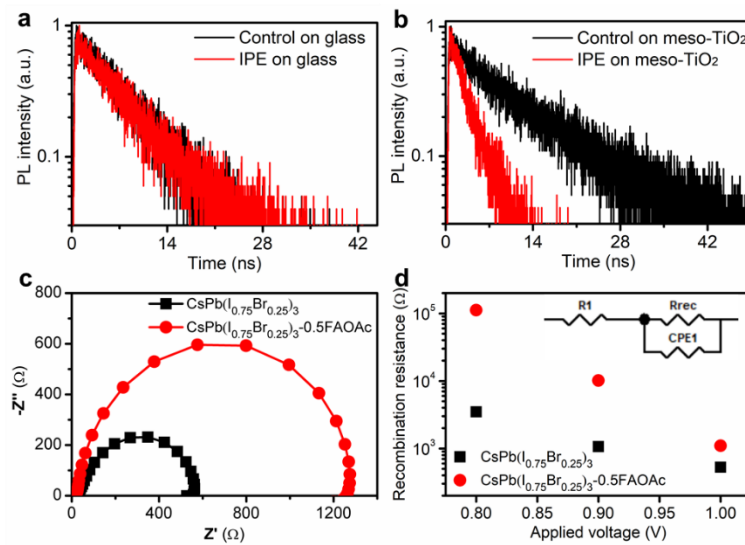


Figure 4.3. Charge transfer properties. (a, b) Time-resolved photoluminescence spectra of control and IPE films on glass and meso-TiO₂ substrates, respectively. (c) Electrochemical impedance spectroscopy (EIS) spectra (Nyquist plots) of control and IPE devices with bias voltage of 1 V under dark, the frequency range is 100 kHz to 0.1 Hz. (d) Recombination resistances under different bias voltage under dark derived from Nyquist plots for control and IPE devices. A simplified equivalent circuit (inset) with one resistance (R_1) and a resistance (R_{rec})–capacitance (C_1) in series where the latter R – C component, assigned to a low frequency range, was used to estimate the recombination resistance at meso-TiO₂/perovskite interfaces.

4.2.2 Characterization of the IPE process

In order to verify the existence of an intermediate phase process, we carried out solid-state magic angle spinning (MAS) nuclear magnetic resonance (NMR) measurements on bulk mechanochemical perovskites as well as thin films. We and others have recently shown that solid-state NMR is a sensitive tool to unambiguously identify cation incorporation^{114,120,135} and halide mixing,¹¹⁵ as well as to study disorder and dynamics in organic-inorganic hybrid and all-

inorganic lead halide perovskites.^{162,163}

Here, we use CsPbBr_3 as a model perovskite because it is structurally similar to $\text{CsPb}(\text{I}_{0.75}\text{Br}_{0.25})_3$. Moreover, spectral features in CsPbBr_3 are well-resolved, unlike in $\text{CsPb}(\text{I}_{0.75}\text{Br}_{0.25})_3$ where chemical disorder leads to very broad ^{133}Cs resonances.¹³⁵

We firstly check whether the doping with FAOAc leads to the incorporation of FA^+ or OAc^- (as a pseudohalide^{164,165}) into the perovskite lattice of CsPbBr_3 . Figure 4.4a shows ^{133}Cs MAS NMR spectra of $\text{Cs}_{1-x}\text{FA}_x\text{PbBr}_3$ ($x = 0, 0.05, 0.10, 0.25, 0.50$). The undoped CsPbBr_3 exhibits a relatively narrow (full width at half maximum of 400 Hz) peak at 101.7 ppm. Upon addition of FA^+ , the peak shifts to lower ppm values and progressively broadens (the fitted values in Table 4.1), indicating the formation of mixed Cs/FA perovskite phases. The broadening is due to the presence of cesium sites with different numbers of nearest neighbour FA^+ in the neighbouring cubo-octahedral cages. There are no other peaks present in the spectra, indicating that the mixed Cs/FA alloys are phase pure. We have thus shown that FA^+ can be incorporated into the CsPbBr_3 perovskite lattice up to at least 50 mol%.

Figure 4.4a (VI) shows the ^{133}Cs spectrum of CsPbBr_3 doped with 50 mol% of $\text{Pb}(\text{OAc})_2$ ($\text{CsPbBr}_3\text{-}0.5\text{Pb}(\text{OAc})_2$). The peak position (~ 102 ppm) and its width (~ 400 Hz) are within error unchanged with respect to neat CsPbBr_3 , indicating that the OAc^- is not incorporated into the perovskite lattice. In addition, we do not observe the formation of CsOAc , which would lead to the appearance of a peak at 86 ppm as shown in Figure 4.4a (VII). We have therefore clearly shown that the acetate ion has no propensity to incorporate into CsPbBr_3 as a pseudohalide. The ^{133}Cs spectrum of $\text{Cs}_{0.80}\text{FA}_{0.20}\text{OAc}$ in Figure 4.4b shows that the peak position (86 ppm) and its width (173 ± 9 Hz) are within the experimental error unchanged with respect to those of neat CsOAc (86 ppm and 155 ± 6 Hz, respectively), indicating that the FA is not incorporated into the CsOAc lattice.

We then look at $\text{CsPbBr}_3\text{-}0.5\text{FAOAc}$, corresponding to the optimized composition in this work. The mechanochemical initial $\text{CsPbBr}_3\text{-}0.5\text{FAOAc}$ composition exhibits three peaks: at 78 (broad shoulder), 88 and 152 ppm. The first two broad peaks are located between those of CsPbBr_3 and $\text{Cs}_{0.5}\text{FA}_{0.5}\text{PbBr}_3$ and correspond to the disordered mixed-cation $\text{Cs}_{1-x}\text{FA}_x\text{PbBr}_3$ 3D perovskite ($0 < x < 0.5$) and the presence of an overlapping CsOAc signal cannot be excluded. The peak at 152 ppm does not correspond to any of the known phases in the CsBr-PbBr_2 family. Since its position (152 ppm) is intermediate with respect to the pure 3D CsPbBr_3 perovskite (101.7 ppm) and the 0D non-perovskite Cs_4PbBr_6 phase (224.9 ppm)¹⁶⁶, we suggest it might be an intermediate of a not fully assembled 3D-like phase since structural heterogeneity is expected in insufficiently annealed samples. The annealed $\text{CsPbBr}_3\text{-}0.5\text{FAOAc}$ yields only one peak at 103 ppm, which corresponds to undoped CsPbBr_3 .

In order to investigate the composition of the thermally decomposed organic products formed

during annealing at 280 °C, we collected the vaporized components on a glass slide and acquired a liquid-state ^1H NMR spectrum in DMSO- d_6 (Figure 4.4c). The spectrum matches that of FAOAc (Figure 4.4c), indicating that FAOAc evaporates during high-temperature annealing.

In addition, we collected the powders from $\text{CsPb}(\text{I}_{0.75}\text{Br}_{0.25})_3\text{-0.5FAOAc}$ for solid-state ^1H MAS NMR measurements (Figure 4.4d). The powder from the initial $\text{CsPb}(\text{I}_{0.75}\text{Br}_{0.25})_3\text{-0.5FAOAc}$ films shows a peak corresponding to unreacted FAOAc at 2.0 ppm and a very narrow peak of residual DMSO at ~ 3.2 ppm. Annealing at 280 °C leads to the disappearance of both these peaks, indicating that FAOAc is no longer present in the material. High-temperature annealing therefore leads to the removal of FA from the $\text{CsPb}(\text{I}_{0.75}\text{Br}_{0.25})_3$ perovskite lattice and a recovery of the parent all-inorganic structure.

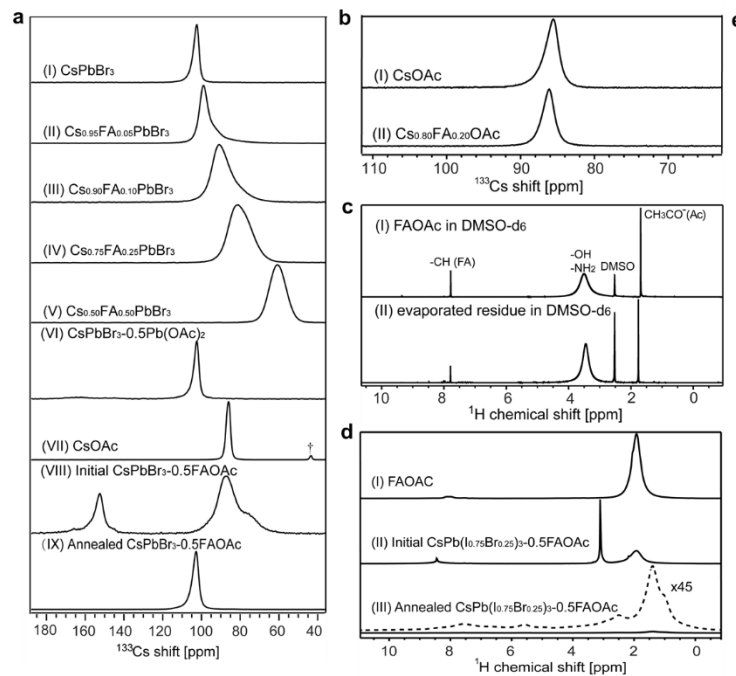


Figure 4.4. Characterizations of intermediate phase engineering (IPE) process by nuclear magnetic resonance (NMR) measurements. (a) Solid-state magic angle spinning (MAS) nuclear magnetic resonance (NMR) characterization of the materials. Echo-detected ^{133}Cs spectra at 21.1 T, 298 K and 20 kHz MAS of (I) CsPbBr_3 , (II) $\text{Cs}_{0.95}\text{FA}_{0.05}\text{PbBr}_3$, (III) $\text{Cs}_{0.90}\text{FA}_{0.10}\text{PbBr}_3$, (IV) $\text{Cs}_{0.75}\text{FA}_{0.25}\text{PbBr}_3$, (V) $\text{Cs}_{0.50}\text{FA}_{0.50}\text{PbBr}_3$, (VI) $\text{CsPbBr}_3\text{-0.5Pb(OAc)}_2$, (VII) CsOAc , (VIII) Initial $\text{CsPbBr}_3\text{-0.5FAOAc}$, (IX) Annealed $\text{CsPbBr}_3\text{-0.5FAOAc}$. The dagger symbol (†) indicates an impurity. (b) MAS NMR characterization of the materials. Echo-detected ^{133}Cs spectra at 11.74 T, 298 K and 20 kHz MAS of CsOAc and $\text{Cs}_{0.80}\text{FA}_{0.20}\text{OAc}$. (c) Liquid-state ^1H spectra at 9.4 T and 298 K of (I) neat FAOAc in DMSO- d_6 , (II) the evaporated component formed during annealing at 280 °C of $\text{CsPbBr}_3\text{-0.5FAOAc}$, dissolved in DMSO- d_6 . The chemical shifts are as follows: (I) Ac (1.6 ppm), -OH/NH $_2$ (3.5 ppm), CH (7.7 ppm), (II) Ac (1.7 ppm), -OH/NH $_2$ (3.4 ppm), CH (7.7 ppm). The spectrum was referenced to the residual DMSO signal at 2.50 ppm (quintet). (d) Solid-state MAS NMR characterization of the materials. Echo-detected ^1H MAS NMR spectra at 21.1 T, 298 K and 20 kHz MAS of (I) FAOAc, (II) Initial $\text{CsPb}(\text{I}_{0.75}\text{Br}_{0.25})_3\text{-0.5FAOAc}$, (III) Annealed $\text{CsPb}(\text{I}_{0.75}\text{Br}_{0.25})_3\text{-0.5FAOAc}$. The spectrum was referenced to the residual DMSO signal at 2.50 ppm (quintet).

T, 298 K and 20 kHz MAS of (I) neat FAOAc, (II) initial $\text{CsPb}(\text{I}_{0.75}\text{Br}_{0.25})_3$ -0.5FAOAc powder from solution process, (III) annealed $\text{CsPb}(\text{I}_{0.75}\text{Br}_{0.25})_3$ -0.5FAOAc powder from solution process. The dashed line is the spectrum magnified 45-fold to show the trace residual protons in the sample.

Table 4.1: ^{133}Cs shifts and peak widths of the spectra reported in Figure 4.4 and Figure 4.7.

Compound	^{133}Cs shift [ppm]	FWHM [Hz]
CsPbBr_3	101.7	400
$\text{Cs}_{0.95}\text{FA}_{0.05}\text{PbBr}_3$	99.2	650
$\text{Cs}_{0.90}\text{FA}_{0.10}\text{PbBr}_3$	91.1	1330
$\text{Cs}_{0.85}\text{FA}_{0.15}\text{PbBr}_3$	84.2	1650
$\text{Cs}_{0.80}\text{FA}_{0.20}\text{PbBr}_3$	82.8	1690
$\text{Cs}_{0.75}\text{FA}_{0.25}\text{PbBr}_3$	80.5	1630
$\text{Cs}_{0.50}\text{FA}_{0.50}\text{PbBr}_3$	60.2	1210
CsPbBr_3 -0.2 $\text{Pb}(\text{OAc})_2$	102.1	410
CsPbBr_3 -0.5 $\text{Pb}(\text{OAc})_2$	101.9	380
CsOAc	86	155±6
$\text{Cs}_{0.80}\text{FA}_{0.20}\text{OAc}$	86	173±9
Initial CsPbBr_3 -0.5FAOAc	78	1084
	88	1269.4
	152	597.5
Annealed CsPbBr_3 -0.5FAOAc	102.1	440
$\text{Cs}_{0.5}\text{MA}_{0.5}\text{PbBr}_3$	64.9	532
$\text{Cs}_{0.90}(\text{NH}_4)_{0.10}\text{PbBr}_3$	Component 1: 102.2	277
	Component 2: 106.2	565
$\text{Cs}_{0.90}\text{BA}_{0.10}\text{PbBr}_3$	Component 1: 101.0	381
	Component 2: 92.6	1428

The XRD measurements of initial $\text{CsPb}(\text{I}_{0.75}\text{Br}_{0.25})_3$ and $\text{CsPb}(\text{I}_{0.75}\text{Br}_{0.25})_3$ -0.5FAOAc films were also carried out (Figure 4.5a). Both spectra have two characteristic peaks of perovskite phase around $2\theta = 15^\circ$ and 29° . XRD peaks of the initial $\text{CsPb}(\text{I}_{0.75}\text{Br}_{0.25})_3$ -0.5FAOAc film shift to low angles compared to that of the $\text{CsPb}(\text{I}_{0.75}\text{Br}_{0.25})_3$ film, as the replacement of Cs^+ with larger FA^+ causes the perovskite lattice to expand. It suggests that FA^+ ions are doped into the $\text{CsPb}(\text{I}_{0.75}\text{Br}_{0.25})_3$ lattice, forming an OIHP intermediate phase $\text{Cs}_{1-x}\text{FA}_x\text{Pb}(\text{I}_{0.75}\text{Br}_{0.25})_3$.

The improved interfacial contact between the IPE perovskite and metal oxide can be understood by first-principles calculations (Figure 4.5b-c). The results show that, with the FA^+ introduction, the $\text{Cs}_{0.5}\text{FA}_{0.5}\text{Pb}(\text{I}_{0.75}\text{Br}_{0.25})_3/\text{TiO}_2$ interface has a higher binding energy than the $\text{CsPb}(\text{I}_{0.75}\text{Br}_{0.25})_3/\text{TiO}_2$ interface (1.31 vs 0.97 meV/Å²). This suggests that the OIHP intermediate phase has a stronger interaction with TiO_2 than the inorganic perovskite.¹⁵⁷

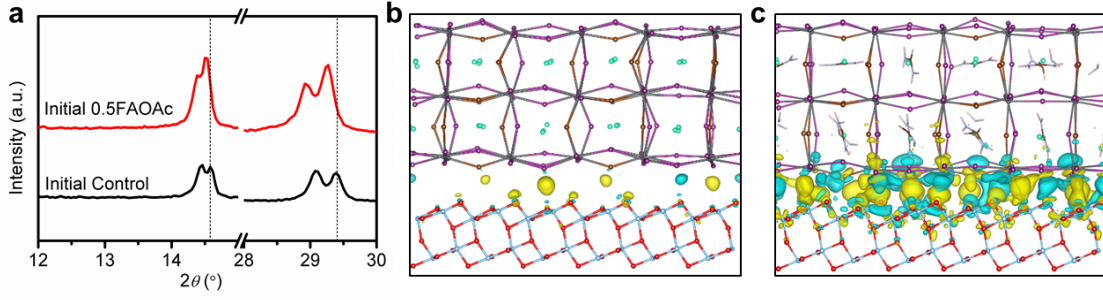
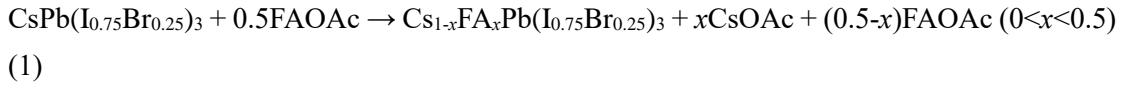


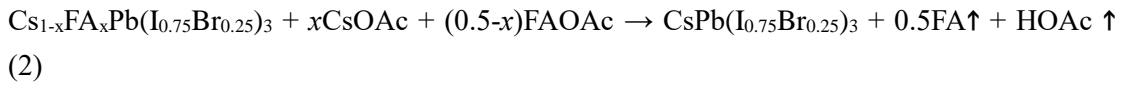
Figure 4.5. Characterizations of intermediate phase engineering (IPE) process. (a) X-ray diffraction spectra of the initial $\text{CsPb}(\text{I}_{0.75}\text{Br}_{0.25})_3$ and $\text{CsPb}(\text{I}_{0.75}\text{Br}_{0.25})_3$ -0.5FAOAc films. (b, c) The real-space distribution of difference charge density at the interfaces for $\text{CsPb}(\text{I}_{0.75}\text{Br}_{0.25})_3/\text{TiO}_2$ (c) and $\text{Cs}_{0.5}\text{FA}_{0.5}\text{Pb}(\text{I}_{0.75}\text{Br}_{0.25})_3/\text{TiO}_2$ (d). The corresponding binding energies are $-0.966 \text{ meV}/\text{\AA}^2$ and $-1.313 \text{ meV}/\text{\AA}^2$, respectively.

We carried out cross-sectional SEM of initial control and IPE films on meso- TiO_2 . Obvious voids are observed at the initial control perovskite/meso- TiO_2 interface. Meanwhile, the initial IPE film has good contact with meso- TiO_2 (Figure 4.6a). Thus, we infer that the good initial IPE perovskite/meso- TiO_2 interfacial contact results from the strong interfacial interaction.

The process of IPE promoting interface optimization can be schematically illustrated in Figure 4.6c. In the initial $\text{CsPb}(\text{I}_{0.75}\text{Br}_{0.25})_3$ -0.5FAOAc film, FA^+ ions are partially doped into the $\text{CsPb}(\text{I}_{0.75}\text{Br}_{0.25})_3$ lattice, which leads to the formation of an OIHP intermediate phase $\text{Cs}_{1-x}\text{FA}_x\text{Pb}(\text{I}_{0.75}\text{Br}_{0.25})_3$ ($0 < x < 0.5$) along with free CsOAc and FAOAc. The process is expressed as:



The stronger interaction between the OIHP intermediate phase and metal oxide charge selective layer leads to a high-quality perovskite/meso- TiO_2 interfacial contact. With the volatilization of FAOAc during thermal annealing, free Cs^+ replaces the doped FA^+ , and the OIHP intermediate phase transforms into the inorganic $\text{CsPb}(\text{I}_{0.75}\text{Br}_{0.25})_3$ phase. As the FAOAc is decomposed to formamidine (FA) gas and acetic acid (HOAc) gas under annealing,¹⁶⁷ this process can be expressed as:



During this process, the robust perovskite/metal oxide interfacial contact is preserved.

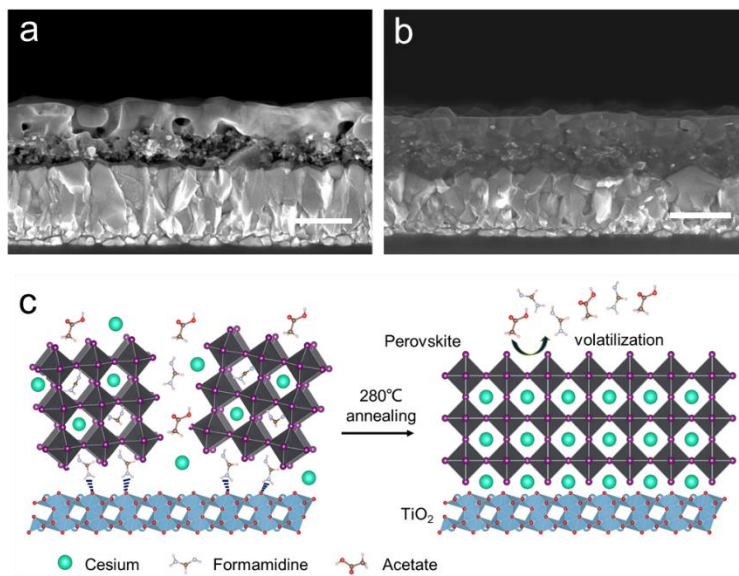


Figure 4.6. Characterizations of IPE process. Cross-sectional SEM images of initial control (a) and IPE (b) films. Scale bar = 500 nm. (c) Schematic illustration of the IPE process.

4.2.3 Volatile salts with different cations and anions

Besides FAOAc, volatile acetate salts with three different cations, methylammonium acetate (MAOAc), ammonium acetate (NH_4OAc) and butylammonium acetate (BAOAc) were further investigated as additives for $\text{CsPb}(\text{I}_{0.75}\text{Br}_{0.25})_3$. The annealed films of $\text{CsPb}(\text{I}_{0.75}\text{Br}_{0.25})_3$ -0.5MAOAc, $\text{CsPb}(\text{I}_{0.75}\text{Br}_{0.25})_3$ -0.5 NH_4OAc and $\text{CsPb}(\text{I}_{0.75}\text{Br}_{0.25})_3$ -0.5BAOAc are uniform and pinhole-free as shown in the top-view SEM images (Figure 7a-c). However, the cross-sectional SEM images of PSCs based on the three films show that only the $\text{CsPb}(\text{I}_{0.75}\text{Br}_{0.25})_3$ -0.5MAOAc perovskite completely penetrated into meso- TiO_2 , while voids at the perovskite/meso- TiO_2 interfaces of the others are reduced in comparison with those at control condition but are still not fully eliminated (Figure 4.7d-f). The $\text{CsPb}(\text{I}_{0.75}\text{Br}_{0.25})_3$ -0.5MAOAc device has an improved efficiency of 13.5%, and the $\text{CsPb}(\text{I}_{0.75}\text{Br}_{0.25})_3$ -0.5 NH_4OAc and $\text{CsPb}(\text{I}_{0.75}\text{Br}_{0.25})_3$ -0.5BAOAc devices show efficiencies of 11.6% and 11.1%, respectively (Figure 4.7h). We carried out ^{133}Cs solid-state NMR experiments on $\text{Cs}_{0.5}\text{MA}_{0.5}\text{PbBr}_3$, $\text{Cs}_{0.9}(\text{NH}_4)_{0.1}\text{PbBr}_3$, and $\text{Cs}_{0.9}\text{BA}_{0.1}\text{PbBr}_3$ to establish whether MA^+ , NH_4^+ and BA^+ can be doped into the CsPbBr_3 perovskite lattice (Figure 4.7i). Upon addition of MA^+ , the peak of CsPbBr_3 shifts to lower ppm values and broadens (the fitted values in Table 4.1), indicating the formation of a mixed Cs/MA 3D perovskite phase, analogous to the behaviour previously reported for Cs/FA 3D iodoplumbate¹¹⁴ and above for 3D bromoplumbate perovskites. Again, the presence of only one peak is evidence that the mixed Cs/MA material is phase pure. Therefore, MA^+ has the capacity to replace at least 50 mol% Cs^+ in the CsPbBr_3 perovskite lattice with no phase segregation. Doping with NH_4^+ and BA^+ leads to a different behaviour: the distribution of Cs^+ in $\text{Cs}_{0.9}(\text{NH}_4)_{0.1}\text{PbBr}_3$, and $\text{Cs}_{0.9}\text{BA}_{0.1}\text{PbBr}_3$ is

heterogeneous, indicative of phase segregation. The 3D perovskite peak of CsPbBr_3 in the two mixtures is largely unchanged compared to neat CsPbBr_3 , whilst a broad overlapping component appears in both cases indicating the formation of mixed $\text{Cs}^+/\text{NH}_4^+$ and Cs^+/BA^+ bromoplumbate phases. These secondary phases are likely 1D¹⁶⁸ and 2D¹⁶⁹, respectively, analogous to their undoped counterparts. The XRD peaks of the initial $\text{CsPb}(\text{I}_{0.75}\text{Br}_{0.25})_3$ -0.5MAOAc film are shifted left compared to those of the initial control film, which confirms the formation of an OIHP intermediate phase $\text{Cs}_{1-x}\text{MA}_x\text{Pb}(\text{I}_{0.75}\text{Br}_{0.25})_3$ as MA^+ dopes into the perovskite lattice (Figure 4.7j).^{114,120} The XRD peaks of the initial $\text{CsPb}(\text{I}_{0.75}\text{Br}_{0.25})_3$ -0.5 NH_4OAc and $\text{CsPb}(\text{I}_{0.75}\text{Br}_{0.25})_3$ -0.5BAOAc films locate in the same position with those of the initial control film. This corroborates the NMR result of no formation of a 3D OIHP intermediate phase. This result is expected, as the radii of NH_4^+ and BA^+ are not compatible with a cubic 3D perovskite lattice.

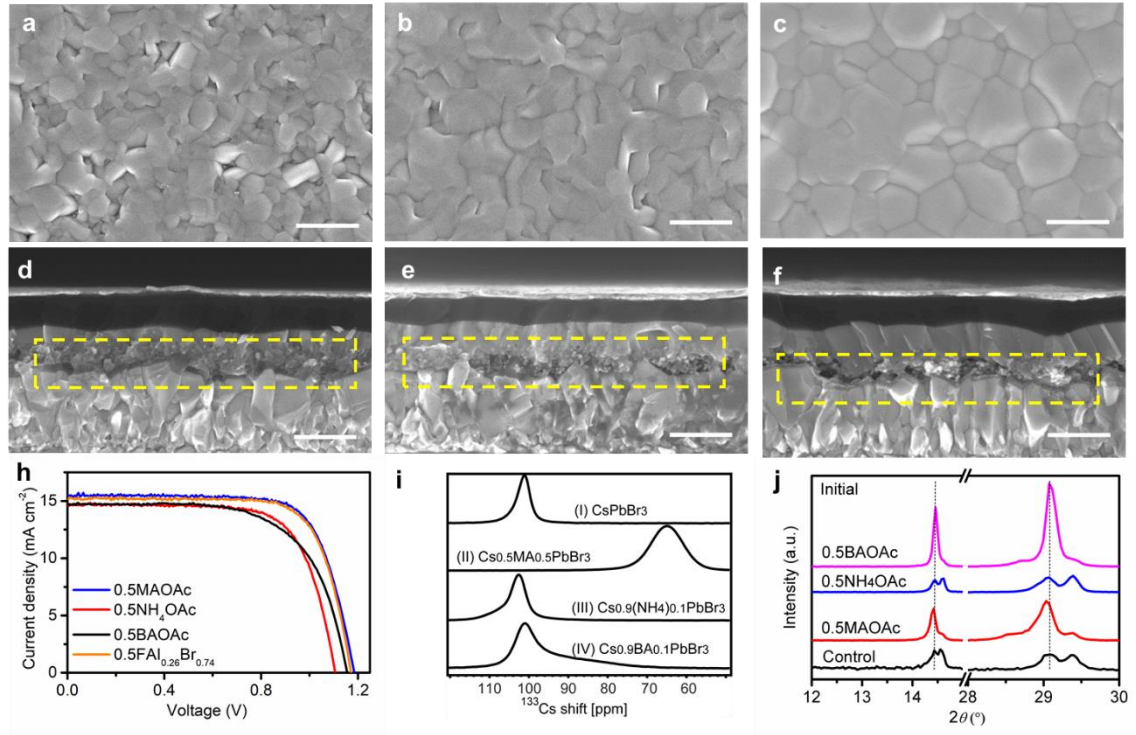


Figure 4.7. Volatile salts with different cations. (a-c) Top-view SEM images of the annealed $\text{CsPb}(\text{I}_{0.75}\text{Br}_{0.25})_3$ films with volatile salts of 0.5MAOAc, 0.5 NH_4OAc , and 0.5BAOAc, respectively. Scale bar = 1 μm . (d-f) Cross-sectional SEM images of the $\text{CsPb}(\text{I}_{0.75}\text{Br}_{0.25})_3$ -0.5MAOAc, $\text{CsPb}(\text{I}_{0.75}\text{Br}_{0.25})_3$ -0.5 NH_4OAc , and $\text{CsPb}(\text{I}_{0.75}\text{Br}_{0.25})_3$ -0.5BAOAc devices, respectively. Scale bar = 500 nm. The yellow dashed boxes show the perovskite/metal oxide interfaces. (g) $J-V$ curves of the $\text{CsPb}(\text{I}_{0.75}\text{Br}_{0.25})_3$ -0.5MAOAc, $\text{CsPb}(\text{I}_{0.75}\text{Br}_{0.25})_3$ -0.5 NH_4OAc , $\text{CsPb}(\text{I}_{0.75}\text{Br}_{0.25})_3$ -0.5BAOAc and $\text{CsPb}(\text{I}_{0.75}\text{Br}_{0.25})_3$ -0.5FAI_{0.26}Br_{0.74} devices, respectively. (h) Solid-state MAS NMR characterization of the materials. Echo-detected ^{133}Cs spectra at 21.1 T, 298 K and 20 kHz MAS of CsPbBr_3 , $\text{Cs}_{0.5}\text{MA}_{0.5}\text{PbBr}_3$, $\text{Cs}_{0.9}(\text{NH}_4)_{0.1}\text{PbBr}_3$, $\text{Cs}_{0.9}\text{BA}_{0.1}\text{PbBr}_3$. (i) XRD spectra of the initial perovskite films of $\text{CsPb}(\text{I}_{0.75}\text{Br}_{0.25})_3$, and with 0.5MAOAc, 0.5 NH_4OAc , and 0.5BAOAc on meso- TiO_2 .

Volatile formamidinium salts with different anions (FACl, FABr, and FAI) were also investigated. FACl was excluded for the generation of CsPbCl_3 or CsCl sediments in $\text{CsPb}(\text{I}_{0.75}\text{Br}_{0.25})_3$ -0.5FACl precursor solution.¹⁷⁰ Our very recent work shows that the MABr and MAI co-evaporated during thermal annealing, thus the ratio of MABr and MAI additives significantly influence the final composition of inorganic perovskite films.⁵⁶ To exclude the influence of band gap (E_g) changes of perovskite films on device performance, the E_g of the annealed $\text{CsPb}(\text{I}_{0.75}\text{Br}_{0.25})_3$ films with different ratios of FABr and FAI (denoted as $\text{CsPb}(\text{I}_{0.75}\text{Br}_{0.25})_3$ -0.5FAI $_x$ Br $_{1-x}$ ($0 \leq x \leq 1$)) were investigated. The E_g (derived from UV spectra) have a linear correlation with FAI content x (Figure 4.8a-b). It is fitted as:

$$E_g = 1.879 - 0.0727 x$$

When $x = 0.26$, the annealed $\text{CsPb}(\text{I}_{0.75}\text{Br}_{0.25})_3$ -0.5FAI $_{0.26}$ Br $_{0.74}$ film and the $\text{CsPb}(\text{I}_{0.75}\text{Br}_{0.25})_3$ film have the same E_g of 1.86 eV and their XRD spectra have the same characteristic peak positions at $2\theta = 14.62^\circ$ and 29.47° (Figure 4.8c-d), which show that these two films have the identical compositions. The SEM images show that the $\text{CsPb}(\text{I}_{0.75}\text{Br}_{0.25})_3$ -0.5FAI $_{0.26}$ Br $_{0.74}$ film is uniform and that it penetrates completely into meso- TiO_2 (Figure 4.8e-f). The PCE of the $\text{CsPb}(\text{I}_{0.75}\text{Br}_{0.25})_3$ -0.5FAI $_{0.26}$ Br $_{0.74}$ device improves to 13.1% (Figure 4.7h).

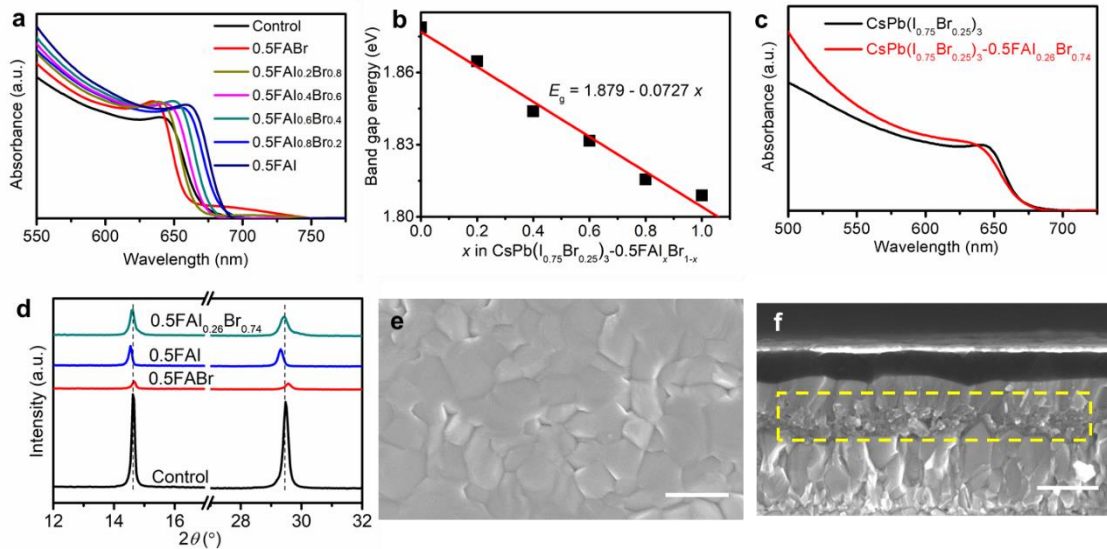


Figure 4.8. $\text{CsPb}(\text{I}_{0.75}\text{Br}_{0.25})_3$ -0.5FAI $_x$ Br $_{1-x}$. (a) Ultraviolet-visible (UV-Vis) spectra of the control and $\text{CsPb}(\text{I}_{0.75}\text{Br}_{0.25})_3$ -0.5FAI $_x$ Br $_{1-x}$ films with $x = 0, 0.2, 0.4, 0.6, 0.8, 1.0$. (b) The band gaps (E_g) of $\text{CsPb}(\text{I}_{0.75}\text{Br}_{0.25})_3$ -0.5FAI $_x$ Br $_{1-x}$ has a linear correlation with FAI content x . (c) UV-Vis spectra of the control and the $\text{CsPb}(\text{I}_{0.75}\text{Br}_{0.25})_3$ -0.5FAI $_{0.26}$ Br $_{0.74}$ films. (d) XRD spectra of annealed perovskite films of the control, and with volatile salts of 0.5FABr, 0.5FAI, and 0.5FAI $_{0.26}$ Br $_{0.74}$ on meso- TiO_2 . (e) Top-view SEM images of the annealed $\text{CsPb}(\text{I}_{0.75}\text{Br}_{0.25})_3$ -0.5FAI $_{0.26}$ Br $_{0.74}$ film. Scale bar = 1 μm . (f) Cross-sectional SEM images of the $\text{CsPb}(\text{I}_{0.75}\text{Br}_{0.25})_3$ -0.5FAI $_{0.26}$ Br $_{0.74}$ devices. Scale bar = 500 nm.

According to the research of different anions and cations above, we think that the NH_4^+ , BA^+

and OAc^- cannot be doped into perovskite lattice but can act as surface ligands and form an interlayer which links the electron transport layer (ETL) and initial perovskite layer. Thus, the $\text{CsPb}(\text{I}_{0.75}\text{Br}_{0.25})_3\text{-0.5NH}_4\text{OAc}$ and $\text{CsPb}(\text{I}_{0.75}\text{Br}_{0.25})_3\text{-0.5BAOAc}$ devices have shown mild improvement of PCE due to the improvement of their interfaces in comparison with control devices. However, the intermediate perovskite phase with MA^+ or FA^+ can directly bond the ETL by strong hydrogen bonding. The better interfacial contact and higher PCE for devices with FAOAc and MAOAc additives than those of NH_4OAc and BAOAc indicate that the IPE method has better performance in interface optimization than the method with forming an interlayer.

4.2.4 PSCs on planar structure

In comparison with the meso-device, the planar PSCs demand higher quality perovskite films to achieve high PCEs.¹⁷¹ Here, the planar devices with a configuration of FTO/compact tin oxide (c-SnO_2)/ $\text{CsPb}(\text{I}_{0.75}\text{Br}_{0.25})_3$ /spiro-OMeTAD/Au are fabricated. For the control device, visible voids exist at perovskite/ c-SnO_2 interface, and the PCE is only 11.3% (Figure 4.9a-c). While for IPE devices based on $\text{CsPb}(\text{I}_{0.75}\text{Br}_{0.25})_3\text{-0.5FAOAc}$, the perovskite film has an excellent contact with c-SnO_2 as shown in the cross-sectional SEM image (Figure 4.9d-e). The champion IPE device based on $\text{CsPb}(\text{I}_{0.75}\text{Br}_{0.25})_3\text{-0.5FAOAc}$ film has a PCE of 17.0% with an SPO of 16.2% (Figure 4.9f). As shown in Figure 4.1a, the ratio of the champion PCE and its corresponding S-Q efficiency limit is 66%, which is higher than that of high performance inorganic PSCs without organic residues or modification in perovskite layers from previous literature ($\leq 60\%$) and comparable to that of organic-inorganic PSCs ($\leq 65\%$) in the band gap range between 1.72 eV to 2.3 eV.^{14107,155} The V_{oc} increases from 1.14 V for the control device to 1.34 V for the champion device.

This spectacular improvement in V_{oc} was further elucidated using electroluminescence (EL) by studying the champion devices. The external EL quantum efficiency for an IPE device was increased by three orders of magnitude compared to a control device (Figure 4.9g). It reaches 2×10^{-4} for currents similar to J_{sc} , which corresponds to a voltage loss of 220 mV.¹²⁷ Considering the theoretical maximum V_{oc} of 1.56 V for a solar cell based on $\text{CsPb}(\text{I}_{0.75}\text{Br}_{0.25})_3$ with a band gap of 1.86 eV, we calculate a V_{oc} of 1.34 V, which is consistent with the experimental data. The V_{oc} is up to 86% of the theoretical maximum V_{oc} which is the highest ratio reported in inorganic PSCs so far (Figure 4.1b).

To get more insights into this strong enhancement of the EL for IPE devices based on $\text{CsPb}(\text{I}_{0.75}\text{Br}_{0.25})_3\text{-0.5FAOAc}$, we compared the photoluminescence efficiency of control and IPE films on glass substrates, on c-SnO_2 substrates, on glass substrates with a spiro-OMeTAD top layer, and in devices, respectively (Figure 4.9h). The PL intensities for films on glass

substrates are comparable, indicating that the IPE films do not show a reduced density of defects in comparison with the control film consistent with the TRPL results above. The PL intensities are slightly quenched for films on c-SnO₂ in both cases. On the contrary, the PL of films on glass substrates with a spiro-OMeTAD top layer is heavily quenched (by more than 2 orders of magnitude). This indicates that the perovskite/spiro-OMeTAD interface is a major source of surface recombination limiting the V_{oc} . Note that majority charge injection into the HTL is not sufficient to lead to a quenched PL if it is not accompanied by an enhanced interfacial recombination. We then measured the PL of the complete devices and found the PL peak is around 10 times higher for IPE devices than the control device, which agrees with the trend in EL. It is an unexpected finding that the PL of IPE device is not quenched compared to IPE films on glass, despite the presence of spiro-OMeTAD. We hypothesize that a possible reason is suppressed recombination at the HTM interface due to a favorable built-in electric field in the perovskite, which could result from the good (i.e. more conductive) ETL/perovskite interfacial contact, also consistent with the trend in FF (79.9% vs. 68.6%).¹⁷² In conclusion, these results obtained from an IPE device indicate an enhanced charge selectivity of the interface, accompanied by a high built-in potential and/or very good injection and transport of electrons and holes.¹⁷²

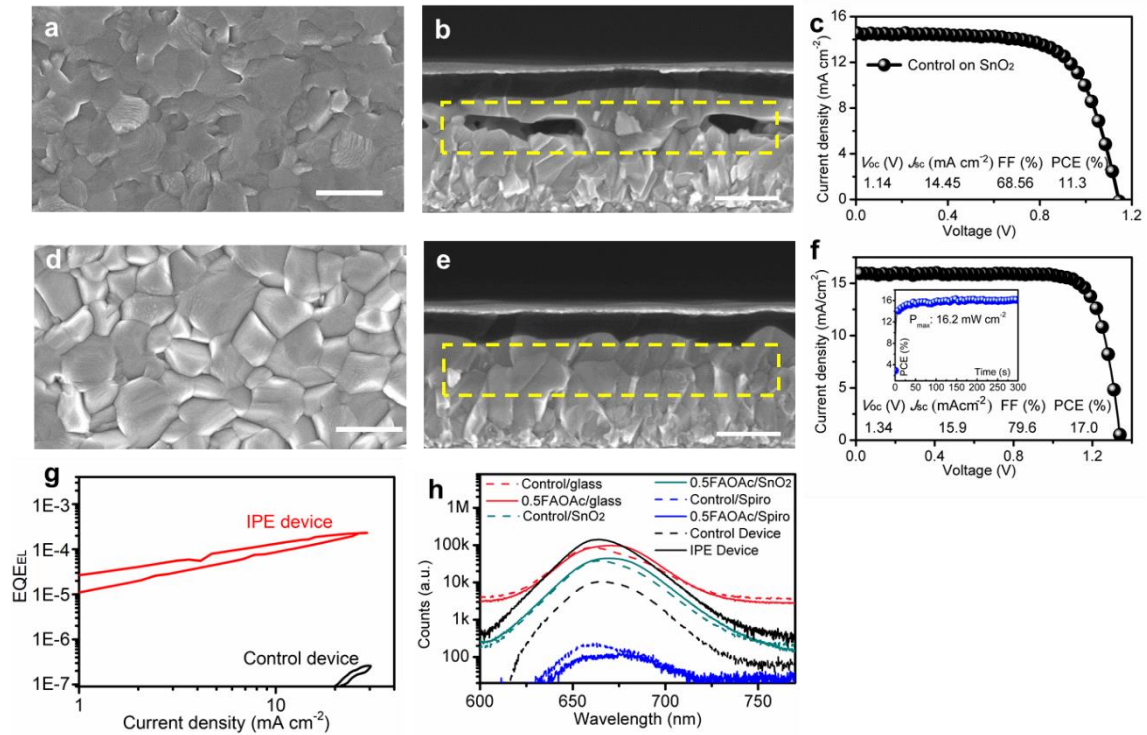


Figure 4.9. PSCs of planar SnO₂ structure. (a, d) Top-view SEM images of the control and the CsPb(I_{0.75}Br_{0.25})₃-0.5FAOAc perovskite films on compact tin oxide, respectively. Scale bar = 1 μm. (b, e) Cross-sectional SEM images of the control and the IPE CsPb(I_{0.75}Br_{0.25})₃-0.5FAOAc films in planar structure, respectively. Scale bar = 500 nm.

The yellow dashed boxes show the perovskite/metal oxide interfaces. (c,f) $J-V$ curve of the control and champion IPE devices in planar structure, respectively. The inset in (f) shows the SPO of the IPE device for 240 s. (g) Electroluminescence quantum efficiency as a function of injection current. (h) Photoluminescence spectra of control and IPE films on glass substrates, on compact SnO_2 substrates, on glass substrates with a spiro-OMeTAD top layer, and in devices, respectively.

Long-term stability of the perovskite materials and devices was examined. The $\text{CsPb}(\text{I}_{0.75}\text{Br}_{0.25})_3$ and $\text{CsPb}(\text{I}_{0.75}\text{Br}_{0.25})_3\text{-0.5FAOAc}$ films were exposed in ambient air at room temperature with a relative humidity around 40%. Figure 4.10a shows photographs of the two films monitored over the course of 60 min. The film of $\text{CsPb}(\text{I}_{0.75}\text{Br}_{0.25})_3\text{-0.5FAOAc}$ shows better stability than the $\text{CsPb}(\text{I}_{0.75}\text{Br}_{0.25})_3$ film, which may be due to the stronger strain of $\text{CsPb}(\text{I}_{0.75}\text{Br}_{0.25})_3$ film with c- SnO_2 resulting from the better interfacial contact.²¹ The EL of perovskite light-emitting diodes and solar cells commonly decreases with time. As shown in Figure 4.10b, under a driving current density of 16 mA/cm^2 , the external EL quantum efficiency of the IPE device at the 10^{-3} order of magnitude maintained 90% of its maximum value after 500 s. However, the control device at the same driving current density maintains only 43% of its maximum external EL quantum efficiency after 500 s, even though its EL quantum efficiency is 3 orders of magnitude lower than that of the IPE device. This indicates that the IPE device is more stable against enhanced defect recombination during operational conditions. To further evaluate the device stability, the maximum power point of an unencapsulated $\text{CsPb}(\text{I}_{0.75}\text{Br}_{0.25})_3\text{-0.5FAOAc}$ inorganic PSC was tracked under a white light-emitting diode irradiation with an intensity equivalent to 1 sun in N_2 atmosphere. After 500 h of continuous light soaking, the device maintained 87% of its initial efficiency (Figure 4.10c).

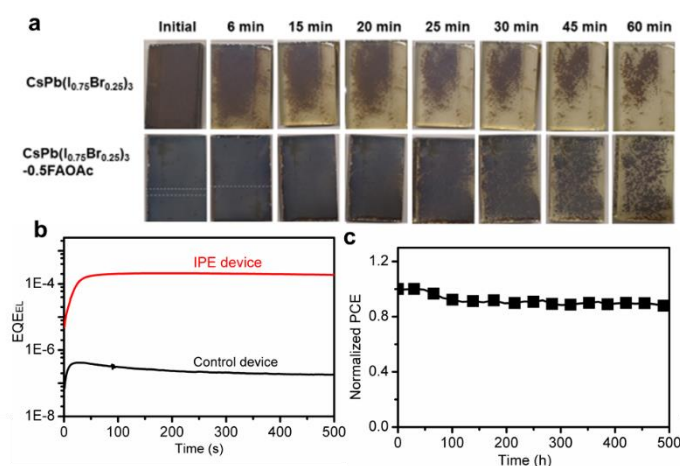


Figure 4.10. Stability. (a) The evolution of photographs over time of the annealed $\text{CsPb}(\text{I}_{0.75}\text{Br}_{0.25})_3$ and $\text{CsPb}(\text{I}_{0.75}\text{Br}_{0.25})_3\text{-0.5FAOAc}$ films in ambient condition. The relative humidity is around 40%, and the room temperature is $298 \pm 5 \text{ K}$. (b) Electroluminescence stability tests of control and IPE PSCs in planar structure. (c) Evolution of the power conversion efficiency (PCE) over time of an unencapsulated $\text{CsPb}(\text{I}_{0.75}\text{Br}_{0.25})_3\text{-0.5FAOAc}$

based perovskite solar cell under 100 mW cm⁻² continuous irradiation.

4.3 Summary

In conclusion, we have developed an intermediate phase engineering strategy to enhance the interfacial contact between the all-inorganic perovskite and metal oxide by introducing organic volatile salts into the inorganic perovskite precursor solution. According to our investigation of volatile salts with different cations and anions, we found that the introduction of organic cations (such as MA⁺ and FA⁺), which can be doped into the cubic perovskite lattice lead to the formation of an OIHP intermediate phase in the initial film. The strong interaction between OIHP intermediate phase and metal oxide promotes the high-quality interfacial contact. With this strategy, the champion planar-device achieves a PCE of 17.0% with a V_{oc} of 1.34 V. The PCE and V_{oc} are 66% and 86% of their Shockley-Queisser limits. Moreover, the matching band gap (1.86 eV), high V_{oc} and high PCE make the inorganic PSCs potential candidates for top devices in Si/perovskite, CuInGa(S,Se)/perovskite or perovskite/perovskite tandem devices.

4.4 Experimental section

4.4.1 Preparation method

Preparation of perovskite solutions The precursor chemicals were mixed stoichiometrically with anhydrous dimethyl sulfoxide (DMSO, ACROS, 99%) solvent and heated at 80 °C until completely dissolved. All precursor perovskite solutions are 1 M. Recipes are as follow:

1 M CsPb(I_{0.75}Br_{0.25})₃ = 1 mol CsI + 0.625 mol PbI₂ + 0.375 mol PbBr₂ + 1 ml DMSO

1 M CsPb(I_{0.75}Br_{0.25})₃-0.5FAOAc = 1 mol CsI + 0.625 mol PbI₂ + 0.375 mol PbBr₂ + 0.5 mol FAOAc + 1 ml DMSO

1 M CsPb(I_{0.75}Br_{0.25})₃-0.25FAOAc = 1 mol CsI + 0.625 mol PbI₂ + 0.375 mol PbBr₂ + 0.25 mol FAOAc + 1 ml DMSO

1 M CsPb(I_{0.75}Br_{0.25})₃-0.75FAOAc = 1 mol CsI + 0.625 mol PbI₂ + 0.375 mol PbBr₂ + 0.75 mol FAOAc + 1 ml DMSO

1 M CsPb(I_{0.75}Br_{0.25})₃-1.0FAOAc = 1 mol CsI + 0.625 mol PbI₂ + 0.375 mol PbBr₂ + 1.0 mol FAOAc + 1 ml DMSO

1 M CsPb(I_{0.75}Br_{0.25})₃-0.5NH₄OAc = 1 mol CsI + 0.625 mol PbI₂ + 0.125 mol PbBr₂ + 0.25 mol Pb(OAc)₂ + 0.5 mol NH₄Br + 1 ml DMSO

1 M CsPb(I_{0.75}Br_{0.25})₃-0.5MAOAc = 1 mol CsI + 0.375 mol PbI₂ + 0.375 mol PbBr₂ + 0.25 mol

$\text{Pb}(\text{OAc})_2 + 0.5 \text{ mol MAI} + 1 \text{ ml DMSO}$

$1 \text{ M CsPb}(\text{I}_{0.75}\text{Br}_{0.25})_3\text{-}0.5\text{BAOAc} = 1 \text{ mol CsI} + 0.375 \text{ mol PbI}_2 + 0.375 \text{ mol PbBr}_2 + 0.25 \text{ mol Pb}(\text{OAc})_2 + 0.5 \text{ mol BAI} + 1 \text{ ml DMSO}$

$1 \text{ M CsPb}(\text{I}_{0.75}\text{Br}_{0.25})_3\text{-}0.5\text{FAI}_x\text{Br}_{1-x} = 1 \text{ mol CsI} + 0.625 \text{ mol PbI}_2 + 0.375 \text{ mol PbBr}_2 + 0.5x \text{ mol FAI} + 0.5(1-x)\text{FABr} + 1 \text{ ml DMSO} (0 \leq x \leq 1)$

Formamidinium acetate (FAOAc, Sigma, 99%), Lead iodide (PbI_2 , AlfaAesar, 99.999%), Lead bromide (PbBr_2 , TCI, 99%), Cesium iodide (CsI, ABCR, 99.998%), Methylammonium iodide (MAI, Dyesol), Formamidinium iodide (FAI, Dyesol), Butylammonium iodide (BAI, TCI, >99.7%), Ammonium bromide (NH_4Br , Sigma, 99.999%), Formamidinium bromide (FABr, Dyesol).

Lead acetate ($\text{Pb}(\text{OAc})_2$): pure $\text{Pb}(\text{OAc})_2$ was obtained by removing the crystal water of the Lead (II) acetate trihydrate (Sigma, 99.99%) by heating at 60 °C for 30 min and 80 °C for 2 h.

Device fabrication

Mesoscopic device architecture: FTO/compact- TiO_2 (c- TiO_2)/meso- TiO_2 /perovskite/spiro-OMeTAD/Au.

1. FTO glass sheet (Nippon Cor. Japan, 10 Ω/sq): A 3.5 mm ribbon area was etched away with zinc powder and 4 M HCl solution. Then the glass sheets were cleaned with 2% volume ratio Hellmanex solution, deionized water, acetone, and ethanol by sonication for 15 min in turns. Finally, the glass sheets were dried with air gas and treated with ultraviolet ozone for 15 min.
2. c- TiO_2 : A 40 nm thick TiO_2 compact layer was deposited on top of FTO glasses by spray pyrolysis at 450 °C from a precursor solution containing 0.6 ml titanium diisopropoxide bis(acetylacetonate) (Sigma-Aldrich, 75 wt%) and 0.4 ml acetylacetone (Sigma-Aldrich, >99%) in 9 ml anhydrous ethanol.
3. meso- TiO_2 : A 150 nm thick meso- TiO_2 layer was deposited by spin-coating a diluted TiO_2 paste (Dyesol, 30NR-D) with anhydrous ethanol (w:w = 1:6) at 4000 rpm for 20 s. Sheets were dried at 80 °C for 10 min and sintered at 450 °C for 30 min.
4. Perovskite layer: The perovskite films were prepared by spin-coating the precursor solutions in a two-step program at 1000 rpm and 3000 rpm for 10 s and 50 s, respectively. The films were placed in glovebox for 60 min, then annealed at 280 °C for 10 min in a dry-air glovebox.
5. Hole transport layer: The spiro-OMeTAD (Merck) chlorobenzene solution (90 mg ml^{-1}) with 20.6 μl bis (trifluoromethane)sulfonimide lithium salt (Li-TFSI, Sigma-Aldrich, 520 mg ml^{-1} in acetonitrile) and 35.5 μl 4-*tert*-butylpyridine (*t*-BP, Sigma-Aldrich) was spin-coated on top of the perovskite film at 4000 rpm for 20 s. The devices were put into a dry-air glovebox (RH < 8%) for 12 h.

6. Electrode deposition: An 80 nm-thick gold electrode was deposited by thermal evaporation. Planar device architecture: FTO/c-SnO₂/perovskite/spiro-OMeTAD/Au. In the planar structure device, the c-SnO₂ was grown on FTO by chemical bath deposition (CBD) method as previous reported.¹ In details, the CBD precursor solution was prepared by mixing 0.5 g urea, 10 μ l mercaptoacetic acid, 0.5 ml HCl (37 wt%), and 109.7 mg SnCl₂·2H₂O (0.012 M) in 240 ml deionized water and stirred for 2 min. FTO substrates were vertically put in a glass container filled with the above solution, then heated in an oven for three hours at 70 °C. The treated substrates were rinsed in deionized water and sonicated for 2 min to remove residual material, then dried with dry air and annealed at 180 °C for 60 min.

Other layers were prepared in the same way as described for the meso-device.

4.4.2 Characterization

SEM characterization A high-resolution SEM (Zeiss Merlin) with an in-lens detector was used for characterizing the top-view and cross-sectional morphologies of devices.

XRD measurements XRD patterns were acquired with a PANalytical Empyrean diffractometer in the transmission-reflection mode, using the Cu K α radiation and the Ni β -filter.

Optical characterization UV-Vis spectra were measured by Varian Cary 5. Band gaps (E_g) were derived from UV-Vis spectra with the Tauc-plot method. Photoluminescence spectra were measured by Fluorolog 322 (Horiba Jobin Yvon Ltd). Samples were excited at 450 nm by a standard 450 W xenon CW lamp. Time-resolved photoluminescence measurements were carried out by using a time-correlated single-photon counting (TCSPC) spectrometer (Fluorolog[®]-3, HORIBA Scientific). A diode laser (402 nm) was used as the excitation source, and a photomultiplier was used as the detector (Horiba TBX Picosecond Photon Detector).

Electrochemical impedance spectroscopy (EIS) EIS analysis was conducted with an electrochemical test station (ParSTAT MC, Princeton Applied Research, USA). The frequency range is from 0.1 Hz to 100 kHz at 0.8-1.0 V bias in dark. The sinusoidal AC perturbation is 25 mV.

Photovoltaic performance The PSCs were tested with a 450 W xenon light source (Oriel) in air at room temperature. The spectral mismatch between AM 1.5G and the solar simulator was calibrated by a Schott K113 Tempax filter. The light intensity was calibrated by a silicon photodiode for each measurement. The J-V curves were recorded by applying an external voltage bias with Keithley 2400 to give the corresponding current response with a scan rate of 10 mV/s (the voltage step is 5 mV with no delay time). Cells were covered by a black metal mask with an active area of 0.16 cm². Incident photon-to-current conversion efficiency (IPCE) measurements were carried out from the monochromatic visible photons, from Gemini-180

double monochromator Jobin Yvon Ltd., powered by a 300 W xenon light source (ILC Technology, USA) superimposed on a 1 mW cm⁻² LED light. The monochromatic incident light passed through a chopper running at 8 Hz frequency and the on/off ratio was measured by an operational amplifier.

Solid-state NMR measurements Room temperature ¹³³Cs (118.04 MHz and 65.58 MHz) NMR spectra were recorded on a Bruker Avance Neo 21.1 T spectrometer and Bruker Avance III 11.7 T spectrometer equipped with a 3.2 mm low-temperature CPMAS probe. ¹³³Cs shifts were referenced to 1 M aqueous solution of CsCl, using solid CsI ($\delta = 271.05$ ppm) as a secondary reference. ¹H chemical shifts were referenced to solid adamantane ($\delta_H = 1.91$ ppm). Quantitative echo-detected ¹³³Cs spectra were recorded with recycle delay between 24 s to 100 s. ¹H spectra were acquired with recycle delays between 3 s to 10 s. Peak widths were fitted in Topspin 3.2.

Perovskite mechanosynthesis Starting materials were stored inside a glove box under argon. Perovskite powders were synthesized by grinding the reactants in an electric ball mill (Retsch Ball Mill MM-200) using a grinding jar (10 ml) and a ball ($\varnothing 10$ mm) for 60 min at 25 Hz. The resulting powders were annealed for 20 min at temperature specified. The amounts of reagents taken into the synthesis were listed in Table 4.2.

Table 4.2. The amounts of reagents taken into the synthesis for mechanosynthesis for NMR measurements.

Materials	Reagents and amounts	Annealing temperature (°C)
CsPbBr ₃	CsBr: 0.212 g (1.00 mmol) PbBr ₂ : 0.367 g (1.00 mmol)	250
Cs _{0.95} FA _{0.05} PbBr ₃	CsBr: 0.202 g (0.95 mmol) FABr: 0.006 g (0.05 mmol) PbBr ₂ : 0.367 g (1.00 mmol)	150
Cs _{0.90} FA _{0.10} PbBr ₃	CsBr: 0.191 g (0.90 mmol) FABr: 0.012 g (0.10 mmol) PbBr ₂ : 0.367 g (1.00 mmol)	150
Cs _{0.85} FA _{0.15} PbBr ₃	CsBr: 0.180 g (0.85 mmol) FABr: 0.018 g (0.15 mmol) PbBr ₂ : 0.367 g (1.00 mmol)	150
Cs _{0.80} FA _{0.20} PbBr ₃	CsBr: 0.170 g (0.80 mmol) FABr: 0.024 g (0.20 mmol) PbBr ₂ : 0.367 g (1.00 mmol)	150
Cs _{0.75} FA _{0.25} PbBr ₃	CsBr: 0.159 g (0.75 mmol) FABr: 0.031 g (0.25 mmol) PbBr ₂ : 0.367 g (1.00 mmol)	150
Cs _{0.50} FA _{0.50} PbBr ₃	CsBr: 0.106 g (0.75 mmol) FABr: 0.062 g (0.25 mmol) PbBr ₂ : 0.367 g (1.00 mmol)	150
CsPbBr ₃ -0.2Pb(OAc) ₂	CsBr: 0.212 g (1.00 mmol) PbBr ₂ : 0.367 g (1.00 mmol) Pb(OAc) ₂ : 0.065 g (0.20 mmol)	150
CsPbBr ₃ -0.5Pb(OAc) ₂	CsBr: 0.212 g (1.00 mmol) PbBr ₂ : 0.367 g (1.00 mmol) Pb(OAc) ₂ : 0.162 g (0.50 mmol)	150
CsPbBr ₃ -0.5FAOAc	CsBr: 0.212 g (1.00 mmol) PbBr ₂ : 0.367 g (1.00 mmol) FAOAc: 0.052 g (0.50 mmol)	80°C (for the initial powder) 280°C (for the annealed powder)
Cs _{0.80} FA _{0.20} OAc	CsOAc: 0.154 g (0.8 mmol) FAOAc: 0.0208 g (0.2 mmol)	Without annealing
Cs _{0.50} MA _{0.50} PbBr ₃	CsBr: 0.106 g (0.50 mmol) PbBr ₂ : 0.367 g (1.00 mmol) MABr: 0.056 g (0.50 mmol)	150
Cs _{0.90} (NH ₄) _{0.10} PbBr ₃	CsBr: 0.191 g (0.90 mmol) PbBr ₂ : 0.367 g (1.00 mmol) (NH ₄)Br: 0.0098 g (0.10 mmol)	150
Cs _{0.90} BA _{0.10} PbBr ₃	CsBr: 0.191 g (0.90 mmol) PbBr ₂ : 0.367 g (1.00 mmol) BABr: 0.015 g (0.10 mmol)	150

Perovskite powder from solution processing The initial and annealed perovskite films were

prepared by spin-coating the precursor solutions at 1000 rpm for 50 s, and respectively annealed at 80 °C for 30 s to remove the excess DMSO and at 280 °C for 8 min. Then these films were scratched off for solid-state NMR measurements.

Vaporized components from CsPbBr₃-0.5FAOAc powder During annealing the initial CsPbBr₃-0.5FAOAc powder at 280 °C, a glass slide was put on the crucible of the powder to collect the vaporized components. Then the vaporized components were dissolved in the DMSO-d₆ for liquid-state ¹H NMR characterization.

Electroluminescence spectra (EL) The driving voltage was applied using a Bio-Logic SP300 potentiostat, it was also used to measure the short-circuit current of a Hamamatsu Silicon photodiode (1 cm²) placed in close vicinity of the sample to detect the emitted photon flux. An estimation of the external quantum yield of EL is obtained by dividing this current corrected for the spectral response of the photodiode by the driving current of the tested PSC.

Stability measurements A continuous flow of dry nitrogen gas was flushed into the custom-built airtight weathering chamber as the sample holder. The chamber was placed under a full AM 1.5 Sun-equivalent white light-emitting diode lamp (LXM3-PW51 with a spectrum of 400-750 nm). The spectral mismatch between AM 1.5G and the solar simulator was calibrated by a Schott K113 Tempax filter. The equivalent sun intensities were calibrated using a calibrated silicon reference diode equipped with a KG-3 filter. The devices were measured *in situ* with a maximum power point (MPP) tracking routine using a Biologic MPG2 potentiostat under continuous illumination at 25 °C with an aperture of 0.16 cm². The MPP was updated every 10 s by a standard perturb-and-observe method. A Peltier element in direct contact with the films was used to control the temperature of the devices. A Pt100 thermometer inserted between the Peltier element and the film was used to measure the temperature of the devices. Every 30 minutes a *J-V* curve was recorded in order to track the evolution of individual *J-V* parameters. The setup is centrally-controlled through a LabView interface allowing for the automatic programming of experiments.

Density function theory calculation All the theoretical calculations were performed with the Vienna Ab-initio Simulation Package. The projector-augmented wave method for the core region and the generalized gradient approximation with the Perdew, Burke and Ernzerhof functional were employed. A kinetic energy cutoff of 400 eV was adopted in the plane-wave expansion. All structures are fully relaxed until the force on each atom is less than 0.01 eV/Å. The Brillouin zone integration was sampled by gamma-only points in order to reduce the computational cost in the huge model of interface. An adequate vacuum space of 15 Å was set between periodic slabs. The perovskite/TiO₂ interface was modelled by using the (110)-perovskite/(101)-TiO₂ surface. This contact is extensively adopted by previous studies^{157,173} which would introduce the smallest lattice mismatch. A 3 × 5 × 2 perovskite slab consisting of

30 perovskite units were placed onto a $5 \times 3 \times 2$ TiO_2 slab made by 120 TiO_2 units. The lattice parameters of the model were fixed at the values of TiO_2 substrate and the positions of the topmost TiO_2 layer plus the entire perovskite slabs were fully relaxed.

Chapter 5 Intermediate phase promoting CsPbI₃ γ -phase formation for efficient photovoltaics

This chapter was the following ongoing work with the permission of all co-authors.

Zaiwei Wang[#], Jiahuan Zhang[#], Jun Li[#], Michael Graetzel*, Wanlin Guo*, Anders Hagfeldt*, Intermediate phase promoting pure CsPbI₃ γ -phase formation for efficient photovoltaic. (In preparation)

[#]These authors contributed equally to this work.

My contribution: Z. W. and J. Z. conceived the idea of this project, designed the experiments and wrote the manuscript. J. Z., and Z.W. performed the fabrication, optimization and characterization of films and devices. Z. W. and J. Z. performed SEM imaging, and XRD measurements.

All-inorganic halide perovskites have attracted immense interest in long-term stable photovoltaic materials and tandem solar cells. CsPbI₃ is the most typical and popular material in highly efficient inorganic PSCs, however the formation of high-quality CsPbI₃ films with pure black phase is still a challenge. In this chapter, an intermediate phase engineering strategy is reported to promote the pure black phase CsPbI₃ perovskite film formation. According to the investigation of the phase transformation processes of pure CsPbI₃ and that with different additives, including NH₄I, BAI, MAI, FAI and DMAI, we found that the formation of a 3D organic-inorganic hybrid perovskite intermediate phase is essential to avoid the generation of the undesired yellow phase and promote the formation of a pure black-phase CsPbI₃ film. A champion efficiency of 17.70% with a stabilized power output of 17.58% based on the optimized CsPbI₃-DMAI device is achieved.

5.1 Introduction

In recent ten years, halide perovskites are sparking a revolution in the field of optoelectronics such as solar cells, light-emitting diodes (LEDs), and photo-/radiation-detectors, scintillators.^{1,3,4,6,7,73,109,110,174,175} This results from their outstanding optoelectronic properties including long charge carrier diffusion lengths, large light-absorption coefficients, intrinsic tolerance to defects, and tunable band gaps.^{5,17,25,151} Especially, the certified power conversion efficiency (PCE) of organic-inorganic hybrid perovskite solar cells (PSCs) has reached 25.2% in 2020, which is higher than that of the most widely-used polycrystalline silicon solar cell.¹⁰

Despite the encouraging PCE, the intrinsic instability of organic-inorganic hybrid perovskite (OIHP) materials, such as the degradation under moisture and heat, is hindering further industrialization of PSCs.^{145,170} By replacing the volatile organic cations with an inorganic cesium cation (Cs⁺), the all-inorganic cesium lead halide perovskites, denoted as CsPbX₃ (X = Br, I), are attracting extensive research as intrinsically stable candidates for highly efficient PSCs.^{15,21,99}

CsPbI₃ exhibits a bandgap of 1.73 eV, which is closer to the optimum value (1.35 eV) of a single-junction solar cells in lead-based halide inorganic perovskites.¹⁷ The CsPbI₃ has three photosensitive “black phases” (cubic α -phase, tetragonal β -phase, and orthorhombic γ -phase).¹⁸ However, they can easily transform into a more thermodynamically stable yellow non-perovskite (δ -phase) at ambient condition.²⁰ Obtaining a high-quality pure black inorganic perovskite phase is the primary consideration for the fabrication of high-efficiency inorganic PSCs.^{15,16}

Intermediate phase engineering is being widely used to promote the formation of black phase of FAPbI₃ and CsPbI₃ for high-efficiency PSCs.^{15,51,176,177} But the mechanism of which kind of additives or the intermediate phases are effective for the formation of black phases is ambiguous.

Here, we investigated the procedures of phase transitions of CsPbI₃ with different additives (such as FAI, MAI, DMAI, NH₄I and BAI) in CsPbI₃ precursor solutions, finding that the 3D OIHP intermediate phase is essential for avoiding the generation of yellow phase and promoting the formation of pure CsPbI₃ black-phase. By the further modulation of morphology of CsPbI₃ film based on intermediate phase, we achieved the PCE of 17.7% based on CsPbI₃ device, which is among the highest in inorganic PSCs without organic residues or modification in perovskite layers.

5.2 Results and discussion

5.2.1 Phase transformation of intermediate phase engineering

Pure CsPbI₃ phase transformation has been fully investigated. When it is directly annealed at high temperature (>300 °C), the transformation is incomplete and the annealed film composes of both yellow and black phase.⁵⁴ Here we investigated the effects of volatile iodide salts for the phase transformation, including NH₄I, BAI, MAI, FAI, and DMAI. The NH₄⁺ and BA⁺ could not enter the monocation position for 3D inorganic perovskite.¹⁷⁷ They have been reported to exist as one-dimensional (1D) NH₄PbI₃ and two-dimensional (2D) BA₂PbI₄.^{178,179} Both the MA⁺ and FA⁺ can be mixed with Cs⁺ to form the mixed cation Cs_xMA_{1-x}PbI₃ or Cs_xFA_{1-x}PbI₃ perovskites in any proportion.^{122,177} While for DMA_{1-x}Cs_xPbI₃, the low x trend to form the 1D phase and the high x is easy to form the 3D perovskite phase.⁵⁰⁻⁵³

The perovskite films of pure CsPbI₃ and with additives (NH₄I, BAI, MAI, FAI, and DMAI, 1:1 mole ratio in the precursor solution) were obtained by one-step spin-coating method and with a gradient annealing at 80 °C for 2 min and 330 °C for 5 min. These samples are denoted as control, CsPbI₃-NH₄I, CsPbI₃-BAI, CsPbI₃-MAI, CsPbI₃-FAI, CsPbI₃-DMAI films, respectively. As the digital photos show in Figure 5.1, the annealed control, CsPbI₃-NH₄I, CsPbI₃-BAI exhibit a yellow color, while CsPbI₃-MAI, CsPbI₃-FAI, CsPbI₃-DMAI films turned black. According to X-ray diffraction (XRD) spectra and UV-Vis spectra, the first three samples have the same characteristic peaks at $2\theta = 9.86^\circ$ and 13.09° , which correspond to the δ -phase of CsPbI₃. The latter three samples all have the characteristic peaks at $2\theta = 14.39^\circ$ and 28.97° , and they have the same light absorption edge at 716 nm ($E_g = 1.73$ eV), which verify the generation of γ -phase CsPbI₃.^{18,51}

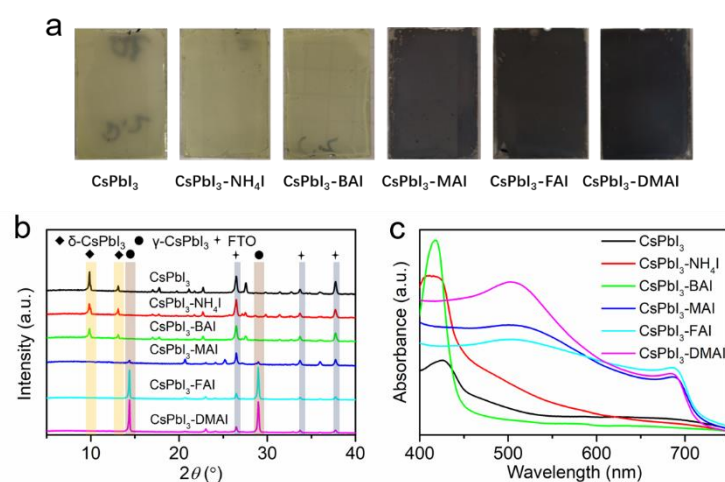


Figure 5.1. Phase transformation of CsPbI₃ film with different additives. Digital pictures (a), X-ray diffraction

spectra (XRD) (b), and UV-Vis spectra (c) of the annealed films of pure CsPbI₃ and with 1:1 mole ratio of NH₄I, BAI, MAI, FAI, and DMAI additives in precursor solutions, respectively.

The influence of the stoichiometric ratios of additives and CsPbI₃ in precursor solutions was further investigated (Figure 5.2). MAI, FAI, DMAI salts were added into the CsPbI₃ solution with mole ratios of 0.5, 0.75, and 1.0. As shown in the digital photos and XRD spectra, for MAI, both the annealed CsPbI₃-0.5MAI, CsPbI₃-0.75MAI films exhibit δ -phase CsPbI₃, while the CsPbI₃-MAI film exhibits black γ -phase. For FAI, the annealed CsPbI₃-0.5FAI film is δ -phase, and the CsPbI₃-0.75FAI and CsPbI₃-FAI films are pure γ -phase. For DMAI additive, it shows the same tendency as FAI. These experimental evidences indicate that the phase obtained is dependent on the additive content and a high additive content favors the black phase transformation for CsPbI₃. And the FA⁺ and DMA⁺ have stronger phase transformation ability than the MA⁺ at the same contents. Meanwhile, the formation of δ -phase CsPbI₃ films for CsPbI₃-2NH₄I and CsPbI₃-2BAI (Figure 5.3) further verify the weak ability of NH₄⁺ and BA⁺ for the formation of CsPbI₃ black phase.

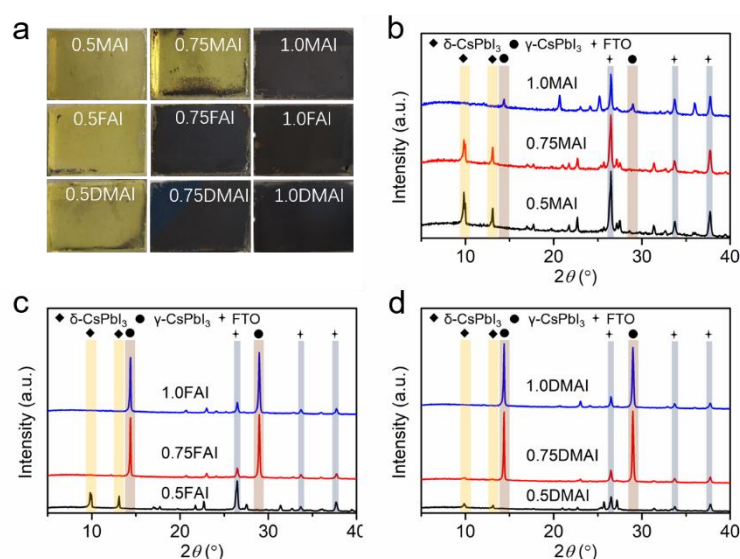


Figure 5.2. Phase transformation of CsPbI₃ films with additives of different ratios. Digital photos (a) and XRD spectra of MAI (b), FAI (c), and DMAI (d), respectively.

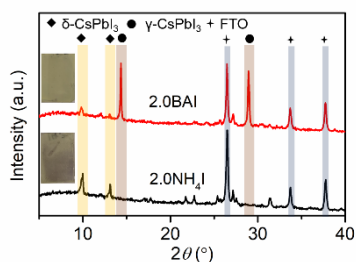


Figure 5.3. XRD spectra of CsPbI₃ film with BAI and NH₄I additives, the mole ratio is 1:2. The insets are corresponding digital photos of annealed films.

5.2.2 The process of phase transformation

The annealing processes of the fresh films after spin-coating are studied to analysis the mechanism of phase transformation. The digital photos and XRD spectra of the films annealed under 80 °C for 2 min and 330 °C for 5 min are shown in Figure 5.4 and 5.5. The fresh CsPbI₃ film is transparent and amorphous as the existence of excess DMSO solvent, which is denoted as CsPbI₃-xDMSO (Figure 5.4 and 5.5a). At 80 °C, the film transforms into black perovskite phase with a partial yellow phase within 60 s and then quickly degrades to yellow δ -phase in 120 s. The yellow δ -phase is maintained until the end of annealing under 330 °C for 5 min. The generation of an interim black phase may result from the formation of an intermediate phase CsPbI₃-xDMSO which promotes the transformation of a part of black phase.

For CsPbI₃-NH₄I, the transparent and amorphous CsPbI₃-NH₄I-xDMSO fresh film transforms into the black intermediate phase film consisting of 3D CsPbI₃ and low-dimensional NH₄(Cs)PbI₃ in 120 s under 80 °C, then it transforms into yellow δ -phase film under 330 °C with the evaporation of NH₄I (Figure 5.4 and 5.5b).

The amorphous CsPbI₃-BAI-xDMSO film, shown in Figure 5.4 and 5.5c, transforms into a red low-dimensional perovskite intermediate phase film without the generation of δ -phase CsPbI₃ at 80 °C. The red film maintained for 25 s at 330 °C and then it transforms into δ -phase CsPbI₃ with the evaporation of BAI. This process showed that the low-dimensional intermediate phases cannot transform into pure γ -phase CsPbI₃.

Figure 5.4 and 5.5d shows that the amorphous CsPbI₃-MAI-xDMSO fresh film quickly transforms into 3D black perovskite intermediate phase film under 80 °C in 2 min. The XRD of intermediate phase film show the left shift of the diffraction peaks compared to those of the black-phase CsPbI₃, which indicates the formation of a mixed cation MA_xCs_{1-x}PbI₃ (0<x<1) 3D perovskite intermediate phase. With the volatilization of MAI under 330 °C, the MA_xCs_{1-x}PbI₃ intermediate phase transforms into pure inorganic CsPbI₃ γ -phase.¹⁷⁷

Figure 5.4 and 5.5e shows that the amorphous CsPbI₃-FAI-xDMSO fresh film transforms into OIHP FA_xCs_{1-x}PbI₃ intermediate phase film under 80 °C in 2 min.¹⁷⁷ Then it further transforms into pure inorganic CsPbI₃ γ -phase with the volatilization of FAI during the annealing under 330 °C.

The fresh CsPbI₃-DMAI-xDMSO film annealed under 80 °C transforms into a yellow film, shown in Figure 5.4 and 5.5f. The characteristic diffraction peaks of the yellow film at near $2\theta = 11^\circ$ and 25.8° similar with these of 1D DMAPbI₃, indicates the formation of 1D intermediate phase. With the evaporation of part of DMAI, the film annealed under 330 °C for 43 s transforms into a black film including a 3D OIHP intermediate phase of DMA_xCs_{1-x}PbI₃ as the left-shift characteristic diffraction peaks at near $2\theta = 14^\circ$ and 29° compared to these of γ -

CsPbI₃. With the further volatilization of DMAI, the 3D OIHP intermediate phase transform into pure inorganic CsPbI₃ γ -phase.

Above all, these formation processes of CsPbI₃ films with various additives show the importance of the avoidance of the generation of δ -phase and the formation of a 3D OHIP intermediate phase.

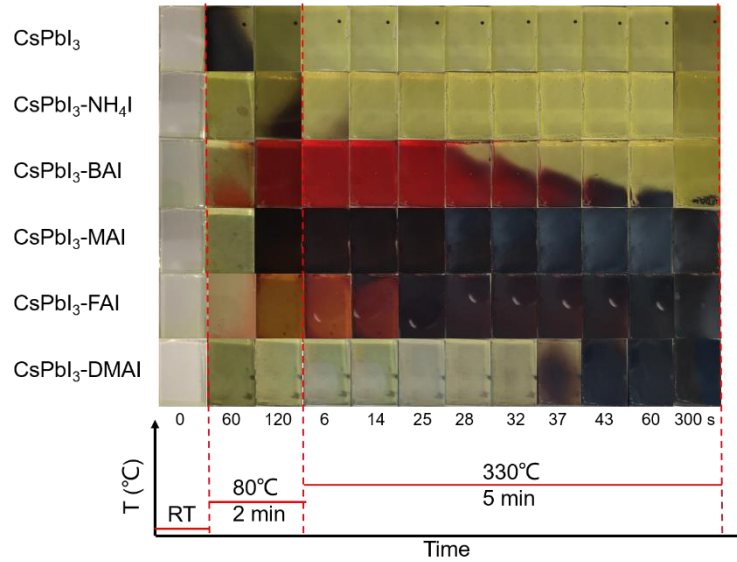


Figure 5.4. Digital photos of the phase transformation processes of pure CsPbI₃ and with 1:1 mole ratio of NH₄I, BAI, MAI, FAI, and DMAI in precursor solutions, respectively. The films were annealed with a gradient temperature at 80 °C for 2 min and 330 °C for 5 min.

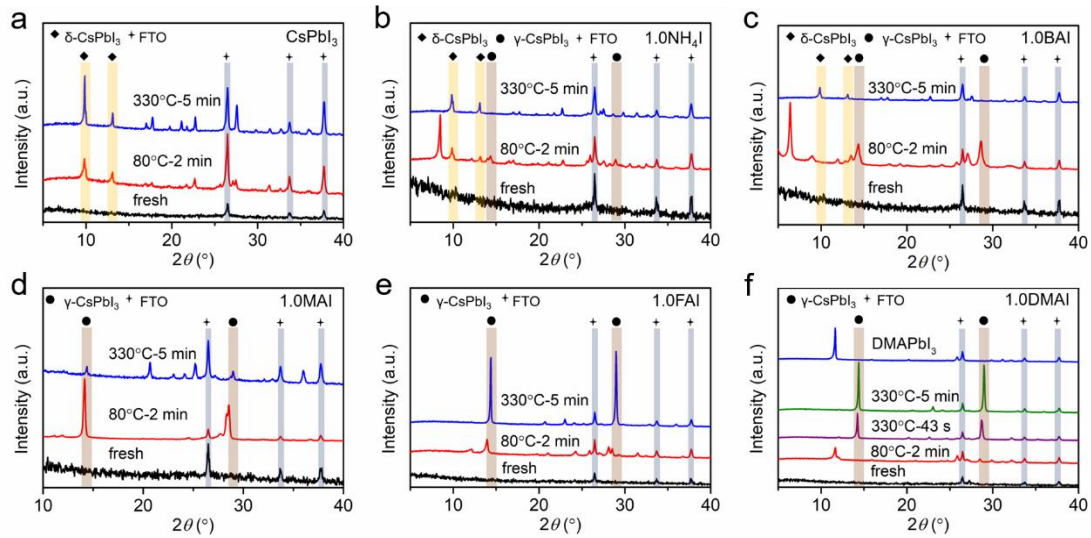


Figure 5.5. XRD spectra of the phase transformation processes of pure CsPbI₃ and with 1:1 mole ratio of NH₄I, BAI, MAI, FAI, and DMAI in precursor solutions, respectively. The films were annealed with a two-step temperature at 80 °C for 2 min and 330 °C for 5 min.

5.2.3 Performance and stability

The meso-devices with an architecture of Fluorine-doped tin oxide (FTO)/compact-TiO₂ (c-TiO₂)/meso-TiO₂/perovskite/2,2',7,7'-tetrakis(N,N-di-p-methoxyphenyl-amine)-9,9'-spirobifluorene (spiro-OMeTAD)/Au were fabricated (Figure 5.6a). The PCEs of the devices based on the CsPbI₃-MAI, CsPbI₃-FAI and CsPbI₃-DMAI are 15.99%, 14.86% and 16.63%, respectively (Figure 5.6b). The PCE differences should result from the difference of pinholes in surface morphology (Figure 5.6d-f).

The champion efficiency of the optimized CsPbI₃-DMAI device is 17.70% with an SPO of 17.58%, an open circuit voltage (V_{oc}) of 1.19 V, a short circuit current density (J_{sc}) of 18.57 mA cm⁻² and a fill factor (FF) of 80.11% (Figure 5.6c). The PCE is among the highest in inorganic PSCs without organic residues or modification in perovskite layers.

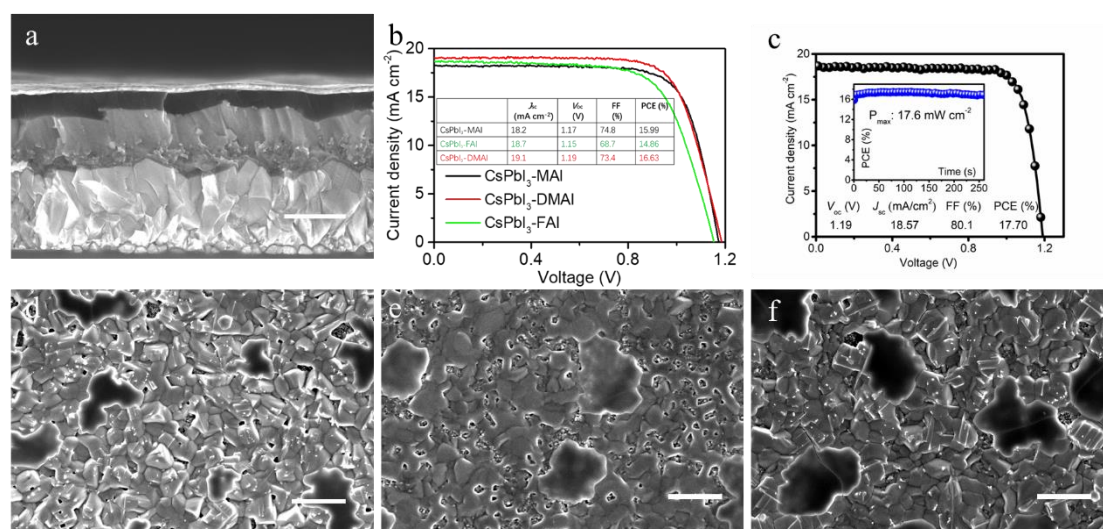


Figure 5.6. Performance of devices and film Morphology. (a) Cross-sectional SEM images of the CsPbI₃-DMAI device. Scale bar = 500 nm. (b) J - V curves of the CsPbI₃ devices with MAI, FAI, and DMAI additives, respectively. (c) J - V curve of champion CsPbI₃-DMAI device. The inset shows the SPO of the device for 260 s. (d-e) Top-view SEM images of the annealed CsPbI₃ films with MAI, FAI, and DMAI additives, respectively. Scale bar = 2 μ m.

5.3 Summary

According to the investigation of the phase transformation processes of CsPbI₃ with different volatile iodide salts additives (such as NH₄I, BAI, MAI, FAI and DMAI), the control CsPbI₃, CsPbI₃-NH₄I and CsPbI₃-BAI films transform into yellow δ -phase at 330 $^{\circ}$ C, while the CsPbI₃-

MAI, CsPbI₃-FAI and CsPbI₃-DMAI films promote the formation of the black phase CsPbI₃. The annealing procedures showed that the formation of a 3D OIHP intermediate phase is essential for avoiding the generation of yellow phase and promoting the formation of a pure CsPbI₃ black-phase. The champion efficiency of 17.70% with an SPO of 17.58% based on the optimized CsPbI₃-DMAI device is achieved.

5.4 Experimental section

5.4.1 Preparation method

Preparation of perovskite solutions The precursor chemicals were mixed stoichiometrically with anhydrous dimethyl sulfoxide (DMSO, ACROS, 99%) solvent and heated at 80 °C until completely dissolved. All precursor perovskite solutions are 1.35 M.

Device fabrication

Mesoscopic device architecture: FTO/compact-TiO₂(c-TiO₂)/meso-TiO₂/perovskite/spiro-OMeTAD/Au.

1. FTO glass sheet (Nippon Cor. Japan, 10 Ω /sq): A 3.5 mm ribbon area was etched away with zinc powder and 4 M HCl solution. Then the glass sheets were cleaned with 2% volume ratio Hellmanex solution, deionized water, acetone, and ethanol by sonication for 15 min in turns. Finally, the glass sheets were dried with air gas and treated with ultraviolet ozone for 15 min.
2. c-TiO₂: A 40 nm thick TiO₂ compact layer was deposited on top of FTO glasses by spray pyrolysis at 450 °C from a precursor solution containing 0.6 ml titanium diisopropoxide bis(acetylacetonate) (Sigma-Aldrich, 75 wt%) and 0.4 ml acetylacetone (Sigma-Aldrich, >99%) in 9 ml anhydrous ethanol.
3. meso-TiO₂: A 150 nm thick meso-TiO₂ layer was deposited by spin-coating a diluted TiO₂ paste (Dyesol, 30NR-D) with anhydrous ethanol (w:w = 1:6) at 4000 rpm for 20 s. Sheets were dried at 80 °C for 10 min and sintered at 450 °C for 30 min.
4. Perovskite layer: The perovskite films were prepared by spin-coating the precursor solutions in a two-step program at 1000 rpm and 3000 rpm for 10 s and 50 s, respectively. The films were placed in glovebox for 60 min, then annealed at 280 °C for 10 min in a dry-air glovebox.
5. Hole transport layer: The spiro-OMeTAD (Merck) chlorobenzene solution (90 mg ml⁻¹) with 20.6 μ l bis (trifluoromethane)sulfonimide lithium salt (Li-TFSI, Sigma-Aldrich, 520 mg ml⁻¹ in acetonitrile) and 35.5 μ l 4-*tert*-butylpyridine (*t*-BP, Sigma-Aldrich) was spin-coated on top of the perovskite film at 4000 rpm for 20 s. The devices were put into a dry-air glovebox (RH < 8%) for 12 h.

6. Electrode deposition: An 80 nm-thick gold electrode was deposited by thermal evaporation.

5.4.2 Characterization

SEM characterization A high-resolution SEM (Zeiss Merlin) with an in-lens detector was used for characterizing the top-view and cross-sectional morphologies of devices.

XRD measurements XRD patterns were acquired with a PANalytical Empyrean diffractometer in the transmission-reflection mode, using the Cu K α radiation and the Ni β -filter.

Optical characterization UV-Vis spectra were measured by Varian Cary 5. Band gaps (E_g) were derived from UV-Vis spectra with the Tauc-plot method. Photoluminescence spectra were measured by Fluorolog 322 (Horiba Jobin Yvon Ltd). Samples were excited at 450 nm by a standard 450 W xenon CW lamp. Time-resolved photoluminescence measurements were carried out by using a time-correlated single-photon counting (TCSPC) spectrometer (Fluorolog[®]-3, HORIBA Scientific). A diode laser (402 nm) was used as the excitation source, and a photomultiplier was used as the detector (Horiba TBX Picosecond Photon Detector).

Photovoltaic performance The PSCs were tested with a 450 W xenon light source (Oriel) in air at room temperature. The spectral mismatch between AM 1.5G and the solar simulator was calibrated by a Schott K113 Tempax filter. The light intensity was calibrated by a silicon photodiode for each measurement. The J-V curves were recorded by applying an external voltage bias with Keithley 2400 to give the corresponding current response with a scan rate of 10 mV/s (the voltage step is 5 mV with no delay time). Cells were covered by a black metal mask with an active area of 0.16 cm². Incident photon-to-current conversion efficiency (IPCE) measurements were carried out from the monochromatic visible photons, from Gemini-180 double monochromator Jobin Yvon Ltd., powered by a 300 W xenon light source (ILC Technology, USA) superimposed on a 1 mW cm⁻² LED light. The monochromatic incident light passed through a chopper running at 8 Hz frequency and the on/off ratio was measured by an operational amplifier.

Chapter 6 Conclusion

6.1 Main results achieved in this thesis

In the thesis, I summarize the developments of the materials, film formations and phase stabilization of lead-based inorganic halide perovskites. The studies in the thesis mainly focus on the stabilization of the inorganic perovskite phase by element doping and the formation of high-quality perovskite films by intermediate phase engineering (IPE) to improve the performance and stability of inorganic PSCs.

In chapter 2, we show the incorporation of europium into a CsPbI_2Br inorganic perovskite lattice, which leads to an enhancing stability of 6 months. The PCE of inorganic PSCs based on the $\text{CsPb}_{0.95}\text{Eu}_{0.05}\text{I}_2\text{Br}$ film is up to 13.71% with a SPO of 13.34%. The exceptional stability of such a device is demonstrated by retaining 93% of the initial efficiency under 100 mW cm^{-2} continuous illumination for 370 hr.

In chapter 3, Ba are introduced into mix halide CsPbI_2Br perovskite precursor solution. Barium does not incorporate into the perovskite lattice. Rather, it segregates into barium-based non-perovskite phases. This in turn leads to a change in the iodide-to-bromide ratio in the photoactive perovskite layer. EL measurements indicate that the non-radiative recombination is effectively inhibited upon the addition of barium, yielding a much higher V_{OC} of 1.33 V and a PCE of 14.0%.

In chapter 4, an intermediate-phase engineering strategy by utilizing volatile organic salts is carried out to achieve robust interfacial contact of inorganic perovskite and metal oxides. The introduction of organic cations (such as methylammonium and formamidinium) leads to the formation of an OIHP intermediate phase in the initial film and the high-quality interfacial contact. A champion $\text{CsPb}(\text{I}_{0.75}\text{Br}_{0.25})_3$ -based device with a power conversion efficiency of 17.0% and an open-circuit voltage of 1.34 V was realized.

In chapter 5, the procedures of phase transitions of CsPbI_3 with different additives (such as FAI, MAI, DMAI, NH_4I and BAI) in CsPbI_3 precursor solutions show that the 3D OIHP intermediate phase is essential for avoiding the generation of yellow phase and promoting the formation of pure CsPbI_3 black-phase. The PCE of 17.7% based on CsPbI_3 device is achieved, which is among the highest in inorganic PSCs without organic residues or modification in perovskite layers.

In summary, the investigations of element doping improve the stability of perovskite phase and illustrate the mechanism of element doping. Meanwhile, the studies of IPE show a new

technology for interfacial contact of inorganic perovskites and metal oxides, and promoting the formation of pure black-phase CsPbI₃ perovskite films for highly efficient inorganic PSCs.

6.2 Future development

In the thesis, I show that the element doping is an effective way to improve the phase stability of inorganic perovskites. Future work based on this may be to explore the cations or anions, which can be heavily doped into perovskite lattice to achieve the phase stability fundamentally.

Sn doping CsPbX₃ to form Sn-Pb mixed inorganic perovskites is likely to have large potential for high-efficiency and stable PSCs, as it shows higher phase stability to its Pb-based perovskites, stronger endurance to oxide and heating in comparison with its organic counterparts. and tunability of band gap from 1.3 to 2.3 eV, including the ideal value of 1.35 eV (from Shockley-Queisser theory) for single-junction solar cell. Thus, the PCE of Sn-Pb mixed inorganic PSCs has the potential to be higher than 20% of that of the Sn-Pb mixed OIHP solar cells in the nearly future. Especially they may achieve some new records for single-junction PSCs.

IPE is an effective method to improve the interfacial contact of inorganic perovskite and metal oxide transport layer. By replacing the organic hole transport layer (HTL) (such as spiro-OMeTAD) with inorganic HTM (such as NiOx and MnS), the all-inorganic PSCs are attracting extensive research due to their potential to achieve the stability of PSCs intrinsically. The IPE is likely to be effective to address the challenge of inorganic perovskite/inorganic HTM interfacial contact. As the suitable band gap of all-inorganic perovskites, the stable and high-efficiency all-inorganic perovskite/silicon tandem solar cells are very promising as the pioneers of the industrialization for PSCs.

Supplemental Information

Table S1.1 Perovskite materials, optimization and photovoltaic parameters of lead-based perovskite solar cells.

Materials (Band gap)	Year	Optimization/Research	V_{oc} (Max V_{oc})/V	J_{sc} (mA cm^{-2})	FF(%)	PCE/SP O (%)	Ref.
CsPbI ₃	2015	HI additive	0.80	12.00	30	2.90	46
CsPbI ₃	2016	sequential solvent engineering	0.66	11.92	52.47	4.13/3.09	28
CsPbI ₃	2017	Co-evaporation	1.063	13.8	71.6	10.5	72
CsPbI ₃	2017	Sequential vapor deposition	1.00	13.0	68	8.80/7.8	26
BA ₂ CsPb ₂ I ₇	2017	2D	0.957	8.88	57.0	4.84	81
CsPbI ₃ 0.025EDAP bI ₄	2017	Reduced-dimension	1.15	14.53	71	11.86	47
CsPbI ₃	2018	solvent-controlled growth	1.08	18.41	79.32	15.71	14
CsPbI ₃ QD (1.75eV)	2016	QD with short MeOAc ligand	1.23	13.47	65.0	10.77	99
CsPbI ₃ QD (1.75eV)	2018	μ -graphene (μ GR) to crosslink CsPbI ₃ QDs	1.16	13.59	72.6	11.4	100
CsPbI ₃ QD (1.75eV)	2017	FAI posttreatment	1.20	14.37	78	13.4	101
CsPbI ₃ (1.75eV)	2017	The modulation of oleylammonium or phenylethylammonium additives	1.06	15.0	41	6.5	102

Supplemental Information

CsPb _{0.96} Bi _{0.04} I ₃ (=1.56eV)	2017	Bi ³⁺ doped	0.97	18.76	72.59	13.21/13.17	⁹⁵
CsPbI ₃	2017	Modulation of sulfobetaine zwitterion additive	1.08	14.9	70	11.4/11.4	¹⁰⁵
γ-CsPbI ₃ (1.73)	2018	H ₂ O additive	1.04	16.53	65.7	11.30	²⁴
CsPbI ₃	2018	PVP modulation	1.11	14.88	65	10.74/10.0	¹⁰³
CsPbI ₃	2018	PTABr surface passivation	1.104	18.42	80.6	17.06/16.3	¹⁰⁷
CsPbI ₃	2018	PEAI surface passivation	1.11	18.51	69.6	14.3/13.5	¹⁰⁶
CsPbI ₃ -0.05EuCl ₃	2018	EuCl ₃ doped	0.898	11.1	68	6.8/4.5	¹⁸⁰
PEA ₂ Cs _{n-1} Pb _n X _{3n+1} (n=60)	2018	Reduced-dimension	1.07	16.25	70	12.4	⁸²
Cs _{0.7} DMA _{0.3} PbI ₃ (1.7eV)	2018	DMA ⁺ doping	0.99	16.65	76.49	12.62	⁵⁰
γ-CsPbI ₃	2019	MAI additive	1.02	17.4	79.4	14.1	⁵⁴
β-CsPbI ₃ (1.68eV)	2019	β-CsPbI ₃ from DMAI and choline iodide surface passivation	1.11	20.2	82	18.4	¹⁵
β-CsPbI ₃	2019	The role of DMAI and PTACl surface passivation	1.137	20.23	82.7	19.03	¹⁶
DMA _{0.15} Cs _{0.85} PbI ₃ (1.65eV)	2019	Phase evolution of CsPbI ₃ -DMAI	1.05	19.4	0.75	15.3	⁵¹
Cs _{0.5} DMA _{0.5} PbI ₃ (about 1.7eV)	2019	Varying the ratio of CsI/DMAPI ₃	1.054	18.4	0.74	14.3/12.8	⁵³

Supplemental Information

CsPb _{0.6} Sn _{0.4} I ₃ (1.38eV)	2020	Sn-Pb alloying, incorporating SnF ₂ •3FACl additive and (4AMP)I ₂ passivation	0.774	25.87	66.7	13.37/12.51	⁸⁵
CsPbI ₃	2020	(Adamantan-1-yl) methan ammonium (ADMA) introducing and all-inorganic PSC	1.09	18.29	80.50	16.04	⁵⁷
CsPbI ₃ :Br:InI ₃ (1.74eV)	2020	In ³⁺ doped, dipped method and all-inorganic PSCs	1.20	15.68	64	12.04	⁷⁸
CsPbI _{3-x} Br _x (1.77eV)	2019	LiF passivated SnO ₂ and Cl doped perovskite	1.234(1.25)	18.3	82.58	18.64/16.9	⁴⁸
CsPbI _{2.25} Br _{0.75} (1.86eV)	2020	Intermediate phase engineering promoting interfacial contact	1.34	15.9	79.6	17.0/16.2	¹⁷⁷
CsPbI ₂ Br	2016	Bandgap-Tunable CsPbX ₃	1.11	11.89	75	9.84/5.6	⁴⁰
CsPbI ₂ Br	2016	Phase segregation	1.06	10.9	58.9	6.8/6.5	⁴¹
CsPbI ₂ Br	2017	Light-independent	-	-	-	10.5/9.3	⁴³
CsPb _{0.98} Sr _{0.02} I ₂ Br	2017	Sr-doped	1.043	15.30	70	11.30/10.80	⁸⁹
CsPbI ₂ Br	2017	Annealing temperature	1.23	12.0	0.73	10.7/9.5	⁶⁶
Cs _{0.925} K _{0.075} PbI ₂ Br	2017	K-doped	1.18	11.6	73	10.00/9	⁴⁵
CsPbI ₂ Br	2018	Solvent modulation	0.98	14.18	0.66	9.14/8.8	⁵⁹

Supplemental Information

						4	
CsPbI ₂ Br	2018	Low-temperature and solvent modulation	1.162	15.566	79.06	14.3/14.6	58
CsPbI ₂ Br-0.02MnCl ₂	2018	Mn ²⁺ doping	1.172	14.37	80.0	13.47/13.37	88
CsPbI ₂ Br	2018	PbI ₂ (DMSO) and PbI ₂ (DMSO) precursors	1.22	15.33	78.7	14.78/14.67	60
CsPbI ₂ Br	2018	Gradient thermal annealing and inverted all-inorganic PSC structure.	1.14	15.2	77	13.3/12	63
CsPbI ₂ Br	2018	Room-temperature solvent (DMSO) annealing treatment	0.93	11.1	61.8	6.4	69
CsPbI ₂ Br	2018	Pulsed flash infrared annealing	1.288	12.3	65	10.3	68
CsPbI ₂ Br	2019	MA gas healing method	1.25	14.6	72	13.1/13.0	56
CsPbI ₂ Br	2019	CsAc+MABr+PbI ₂	1.18	15.2	79.3	14.23/13.4	55
CsPb _{0.96} Sb _{0.04} I ₃	2018	Sb-doping	0.73	14.64	48	5.18	97
CsPbI _{2+x} Br _{1-x} (1.82eV)	2018	CsPbI ₃ QDs surface modulation inducing a graded bandgap CsPbI _{2+x} Br _{1-x}	1.204	14.45	78.7	14.45/14.41	108
CsPbI ₂ Br-0.0025InCl ₃	2018	InCl ₃ doping	1.14	15.7	77	13.74/12.4	96
		1cm*1cm	1.1	15.5	67	11.4/10.4	

Supplemental Information

CsPbI ₂ Br	2019	Oxygen passivation	1.18	16.31	78.8	15.17	67
CsPbI ₂ Br	2019	Gradient thermal annealing and antisolvent	1.23	16.79	77.81	16.07/15.75	62
CsPbI ₂ Br	2019	Dynamic hot-air casting process	1.21	15.45	79.45	14.85	64
		Large-scale (1cm*1cm)	1.217	15.26	75.25	13.78/13.6	
CsPb _{0.95} Eu _{0.05} I ₂ Br	2019	Eu-doped	1.22 (1.27)	14.63	76.6	13.71/13.34	135
CsPb _{0.8} Ba _{0.2} I ₂ Br	2019	Ba-dopping	1.28/1.33	14.0	78.2	14.0/13.6	39
CsPb _{0.98} Ni _{0.02} I ₂ Br	2019	Ni-doped	1.141	16.02	75.96	13.88/12.84	90
CsPbI ₂ Br/CuBr ₂ (0.2 wt %) (1.95eV)	2019	CuBr ₂ doped	1.18	16.95	80	16.15/15.93	91
CsPbIBr ₂	2016	Co-evaporation and HTM-free	0.959	8.7	56	4.7	71
CsPbIBr ₂	2017		1.227	9.69	67.4	8.02/6.07	42
CsPbIBr ₂	2017	Dipping method and Free-HTM all-inorganic PSCs	1.08	12.32	62	8.25	77
CsPb _{0.995} Mn _{0.005} I _{1.01} Br _{1.99}	2018	Mn-dopping	0.99	13.15	0.57	7.36	181
CsPb _{0.9} Sn _{0.1} IBr ₂ (Eg =1.79eV)	2017	Dipping and Sn-dopped	1.26	14.3	63	11.33/10.1	77

Supplemental Information

CsPbBr ₃	2015	Dipping method	1.28	6.24	74	5.95	⁷⁵
CsPbBr ₃	2016	Dipping method and HTM-Free all-inorganic PSCs	1.24	7.4	73	6.7	⁷⁶
CsPbBr ₃	2019	Face-down dipping method	1.34	6.46	68.04	5.86	⁷⁹
CsPbBr ₃	2019	One-step solution method	1.23	7.19	73.1	7.37/6.91	⁶¹
CsPbBr ₃	2018	Multi-step spin-coating	1.458	8.12	82.1	7.72	³⁷
CsPb _{0.97} Sm _{0.03} Br ₃	2018	Ln ³⁺ - (Sm ³⁺ , Tb ³⁺ , Ho ³⁺ , Er ³⁺ , and Yb ³⁺) doped	1.594	7.48	85.1	10.14	⁹⁸
Cs _{0.91} Rb _{0.09} PbBr ₃	2018	Alkali metal cations (such as Rb ⁺ , K ⁺ , Na ⁺ , Li ⁺) doped	1.552	7.73	82.2	9.86	⁸³
CsPb _{0.97} Sr _{0.03} Br ₃	2019	Mg ²⁺ , Ca ²⁺ , Sr ²⁺ , Ba ²⁺ -doped	1.54	7.71	81.1	9.63	⁹²
CsPbBr ₃	2019	Sequential vapor deposition and gradient bandgap architecture	1.461	9.24	75.39	10.17	³⁸
Others							
Cs ₂ PbI ₂ (SCN) ₂ (2.05eV)	2018	2D all-inorganic perovskite	0.94	4.55	48	2.04	⁸⁰

Table S3.1. DFT calculated ^{133}Cs chemical shieldings and referenced chemical shifts of the CsBaPbBr_3 clusters.

System	Description	Calculated chemical [pm]	^{133}Cs shielding	Calculated chemical [ppm]	^{133}Cs shift	Experimental chemical shift [ppm]	^{133}Cs
Reference systems							
(tetragonal) rt- CsPbCl_3	(tetragonal) rt- CsPbCl_3 cluster	6390.8		60.9		71	
(hexagonal) δ - CsPbI_3	(hexagonal) δ - CsPbI_3 cluster	5940.4		235.5		240	
(orthorhombic) rt- CsPbBr_3	(orthorhombic) rt- CsPbBr_3 cluster	6249.2		115.8		100.5	
Structures based on the cubic (Pm-3m) structure of CsPbBr_3							
$\text{Cs}_{20}\text{Pb}_8\text{Br}_{36}$ (CsPbBr_3)	unperturbed cubic CsPbBr_3 cluster	6459.67		34.2		-	
$\text{Cs}_{20}\text{BaPb}_7\text{Br}_{36}$ ($\text{Cs}(\text{Pb-Ba})\text{Br}_3$)	Cs centered with one surrounding Pb replaced by Ba	6451.21		37.5		-	
$\text{BaCs}_{18}\text{Pb}_8\text{Br}_{36}$ (1NN_edge)	1 nearest neighbor Cs replaced by Ba on adjacent edge	6455.86		35.7		-	
$\text{BaCs}_{18}\text{Pb}_8\text{Br}_{36}$ (1NN_surf)	1 nearest neighbor Cs replaced by Ba on adjacent surface	6449.57		38.1		-	

Ba ₂ Cs ₁₆ Pb ₈ Br ₃₆	2 nearest neighbor Cs			
(2NN_surfO)	replaced by Ba on opposite surfaces	6438.06	42.6	-
Ba ₂ Cs ₁₆ Pb ₈ Br ₃₆	2 nearest neighbor Cs			
(2NN_surfA)	replaced by Ba on adjacent surfaces	6436.44	43.2	-
Ba ₂ Cs ₁₆ Pb ₈ Br ₃₆	2 nearest neighbor Cs			
(2NN_edge)	replaced by Ba on opposite edges	6452.22	37.1	-
Ba ₃ Cs ₁₄ Pb ₈ Br ₃₆	3 nearest neighbor Cs			
(3NN_surfP)	replaced by Ba on adjacent surfaces in a plane	6428.11	46.5	-
Ba ₃ Cs ₁₄ Pb ₈ Br ₃₆	3 nearest neighbor Cs			
(3NN_surfC)	replaced by Ba on adjacent surfaces around a corner	6426.40	47.1	-
Structures based on the orthorhombic (Pnma) room temperature structure of CsPbBr ₃				
Cs ₂₀ Pb ₈ Br ₃₆	unperturbed orthorhombic	6249.1	115.8	
(CsPbBr ₃)	CsPbBr ₃ cluster			
Cs ₂₀ BaPb ₇ Br ₃₆	Cs centered with one surrounding Pb	6241.8	118.7	
(Cs(Pb-Ba)Br ₃)	replaced by Ba			

Supplemental Information

BaCs ₁₈ Pb ₈ Br ₃₆	1 nearest neighbor Cs		
(1NN_Nsurf)	replaced by Ba on narrow adjacent surface	6245.7	117.2
BaCs ₁₈ Pb ₈ Br ₃₆	1 nearest neighbor Cs		
(1NN_Wsurf)	replaced by Ba on wide adjacent surface	6244.5	117.6
BaCs ₁₈ Pb ₈ Br ₃₆	1 nearest neighbor Cs		
(1NN_Nedge)	replaced by Ba on narrow adjacent edge	6247.0	116.6
BaCs ₁₈ Pb ₈ Br ₃₆	1 nearest neighbor Cs		
(1NN_Wedge)	replaced by Ba on wide adjacent edge	6244.5	117.6

Table S4.1. Perovskite materials, band gaps and photovoltaic parameters of reported highly efficient inorganic perovskite solar cells without organic residues or modification in perovskite layers and wide band gap (1.72 eV-2.3 eV) organic-inorganic hybrid perovskite solar cells and our devices.

Materials and Ref.	Band gap (eV) ^a	V _{oc} (V)	$\frac{V_{oc}}{V_{oc} - Q}$ (%) ^b	J _{sc} (mA cm ⁻²)	FF (%)	PCE (%)	$\frac{PCE}{PCE_{S-Q}}$ (%) ^c
CsPbI ₃ ¹⁵	1.72	1.05	73.2	20.03	72	15.1	52.9
CsPbI ₃ ¹⁶	1.72	1.066	74.3	20.09	77.6	16.62	58.3
CsPbI ₃ ¹⁰⁷	1.72	1.051	76.4	18.88	68.5	13.59	59.8
CsPbI ₃ ¹⁴	1.72	1.08	75	18.41	79.32	15.71	55.1
CsPbI ₃ ⁹⁹	1.75	1.23	84.2	13.47	65	10.77	38.6
CsPbI ₂ Br ⁶⁰	1.92	1.22	75.3	15.33	78.7	14.78	60.57
CsPbI ₂ Br ⁸⁸	1.92	1.17	72.2	14.37	80	13.47	55.2
CsPbI ₂ Br ¹⁸²	1.92	1.3	80.2	13.13	70.4	12.02	49.3
CsPbI ₂ Br ¹⁸³	1.92	1.23	75.9	15	78.8	14.6	58.6
CsPbI ₂ Br ¹⁸⁴	1.92	1.205	74.4	14.69	77.4	14.49	59.4
CsPbI ₂ Br ¹³⁵	1.92	1.22(1.27)	78.4	14.63	76.6	13.71	56.2
CsPbIBr ₂ ¹⁸⁵	2.06	1.23(1.31)	74.9	8.5	67	7	32.6
CsPbIBr ₂ ⁴²	2.06	1.227	70.1	9.69	67.4	8.02	37.3
CsPbBr ₃ ¹⁸⁶	2.3	1.52	76.8	-	-	9.43	57.5
CsPbBr ₃ ³⁷	2.3	1.46	73.7	8.12	82.1	9.72	59.2
CsPbBr ₃ ⁹²	2.3	1.54	77.8	7.71	81.1	9.63	58.7
CsPbBr ₃ ⁹⁸	2.3	1.594	80.5	7.48	85.1	10.14	61.8
CsPbBr ₃ ¹⁸⁷	2.3	1.505	76.0	5.512	62.8	5.2	31.7

Supplemental Information

$\text{FA}_{0.15}\text{Cs}_{0.85}\text{Pb}(\text{I}_{0.73}\text{Br}_{0.27})_3^{188}$	1.72	1.24	86.1	19.83	73.7	18.1	63.5
$\text{FA}_{0.83}\text{MA}_{0.17}\text{Pb}(\text{I}_{0.6}\text{Br}_{0.4})_3^{189}$	1.72	1.15	79.9	19.4	77.0	17.2	60.4
$\text{BA}_{0.09}(\text{FA}_{0.83}\text{Cs}_{0.17})_{0.91}\text{Pb}(\text{I}_{0.6}\text{Br}_{0.4})_3^{190}$	1.72	1.18	81.9	19.8	73.0	17.3	60.7
$\text{FA}_{0.75}\text{MA}_{0.15}\text{Cs}_{0.1}\text{Rb}_{0.05}\text{Pb}(\text{I}_{0.67}\text{Br}_{0.33})_3^{191}$	1.73	1.13	77.9	-	-	17.3	60.9
$\text{FA}_{0.83}\text{MA}_{0.17}\text{Pb}(\text{I}_{0.6}\text{Br}_{0.4})_3^{192}$	1.74	1.20	82.2	19.4	75.1	17.1	60.9
$\text{FA}_{0.8}\text{Cs}_{0.2}\text{Pb}(\text{I}_{0.6}\text{Br}_{0.4})_3^{193}$	1.75	1.23	84.2	18.1	76.0	17.8	63.8
$\text{FA}_{0.8}\text{Cs}_{0.2}\text{Pb}(\text{I}_{0.7}\text{Br}_{0.3})_3^{194}$	1.75	1.23	84.2	18.5	77.8	17.7	63.4
$\text{FA}_{0.75}\text{Cs}_{0.25}\text{Pb}(\text{I}_{0.8}\text{Br}_{0.2})_3^{195}$	1.75	1.17	80.1	17.5	80.	16.3	58.4
$\text{FA}_{0.33}\text{MA}_{0.67}\text{PbI}_2\text{Br}^{196}$	1.76	1.17	79.6	20.4	73.	17.5	63.2
$\text{Cs}_{0.06}\text{FA}_{0.79}\text{MA}_{0.15}\text{Pb}(\text{I}_{0.4}\text{Br}_{0.6})_3^{197}$	1.78	1.23	82.6	17.9	79	17.5	64.1
$\text{FA}_{0.83}\text{Cs}_{0.17}\text{Pb}(\text{I}_{0.5}\text{Br}_{0.5})_3^{155}$	1.8	1.12	74.2	15.1	58	9.8	36.3
$\text{Cs}_{0.6}\text{MA}_{0.4}\text{Pb}(\text{I}_{0.6}\text{Br}_{0.4})_3^{198}$	1.81	1.17	77.0	13.9	68.3	11.1	41.4
$\text{MAPb}(\text{I}_{0.6}\text{Br}_{0.4})_3^{199}$	1.82	1.30	85.0	12.9	65	11.6	43.8
$\text{MA}_{0.90}\text{Cs}_{0.10}\text{Pb}(\text{I}_{0.6}\text{Br}_{0.4})_3^{200}$	1.82	1.22	79.7	15.1	69	12.5	47.2
FAPbBr_3^{201}	2.2	1.5	79.8	6.9	69	7.1	38.6
FAPbBr_3^{202}	2.2	1.53	81.4	7.3	71	8.2	44.6
FAPbBr_3^{203}	2.2	1.47	78.2	6.7	69	6.8	37.0
MAPbBr_3^{204}	2.2	1.65	87.8	7.72	79	10.1	54.9
MAPbBr_3^{205}	2.2	1.61	85.6	6.04	77	7.50	40.8
Our work	1.86	1.34	86.0	15.9	79.6	17.0	66.1

^aThe band gaps of perovskite with the same chemical formula are slightly different in different literatures. They were unified when calculating the corresponding Shockley-Queisser (S-Q) values.

^{b, c}The S-Q theoretical values for PCE and V_{oc} are given in Supplemental Information “Photovoltaic parameters of

Shockley-Queisser (S-Q) limit.excel”.

References

- 1 Kojima, A., Teshima, K., Shirai, Y. & Miyasaka, T. Organometal halide perovskites as visible-light sensitizers for photovoltaic cells. *J. Am. Chem. Soc.* **131**, 6050-6051 (2009).
- 2 Stoumpos, C. C., Malliakas, C. D. & Kanatzidis, M. G. Semiconducting tin and lead iodide perovskites with organic cations: Phase transitions, high mobilities, and near-infrared photoluminescent properties. *Inorg. Chem.* **52**, 9019-9038 (2013).
- 3 Lee, M. M., Teuscher, J., Miyasaka, T., Murakami, T. N. & Snaith, H. J. Efficient hybrid solar cells based on meso-superstructured organometal halide perovskites. *Science* **338**, 643-647 (2012).
- 4 Kim, H. S. *et al.* Lead iodide perovskite sensitized all-solid-state submicron thin film mesoscopic solar cell with efficiency exceeding 9%. *Sci. Rep.* **2**, 591 (2012).
- 5 Dong, Q. *et al.* Electron-hole diffusion lengths > 175 μm in solution-grown $\text{CH}_3\text{NH}_3\text{PbI}_3$ single crystals. *Science* **347**, 967-970 (2015).
- 6 Chen, Q. *et al.* All-inorganic perovskite nanocrystal scintillators. *Nature* **561**, 88-93 (2018).
- 7 Lin, K. *et al.* Perovskite light-emitting diodes with external quantum efficiency exceeding 20 per cent. *Nature* **562**, 245-248 (2018).
- 8 Jena, A. K., Kulkarni, A. & Miyasaka, T. Halide perovskite photovoltaics: Background, status, and future prospects. *Chem. Rev.* **119**, 3036-3103 (2019).
- 9 Oregan, B. & Gratzel, M. A low-cost, high-efficiency solar-cell based on dye-sensitized colloidal TiO_2 films. *Nature* **353**, 737-740 (1991).
- 10 Laboratory, N. R. E. *Best research-cell efficiencies*, <<https://www.nrel.gov/pv/assets/pdfs/best-research-cell-efficiencies.pdf>> (2020.06.04).
- 11 Boyd, C. C., Cheacharoen, R., Leijtens, T. & McGehee, M. D. Understanding degradation mechanisms and improving stability of perovskite photovoltaics. *Chem. Rev.* **119**, 3418-3451 (2019).
- 12 Zhou, Y. & Zhao, Y. Chemical stability and instability of inorganic halide perovskites. *Energy Environ. Sci.* **12**, 1495-1511 (2019).
- 13 Zhang, J., Hodes, G., Jin, Z. & Liu, S. F. All-inorganic CsPbX_3 perovskite solar cells: progress and prospects. *Angew. Chem. Int. Ed.* **58**, 15596-15618 (2019).
- 14 Wang, P. *et al.* Solvent-controlled growth of inorganic perovskite films in dry environment for efficient and stable solar cells. *Nat. Commun.* **9**, 2225 (2018).
- 15 Wang, Y. *et al.* Thermodynamically stabilized β - CsPbI_3 -based perovskite solar cells with efficiencies >18%. *Science*, 591-595 (2019).
- 16 Wang, Y. *et al.* The role of dimethylammonium iodide in CsPbI_3 perovskite fabrication: Additive or dopant? *Angew. Chem. Int. Ed.* **131**, 2-8 (2019).
- 17 Polman, A., Knight, M., Garnett, E. C., Ehrler, B. & Sinke, W. C. Photovoltaic materials: Present efficiencies and future challenges. *Science* **352**, 307 (2016).
- 18 Marronnier, A. *et al.* Anharmonicity and disorder in the black phases of cesium lead iodide used for stable inorganic perovskite solar cells. *ACS Nano* **12**, 3477-3486 (2018).
- 19 Stoumpos, C. C. & Kanatzidis, M. G. The renaissance of halide perovskites and their evolution

- as emerging semiconductors. *Acc. Chem. Res.* **48**, 2791-2802 (2015).
- 20 Deng, J., Li, J., Yang, Z. & Wang, M. All-inorganic lead halide perovskites: a promising choice for photovoltaics and detectors. *J. Mater. Chem. C* **7**, 12415-12440 (2019).
- 21 Steele, J. A. *et al.* Thermal unequilibrium of strained black CsPbI₃ thin films. *Science* **365**, 679–684 (2019).
- 22 Huang, Y., Yin, W.-J. & He, Y. Intrinsic point defects in inorganic cesium lead iodide perovskite CsPbI₃. *J. Phys. Chem. C* **122**, 1345-1350 (2018).
- 23 Yin, W.-J., Shi, T. & Yan, Y. Unusual defect physics in CH₃NH₃PbI₃ perovskite solar cell absorber. *Appl. Phys. Lett.* **104**, 063903 (2014).
- 24 Zhao, B. *et al.* Thermodynamically stable orthorhombic gamma-CsPbI₃ thin films for high-performance photovoltaics. *J. Am. Chem. Soc.* **140**, 11716-11725 (2018).
- 25 Pazos-Outon, L. M. *et al.* Photon recycling in lead iodide perovskite solar cells. *Science* **351**, 1430-1433 (2016).
- 26 Hutter, E. M. *et al.* Vapour-deposited cesium lead iodide perovskites: Microsecond charge carrier lifetimes and enhanced photovoltaic performance. *ACS Energy Lett.* **2**, 1901-1908 (2017).
- 27 Dastidar, S., Li, S., Smolin, S. Y., Baxter, J. B. & Fafarman, A. T. Slow electron–hole recombination in lead iodide perovskites does not require a molecular dipole. *ACS Energy Lett.* **2**, 2239-2244 (2017).
- 28 Luo, P. *et al.* Solvent engineering for ambient-air-processed, phase-stable CsPbI₃ in perovskite solar cells. *J. Phys. Chem. Lett.* **7**, 3603-3608 (2016).
- 29 Xiao, Z., Meng, W., Wang, J., Mitzi, D. B. & Yan, Y. Searching for promising new perovskite-based photovoltaic absorbers: the importance of electronic dimensionality. *Materials Horizons* **4**, 206-216 (2017).
- 30 Stoumpos, C. C. *et al.* Crystal growth of the perovskite semiconductor CsPbBr₃: A new material for high-energy radiation detection. *Crystal Growth & Design* **13**, 2722-2727 (2013).
- 31 Song, J. *et al.* Ultralarge all-inorganic perovskite bulk single crystal for high-performance visible-infrared dual-modal photodetectors. *Advanced Optical Materials* **5**, 1700157 (2017).
- 32 Kulbak, M. *et al.* Control over self-doping in high band gap perovskite films. *Adv. Energy Mater.* **8**, 1800398 (2018).
- 33 Yang, Z. *et al.* Engineering the exciton dissociation in quantum-confined 2D CsPbBr₃ nanosheet films. *Adv. Funct. Mater.* **28**, 1705908 (2018).
- 34 Yang, L. *et al.* Extrinsic photoluminescence properties of individual micro-particle of Cs₄PbBr₆ perovskite with "defect" structure. *Optics Express* **27**, 31207-31216 (2019).
- 35 Zhang, Z. *et al.* Growth, characterization and optoelectronic applications of pure-phase large-area CsPb₂Br₅ flake single crystals. *J. Mater. Chem. C* **6**, 446-451 (2018).
- 36 Tong, G., Ono, L. K. & Qi, Y. Recent progress of all-bromide inorganic perovskite solar cells. *Energy Technology*, 1900961 (2019).
- 37 Duan, J., Zhao, Y., He, B. & Tang, Q. High-purity inorganic perovskite films for solar cells with 9.72 % efficiency. *Angew. Chem. Int. Ed.* **57**, 3787-3791 (2018).
- 38 Tong, G. *et al.* High efficient hole extraction and stable all-bromide inorganic perovskite solar cells via derivative-phase gradient bandgap architecture. *Solar RRL* **3**, 1900030 (2019).
- 39 Xiang, W. *et al.* Ba-induced phase segregation and band gap reduction in mixed-halide inorganic

- perovskite solar cells. *Nat. Commun.* **10**, 4686 (2019).
- 40 Sutton, R. J. *et al.* Bandgap-tunable cesium lead halide perovskites with high thermal stability for efficient solar cells. *Adv. Energy Mater.* **6**, 1502458 (2016).
- 41 Beal, R. E. *et al.* Cesium lead halide perovskites with improved stability for tandem solar cells. *J. Phys. Chem. Lett.* **7**, 746-751 (2016).
- 42 Li, W. *et al.* Phase segregation enhanced ion movement in efficient inorganic CsPbIBr₂ Solar Cells. *Adv. Energy Mater.* **7**, 1700946 (2017).
- 43 Zhou, W. *et al.* Light-independent ionic transport in inorganic perovskite and ultrastable Cs-based perovskite solar cells. *J. Phys. Chem. Lett.* **8**, 4122-4128 (2017).
- 44 Kennedy, C. L., Hill, A. H., Massaro, E. S. & Grumstrup, E. M. Ultrafast excited-state transport and decay dynamics in cesium lead mixed halide perovskites. *ACS Energy Lett.* **2**, 1501-1506 (2017).
- 45 Nam, J. K. *et al.* Potassium incorporation for enhanced performance and stability of fully inorganic cesium lead halide perovskite solar cells. *Nano Lett.* **17**, 2028-2033 (2017).
- 46 Eperon, G. E. *et al.* Inorganic caesium lead iodide perovskite solar cells. *J. Mater. Chem. A* **3**, 19688-19695 (2015).
- 47 Zhang, T. Y. *et al.* Bication lead iodide 2D perovskite component to stabilize inorganic a-CsPbI₃ perovskite phase for high-efficiency solar cells. *Sci. Adv.* **3**, 6 (2017).
- 48 Ye, Q. *et al.* Cesium lead inorganic solar cell with efficiency beyond 18% via reduced charge recombination. *Adv. Mater.* **31**, e1905143 (2019).
- 49 Zheng, Y. *et al.* High - performance CsPbI_xBr_{3-x} all - inorganic perovskite solar cells with efficiency over 18% via spontaneous interfacial manipulation. *Adv. Funct. Mater.*, 2000457 (2020).
- 50 Ke, W., Spanopoulos, I., Stoumpos, C. C. & Kanatzidis, M. G. Myths and reality of HPbI₃ in halide perovskite solar cells. *Nat. Commun.* **9**, 4785 (2018).
- 51 Meng, H. *et al.* Chemical composition and phase evolution in DMAI-derived inorganic perovskite solar cells. *ACS Energy Lett.* **5**, 263-270 (2019).
- 52 Anelli, C. *et al.* Investigation of dimethylammonium solubility in MAPbBr₃ hybrid perovskite: synthesis, crystal structure, and optical properties. *Inorg. Chem.* **58**, 944-949 (2018).
- 53 Pei, Y. *et al.* Unveiling property of hydrolysis-derived DMAPbI₃ for perovskite devices: Composition engineering, defect mitigation, and stability optimization. *iScience* **15**, 165-172 (2019).
- 54 Lau, C. F. J. *et al.* Fabrication of efficient and stable CsPbI₃ perovskite solar cells through cation exchange process. *Adv. Energy Mater.* **9**, 1901685 (2019).
- 55 Zhang, T. *et al.* Organic salt mediated growth of phase pure and stable all-inorganic CsPbX₃ (X=I, Br) perovskites for efficient photovoltaics. *Sci. Bull.* (2019).
- 56 Shao, Z. *et al.* A scalable methylamine gas healing strategy for high-efficiency inorganic perovskite solar cells. *Angew. Chem. Int. Ed.* **58**, 5587-5591 (2019).
- 57 Liu, C. *et al.* Soft template-controlled growth of high-quality CsPbI₃ films for efficient and stable solar cells. *Adv. Energy Mater.*, 1903751 (2020).
- 58 Zai, H. *et al.* Low-temperature-processed inorganic perovskite solar cells via solvent engineering with enhanced mass transport. *J. Mater. Chem. A* **6**, 23602-23609 (2018).

- 59 Zhang, S. *et al.* Solvent engineering for efficient inverted perovskite solar cells based on inorganic CsPbI₂Br light absorber. *Materials Today Energy* **8**, 125-133 (2018).
- 60 Yin, G. *et al.* Precursor engineering for all-inorganic CsPbI₂Br perovskite solar cells with 14.78% efficiency. *Adv. Funct. Mater.* **28**, 1803269 (2018).
- 61 Huang, D., Xie, P., Pan, Z., Rao, H. & Zhong, X. One-step solution deposition of CsPbBr₃ based on precursor engineering for efficient all-inorganic perovskite solar cells. *J. Mater. Chem. A* **7**, 22420-22428 (2019).
- 62 Chen, W. *et al.* Precise control of crystal growth for highly efficient CsPbI₂Br perovskite solar cells. *Joule* **3**, 191-204 (2019).
- 63 Liu, C. *et al.* All-Inorganic CsPbI₂Br perovskite solar cells with high efficiency exceeding 13%. *J. Am. Chem. Soc.* **140**, 3825-3828 (2018).
- 64 Mali, S. S., Patil, J. V. & Hong, C. K. Hot-air-assisted fully air-processed barium incorporated CsPbI₂Br perovskite thin films for highly efficient and stable all-inorganic perovskite solar cells. *Nano Lett.* **19**, 6213-6220 (2019).
- 65 Jeon, N. J. *et al.* Solvent engineering for high-performance inorganic-organic hybrid perovskite solar cells. *Nat. Mater.* **13**, 897-903 (2014).
- 66 Nam, J. K. *et al.* Unveiling the crystal formation of cesium lead mixed-halide perovskites for efficient and stable solar cells. *J. Phys. Chem. Lett.* **8**, 2936-2940 (2017).
- 67 Liu, S. C. *et al.* Investigation of oxygen passivation for high-performance all-inorganic perovskite solar cells. *J. Am. Chem. Soc.* **141**, 18075-18082 (2019).
- 68 Sanchez, S. *et al.* Efficient and stable inorganic perovskite solar cells manufactured by pulsed flash infrared annealing. *Adv. Energy Mater.* **8**, 1802060 (2018).
- 69 Rao, H. *et al.* Morphology controlling of all-inorganic perovskite at low temperature for efficient rigid and flexible solar cells. *Adv. Energy Mater.* **8**, 1800758 (2018).
- 70 Burwig, T., Franzel, W. & Pistor, P. Crystal phases and thermal stability of co-evaporated CsPbX₃ (X = I, Br) thin films. *J. Phys. Chem. Lett.* **9**, 4808-4813 (2018).
- 71 Ma, Q., Huang, S., Wen, X., Green, M. A. & Ho-Baillie, A. W. Y. Hole transport layer free inorganic CsPbIBr₂ perovskite solar cell by dual source thermal evaporation. *Adv. Energy Mater.* **6**, 1502202 (2016).
- 72 Frolova, L. A. *et al.* Highly efficient all-inorganic planar heterojunction perovskite solar cells produced by thermal coevaporation of CsI and PbI₂. *J. Phys. Chem. Lett.* **8**, 67-72 (2017).
- 73 Liu, M. Z., Johnston, M. B. & Snaith, H. J. Efficient planar heterojunction perovskite solar cells by vapour deposition. *Nature* **501**, 395-398 (2013).
- 74 Tenuta, E., Zheng, C. & Rubel, O. Thermodynamic origin of instability in hybrid halide perovskites. *Sci. Rep.* **6**, 37654 (2016).
- 75 Kulbak, M., Cahen, D. & Hodes, G. How important is the organic part of lead halide perovskite photovoltaic cells? Efficient CsPbBr₃ cells. *J. Phys. Chem. Lett.* **6**, 2452-2456 (2015).
- 76 Liang, J. *et al.* All-inorganic perovskite solar cells. *J. Am. Chem. Soc.* **138**, 15829-15832 (2016).
- 77 Liang, J. *et al.* CsPb_{0.9}Sn_{0.1}IBr₂ based all-inorganic perovskite solar cells with exceptional efficiency and stability. *J. Am. Chem. Soc.* **139**, 14009-14012 (2017).
- 78 Liang, J. *et al.* Defect-engineering-enabled high-efficiency all-inorganic perovskite solar cells. *Adv. Mater.* **31**, e1903448 (2019).

- 79 Teng, P. *et al.* Elegant face-down liquid-space-restricted deposition of CsPbBr₃ films for efficient carbon-based all-inorganic planar perovskite solar cells. *ACS Appl. Mater. Interfaces* **10**, 9541-9546 (2018).
- 80 Numata, Y., Sanehira, Y., Ishikawa, R., Shirai, H. & Miyasaka, T. Thiocyanate containing two-dimensional cesium lead iodide perovskite, Cs₂PbI₂(SCN)₂: Characterization, photovoltaic application, and degradation mechanism. *ACS Appl. Mater. Interfaces* (2018).
- 81 Liao, J.-F., Rao, H.-S., Chen, B.-X., Kuang, D.-B. & Su, C.-Y. Dimension engineering on cesium lead iodide for efficient and stable perovskite solar cells. *J. Mater. Chem. A* **5**, 2066-2072 (2017).
- 82 Jiang, Y. *et al.* Reduced-dimensional α -CsPbX₃ perovskites for efficient and stable photovoltaics. *Joule* (2018).
- 83 Li, Y. *et al.* Lattice modulation of alkali metal cations doped Cs_{1-x}R_xPbBr₃ halides for inorganic perovskite solar cells. *Solar RRL* **2**, 1800164 (2018).
- 84 Li, N., Zhu, Z., Li, J., Jen, A. K. Y. & Wang, L. Inorganic CsPb_{1-x}Sn_xIBr₂ for efficient wide-bandgap perovskite solar cells. *Adv. Energy Mater.* **8**, 1800525 (2018).
- 85 Hu, M. *et al.* Sub-1.4eV bandgap inorganic perovskite solar cells with long-term stability. *Nat. Commun.* **11**, 151 (2020).
- 86 Kubicki, D. J. *et al.* Doping and phase segregation in Mn²⁺- and Co²⁺-doped lead halide perovskites from ¹³³Cs and ¹H NMR relaxation enhancement. *J. Mater. Chem. A* **7**, 2326-2333 (2019).
- 87 Akkerman, Q. A., Meggiolaro, D., Dang, Z., De Angelis, F. & Manna, L. Fluorescent alloy CsPb_xMn_{1-x}I₃ perovskite nanocrystals with high structural and optical stability. *ACS Energy Lett.* **2**, 2183-2186 (2017).
- 88 Bai, D. *et al.* Interstitial Mn²⁺-driven high-aspect-ratio grain growth for low-trap-density microcrystalline films for record efficiency CsPbI₂Br solar cells. *ACS Energy Lett.* **3**, 970-978 (2018).
- 89 Lau, C. F. J. *et al.* Strontium-doped low-temperature-processed CsPbI₂Br perovskite solar cells. *ACS Energy Lett.* **2**, 2319-2325 (2017).
- 90 Chen, L. *et al.* Inverted all-inorganic CsPbI₂Br perovskite solar cells with promoted efficiency and stability by nickel incorporation. *Chem. Mater.* **31**, 9032-9039 (2019).
- 91 Wang, K. L. *et al.* Tailored phase transformation of CsPbI₂Br films by copper(II) bromide for high-performance all-inorganic perovskite solar cells. *Nano Lett.* **19**, 5176-5184 (2019).
- 92 Zhao, Y., Wang, Y., Duan, J., Yang, X. & Tang, Q. Divalent hard Lewis acid doped CsPbBr₃ films for 9.63%-efficiency and ultra-stable all-inorganic perovskite solar cells. *J. Mater. Chem. A* **7**, 6877-6882 (2019).
- 93 Abdelhady, A. L. *et al.* Heterovalent dopant incorporation for bandgap and type engineering of perovskite crystals. *J. Phys. Chem. Lett.* **7**, 295-301 (2016).
- 94 Miao, X. *et al.* Air-stable CsPb_{1-x}Bi_xBr₃ (0 ≤ x < 1) perovskite crystals: optoelectronic and photostriction properties. *J. Mater. Chem. C* **5**, 4931-4939 (2017).
- 95 Hu, Y. *et al.* Bismuth incorporation stabilized α -CsPbI₃ for fully inorganic perovskite solar cells. *ACS Energy Lett.* **2**, 2219-2227 (2017).
- 96 Liu, C. *et al.* Structurally reconstructed CsPbI₂Br perovskite for highly stable and square-

- centimeter all-inorganic perovskite solar cells. *Adv. Energy Mater.*, 1803572 (2018).
- 97 Xiang, S. *et al.* The synergistic effect of non-stoichiometry and Sb-doping on air-stable α -CsPbI₃ for efficient carbon-based perovskite solar cells. *Nanoscale* **10**, 9996-10004 (2018).
- 98 Duan, J. *et al.* Lanthanide ions doped CsPbBr₃ halides for HTM-free 10.14%-efficiency inorganic perovskite solar cell with an ultrahigh open-circuit voltage of 1.594 V. *Adv. Energy Mater.* **8**, 1802346 (2018).
- 99 Swarnkar, A. *et al.* Quantum dot-induced phase stabilization of α -CsPbI₃ perovskite for high-efficiency photovoltaics. *Science* **354**, 92-95 (2016).
- 100 Wang, Q. *et al.* μ -graphene crosslinked CsPbI₃ quantum dots for high efficiency solar cells with much improved stability. *Adv. Energy Mater.* **8**, 1800007 (2018).
- 101 Sanehira, E. M. *et al.* Enhanced mobility CsPbI₃ quantum dot arrays for record-efficiency, high-voltage photovoltaic cells. *Sci. Adv.* **3**, eaao4204 (2017).
- 102 Fu, Y. *et al.* Selective stabilization and photophysical properties of metastable perovskite polymorphs of CsPbI₃ in thin films. *Chem. Mater.* **29**, 8385-8394 (2017).
- 103 Li, B. *et al.* Surface passivation engineering strategy to fully-inorganic cubic CsPbI₃ perovskites for high-performance solar cells. *Nat. Commun.* **9**, 1076 (2018).
- 104 Jeong, B. *et al.* All-inorganic CsPbI₃ perovskite phase-stabilized by poly(ethylene oxide) for red-light-emitting diodes. *Adv. Funct. Mater.* **28**, 1706401 (2018).
- 105 Wang, Q. *et al.* Stabilizing the α -phase of CsPbI₃ perovskite by sulfobetaine zwitterions in one-step spin-coating films. *Joule* **1**, 371-382 (2017).
- 106 Wang, Y. *et al.* Efficient α -CsPbI₃ photovoltaics with surface terminated organic cations. *Joule* **2**, 2065-2075 (2018).
- 107 Wang, Y., Zhang, T., Kan, M. & Zhao, Y. Bifunctional stabilization of all-inorganic α -CsPbI₃ perovskite for 17% efficiency photovoltaics. *J. Am. Chem. Soc.* **140**, 12345-12348 (2018).
- 108 Bian, H. *et al.* Graded bandgap CsPbI_{2+x}Br_{1-x} perovskite solar cells with a stabilized efficiency of 14.4%. *Joule* (2018).
- 109 Jeon, N. J. *et al.* Compositional engineering of perovskite materials for high-performance solar cells. *Nature* **517**, 476-480 (2015).
- 110 Burschka, J. *et al.* Sequential deposition as a route to high-performance perovskite-sensitized solar cells. *Nature* **499**, 316-319 (2013).
- 111 Berhe, T. A. *et al.* Organometal halide perovskite solar cells: degradation and stability. *Energy Environ. Sci.* **9**, 323-356 (2016).
- 112 Robert, F. Cesium fortifies next-generation solar cells. *Science* **351**, 113-114 (2016).
- 113 Liang, J., Liu, J. & Jin, Z. All-inorganic halide perovskites for optoelectronics: Progress and prospects. *Solar RRL* **1**, 1700086 (2017).
- 114 Kubicki, D. J. *et al.* Phase segregation in Cs-, Rb- and K-doped mixed-cation (MA)_x(FA)_{1-x}PbI₃ hybrid perovskites from solid-state NMR. *J. Am. Chem. Soc.* **139**, 14173-14180 (2017).
- 115 Rosales, B. A. *et al.* Persistent dopants and phase segregation in organolead mixed-halide perovskites. *Chem. Mater.* **28**, 6848-6859 (2016).
- 116 Pan, J. *et al.* Bidentate ligand-passivated CsPbI₃ perovskite nanocrystals for stable near-unity photoluminescence quantum yield and efficient red light-emitting diodes. *J. Am. Chem. Soc.* **140**, 562-565 (2018).

- 117 Yi, C. *et al.* Entropic stabilization of mixed A-cation ABX₃ metal halide perovskites for high
performance perovskite solar cells. *Energy Environ. Sci.* **9**, 656-662 (2016).
- 118 Lefevre, G. *et al.* Electron-phonon coupling in luminescent europium doped hydride perovskites
studied by luminescence spectroscopy, inelastic neutron scattering, and first-principle
calculations. *J. Phys. Chem. C* **122**, 10501-10509 (2018).
- 119 Swarnkar, A., Mir, W. J. & Nag, A. Can B-site doping or alloying improve thermal- and phase-
stability of all-inorganic CsPbX₃ (X = Cl, Br, I) perovskites? *ACS Energy Lett.* **3**, 286-289
(2018).
- 120 Kubicki, D. J. *et al.* Cation dynamics in mixed-cation (MA)_x(FA)_{1-x}PbI₃ hybrid perovskites from
solid-state NMR. *J. Am. Chem. Soc.* **139**, 10055-10061 (2017).
- 121 Kubicki, D. J. *et al.* Formation of stable mixed guanidinium-methylammonium phases with
exceptionally long carrier lifetimes for high-efficiency lead iodide-based perovskite
photovoltaics. *J. Am. Chem. Soc.* **140**, 3345-3351 (2018).
- 122 Kubicki, D. J. *et al.* Phase segregation in potassium-doped lead halide perovskites from ³⁹K
solid-state NMR at 21.1 T. *J. Am. Chem. Soc.* **140**, 7232-7238 (2018).
- 123 Knight, M. J., Felli, I. C., Pierattelli, R., Emsley, L. & Pintacuda, G. Magic angle spinning NMR
of paramagnetic proteins. *Acc. Chem. Res.* **46**, 2108-2116 (2013).
- 124 Hu, Y., Aygüler, M. F., Petrus, M. L., Bein, T. & Docampo, P. Impact of rubidium and cesium
cations on the moisture stability of multiple-cation mixed-halide perovskites. *ACS Energy Lett.*
2, 2212-2218 (2017).
- 125 Solomon, I. Relaxation processes in a system of two spins. *Physical Review* **99**, 559 (1955).
- 126 Tress, W. *et al.* Predicting the open-circuit voltage of CH₃NH₃PbI₃ perovskite solar cells using
electroluminescence and photovoltaic quantum efficiency spectra: the role of radiative and non-
radiative recombination. *Adv. Energy Mater.* **3**, 6 (2015).
- 127 Tress, W. *et al.* Interpretation and evolution of open-circuit voltage, recombination, ideality
factor and subgap defect states during reversible light-soaking and irreversible degradation of
perovskite solar cells. *Energy Environ. Sci.* **11**, 151-165 (2018).
- 128 Tress, W. *et al.* Understanding the rate-dependent J–V hysteresis, slow time component, and
aging in CH₃NH₃PbI₃ perovskite solar cells: the role of a compensated electric field. *Energy
Environ. Sci.* **8**, 995-1004 (2015).
- 129 Giebink, N. C., Wiederrecht, G. P., Wasielewski, M. R. & Forrest, S. R. Ideal diode equation for
organic heterojunctions. I. Derivation and application. *Phys. Rev. B* **82**, 155305 (2010).
- 130 Ahmad, W., Khan, J., Niu, G. & Tang, J. Inorganic CsPbI₃ perovskite-based solar cells: A choice
for a tandem device. *Solar RRL* **1**, 1700048 (2017).
- 131 Li, Z. *et al.* Acid additives enhancing the conductivity of spiro-OMeTAD toward high-efficiency
and hysteresis-less planar perovskite solar cells. *Adv. Energy Mater.* **7**, 1601451 (2017).
- 132 Prochowicz, D. *et al.* One-step mechanochemical incorporation of an insoluble cesium additive
for high performance planar heterojunction solar cells. *Nano Energy* **49**, 523-528 (2018).
- 133 Yang, S. *et al.* Functionalization of perovskite thin films with moisture-tolerant molecules. *Nat.
Energy* **1**, 15016 (2016).
- 134 Domanski, K., Alharbi, E. A., Hagfeldt, A., Grätzel, M. & Tress, W. Systematic investigation of
the impact of operation conditions on the degradation behaviour of perovskite solar cells. *Nat.*

- Energy* **3**, 61-67 (2018).
- 135 Xiang, W. *et al.* Europium-doped CsPbI₂Br for stable and highly efficient inorganic perovskite solar cells. *Joule* **3**, 205-214 (2019).
- 136 Ke, W. & Kanatzidis, M. G. Prospects for low-toxicity lead-free perovskite solar cells. *Nat. Commun.* **10**, 965 (2019).
- 137 Hao, F., Stoumpos, C. C., Cao, D. H., Chang, R. P. H. & Kanatzidis, M. G. Lead-free solid-state organic–inorganic halide perovskite solar cells. *Nat. Photon.* **8**, 489-494 (2014).
- 138 Ju, M. G., Dai, J., Ma, L. & Zeng, X. C. Lead-free mixed tin and germanium perovskites for photovoltaic application. *J. Am. Chem. Soc.* **139**, 8038-8043 (2017).
- 139 Shi, Z. *et al.* Lead-free organic-inorganic hybrid perovskites for photovoltaic applications: recent advances and perspectives. *Adv. Mater.* **29**, 1605005 (2017).
- 140 Mir, W. J., Jagadeeswararao, M., Das, S. & Nag, A. Colloidal Mn-doped cesium lead halide perovskite nanoplatelets. *ACS Energy Lett.* **2**, 537-543 (2017).
- 141 Klug, M. T. *et al.* Tailoring metal halide perovskites through metal substitution: influence on photovoltaic and material properties. *Energy Environ. Sci.* **10**, 236-246 (2017).
- 142 Bi, D. Q. *et al.* Polymer-templated nucleation and crystal growth of perovskite films for solar cells with efficiency greater than 21%. *Nat. Energy* **1**, 5 (2016).
- 143 Dec, S. F. *et al.* Solid-state multinuclear NMR-studies of ferroelectric, piezoelectric, piezoelectric, and related materials. *Inorg. Chem.* **32**, 955-959 (1993).
- 144 Hamaed, H., Ye, E., Udachin, K. & Schurko, R. W. Solid-state ¹³⁷Ba NMR spectroscopy: An experimental and theoretical investigation of ¹³⁷Ba electric field gradient tensors and their relation to structure and symmetry. *J. Phys. Chem. B* **114**, 6014-6022 (2010).
- 145 Leijtens, T. *et al.* Stability of metal halide perovskite solar cells. *Adv. Energy Mater.* **5**, 1500963 (2015).
- 146 Hayashi, S. & Hayamizu, K. Accurate determination of NMR chemical-shifts in alkali-halides and their correlation with structural factors. *B. Chem. Soc. Jpn.* **63**, 913-919 (1990).
- 147 Kresse, G. & Furthmüller, J. Efficiency of ab-initio total energy calculations for metals and semiconductors using a plane-wave basis set. *Comput. Mater. Sci.* **6**, 15-50 (1996).
- 148 Kresse, G. & Furthmüller, J. Efficient iterative schemes for ab initio total-energy calculations using a plane-wave basis set. *Phys. Rev. B* **54**, 11169-11186 (1996).
- 149 Perdew, J. P., Burke, K. & Ernzerhof, M. Generalized gradient approximation made simple. *Phys. Rev. Lett.* **77**, 3865-3868 (1996).
- 150 Van de Walle, A. *et al.* Efficient stochastic generation of special quasirandom structures. *Calphad* **42**, 13-18 (2013).
- 151 Stranks, S. D. *et al.* Electron-hole diffusion lengths exceeding 1 micrometer in an organometal trihalide perovskite absorber. *Science* **342**, 341-344 (2013).
- 152 Jung, E. H. *et al.* Efficient, stable and scalable perovskite solar cells using poly(3-hexylthiophene). *Nature* **567**, 511-515 (2019).
- 153 Jiang, Q. *et al.* Surface passivation of perovskite film for efficient solar cells. *Nat. Photon.* **13**, 460-466 (2019).
- 154 Wang, K. *et al.* All-inorganic cesium lead iodide perovskite solar cells with stabilized efficiency

- beyond 15%. *Nat. Commun.* **9**, 4544 (2018).
- 155 Eperon, G. E. *et al.* Perovskite-perovskite tandem photovoltaics with optimized band gaps. *Science* **354**, 861-865 (2016).
- 156 Zhou, H. *et al.* Interface engineering of highly efficient perovskite solar cells. *Science* **345**, 542-546 (2014).
- 157 Tan, H. R. *et al.* Efficient and stable solution-processed planar perovskite solar cells via contact passivation. *Science* **355**, 722-726 (2017).
- 158 Mei, A. *et al.* A hole-conductor-free, fully printable mesoscopic perovskite solar cell with high stability. *Science* **345**, 295-298 (2014).
- 159 Li, X. *et al.* Improved performance and stability of perovskite solar cells by crystal crosslinking with alkylphosphonic acid omega-ammonium chlorides. *Nat. Chem.* **7**, 703-711 (2015).
- 160 Feng, H.-J., Huang, J. & Zeng, X. C. Photovoltaic diode effect induced by positive bias poling of organic layer-mediated interface in perovskite heterostructure α -HC(NH₂)₂PbI₃/TiO₂. *Advanced Materials Interfaces* **3**, 1600267 (2016).
- 161 Zhang, J., Chen, Y. & Guo, W. Optimizing the efficiency of perovskite solar cells by a sub-nanometer compact titanium oxide electron transport layer. *Nano Energy* **49**, 230-236 (2018).
- 162 Milić, J. V. *et al.* Supramolecular engineering for formamidinium-based layered 2D perovskite solar cells: Structural complexity and dynamics revealed by solid-state NMR spectroscopy. *Adv. Energy Mater.* **9**, 1900284 (2019).
- 163 Franssen, W. M. J. & Kentgens, A. P. M. Solid-state NMR of hybrid halide perovskites. *Solid State Nucl. Magn. Reson.* **100**, 36-44 (2019).
- 164 Walker, B., Kim, G. H. & Kim, J. Y. Pseudohalides in lead-based perovskite semiconductors. *Adv. Mater.* **31**, e1807029 (2019).
- 165 Li, W. *et al.* Chemically diverse and multifunctional hybrid organic–inorganic perovskites. *Nat. Rev. Mater.* **2**, 16099 (2017).
- 166 Karmakar, A. *et al.* Mechanochemical synthesis of 0D and 3D cesium lead mixed halide perovskites. *Chem. Commun.* **55**, 5079-5082 (2019).
- 167 Li, C. *et al.* Methylammonium-mediated evolution of mixed-organic-cation perovskite thin films: A dynamic composition-tuning Process. *Angew. Chem. Int. Ed.* **56**, 7674-7678 (2017).
- 168 Fan, L.-Q. & Wu, J.-H. NH₄PbI₃. *Acta Crystallogr. E* **63**, i189-i189 (2007).
- 169 Sheikh, T. & Nag, A. Mn doping in centimeter-sized layered 2D butylammonium lead bromide (BA₂PbBr₄) single crystals and their optical properties. *J. Phys. Chem. C* **123**, 9420-9427 (2019).
- 170 Fu, Y. *et al.* Metal halide perovskite nanostructures for optoelectronic applications and the study of physical properties. *Nat. Rev. Mater.* **4**, 169-188 (2019).
- 171 Turren-Cruz, S. H., Hagfeldt, A. & Saliba, M. Methylammonium-free, high-performance, and stable perovskite solar cells on a planar architecture. *Science* **362**, 449-453 (2018).
- 172 Bi, D. *et al.* Efficient luminescent solar cells based on tailored mixed-cation perovskites. *Sci. Adv.* **2**, e1501170 (2016).
- 173 Mosconi, E., Ronca, E. & De Angelis, F. First-principles investigation of the TiO₂/organohalide perovskites interface: The role of interfacial chlorine. *J. Phys. Chem. Lett.* **5**, 2619-2625 (2014).
- 174 Ning, Z. *et al.* Quantum-dot-in-perovskite solids. *Nature* **523**, 324-328 (2015).
- 175 Tsai, H. *et al.* High-efficiency two-dimensional Ruddlesden-Popper perovskite solar cells.

- Nature* **536**, 312-316 (2016).
- 176 Wang, Z. *et al.* Additive-modulated evolution of $\text{HC}(\text{NH}_2)_2\text{PbI}_3$ black polymorph for mesoscopic perovskite solar cells. *Chem. Mater.* **27**, 7149-7155 (2015).
- 177 Zhang, J. *et al.* Intermediate phase enhances inorganic perovskite and metal oxide interface for efficient photovoltaics. *Joule* **4**, 222-234 (2020).
- 178 Zong, Y. *et al.* Thin-film transformation of NH_4PbI_3 to $\text{CH}_3\text{NH}_3\text{PbI}_3$ Perovskite: A methylamine-induced conversion-healing process. *Angew. Chem. Int. Ed.* **55**, 14723-14727 (2016).
- 179 Cao, D. H., Stoumpos, C. C., Farha, O. K., Hupp, J. T. & Kanatzidis, M. G. 2D homologous perovskites as light-absorbing materials for solar cell applications. *J. Am. Chem. Soc.* **137**, 7843-7850 (2015).
- 180 Jena, A. K., Kulkarni, A., Sanehira, Y., Ikegami, M. & Miyasaka, T. Stabilization of $\alpha\text{-CsPbI}_3$ in ambient room temperature conditions by incorporating Eu into CsPbI_3 . *Chem. Mater.* **30**, 6668-6674 (2018).
- 181 Liang, J. *et al.* Enhancing optical, electronic, crystalline, and morphological properties of cesium lead halide by Mn substitution for high-stability all-inorganic perovskite solar cells with carbon electrodes. *Adv. Energy Mater.* **8**, 1800504 (2018).
- 182 Zeng, Q. *et al.* Polymer-passivated inorganic cesium lead mixed-halide perovskites for stable and efficient solar cells with high open-circuit voltage over 1.3 V. *Adv. Mater.* **30**, 1705393 (2018).
- 183 Yan, L. *et al.* Interface engineering for all-inorganic CsPbI_2Br perovskite solar cells with efficiency over 14%. *Adv. Mater.* **30**, e1802509 (2018).
- 184 Zhang, J. *et al.* Iodine-optimized interface for inorganic CsPbI_2Br perovskite solar cell to attain high stabilized efficiency exceeding 14%. *Adv. Sci.* **5**, 1801123 (2018).
- 185 Guo, Z. *et al.* Achievable high V_{oc} of carbon based all-inorganic CsPbIBr_2 perovskite solar cells through interface engineering. *J. Mater. Chem. A* **7**, 1227-1232 (2019).
- 186 Duan, J., Hu, T., Zhao, Y., He, B. & Tang, Q. Carbon-electrode-tailored all-inorganic perovskite solar cells to harvest solar and water-vapor energy. *Angew. Chem. Int. Ed.* **57**, 5746-5749 (2018).
- 187 Akkerman, Q. A. *et al.* Strongly emissive perovskite nanocrystal inks for high-voltage solar cells. *Nat. Energy* **2**, e16194 (2016).
- 188 Zhou, Y. *et al.* Benzylamine-treated wide-bandgap perovskite with high thermal-photostability and photovoltaic performance. *Adv. Energy Mater.* **7**, 1701048 (2017).
- 189 Zheng, X. *et al.* Defect passivation in hybrid perovskite solar cells using quaternary ammonium halide anions and cations. *Nat. Energy* **2**, e17102 (2017).
- 190 Wang, Z. *et al.* Efficient ambient-air-stable solar cells with 2D-3D heterostructured butylammonium-caesium-formamidinium lead halide perovskites. *Nat. Energy* **2**, 17135 (2017).
- 191 Duong, T. *et al.* Rubidium multication perovskite with optimized bandgap for perovskite-silicon tandem with over 26% efficiency. *Adv. Energy Mater.* **7**, 1700228 (2017).
- 192 McMeekin, D. P. *et al.* A mixed-cation lead mixed-halide perovskite absorber for tandem solar cells. *Science* **351**, 151-155 (2016).
- 193 Kim, J. *et al.* Amide-catalyzed phase-selective crystallization reduces defect density in wide-bandgap perovskites. *Adv. Mater.* **30**, e1706275 (2018).
- 194 Yu, Y. *et al.* Synergistic effects of lead thiocyanate additive and solvent annealing on the

- performance of wide-bandgap perovskite solar cells. *ACS Energy Lett.* **2**, 1177-1182 (2017).
- 195 Bush, K. A. *et al.* Compositional engineering for efficient wide band gap perovskites with improved stability to photoinduced phase segregation. *ACS Energy Lett.* **3**, 428-435 (2018).
- 196 Jesper Jacobsson, T. *et al.* Exploration of the compositional space for mixed lead halogen perovskites for high efficiency solar cells. *Energy Environ. Sci.* **9**, 1706-1724 (2016).
- 197 Abdi-Jalebi, M. *et al.* Maximizing and stabilizing luminescence from halide perovskites with potassium passivation. *Nature* **555**, 497-501 (2018).
- 198 Chen, S. *et al.* Exploring the stability of novel wide bandgap perovskites by a robot based high throughput approach. *Adv. Energy Mater.* **8**, 1701543 (2018).
- 199 Rajagopal, A., Stoddard, R. J., Jo, S. B., Hillhouse, H. W. & Jen, A. K. Overcoming the photovoltage plateau in large bandgap perovskite photovoltaics. *Nano Lett.* **18**, 3985-3993 (2018).
- 200 Rajagopal, A. *et al.* Highly efficient perovskite-perovskite tandem solar cells reaching 80% of the theoretical limit in photovoltage. *Adv. Mater.* **29**, 1702140 (2017).
- 201 Arora, N. *et al.* High open-circuit voltage: fabrication of formamidinium lead bromide perovskite solar cells using fluorene-dithiophene derivatives as hole-transporting materials. *ACS Energy Lett.* **1**, 107-112 (2016).
- 202 Arora, N. *et al.* Intrinsic and extrinsic stability of formamidinium lead bromide perovskite solar cells yielding high photovoltage. *Nano Lett.* **16**, 7155-7162 (2016).
- 203 Dar, M. I. *et al.* Function follows form: Correlation between the growth and local emission of perovskite structures and the performance of solar cells. *Adv. Funct. Mater.* **27**, 1701433 (2017).
- 204 Hu, X. *et al.* Wide-bandgap perovskite solar cells with large open-circuit voltage of 1653 mV through interfacial engineering. *Solar RRL* **2**, 1800083 (2018).
- 205 Wu, C.-G., Chiang, C.-H. & Chang, S. H. A perovskite cell with a record-high- V_{oc} of 1.61 V based on solvent annealed $\text{CH}_3\text{NH}_3\text{PbBr}_3/\text{ICBA}$ active layer. *Nanoscale* **8**, 4077-4085 (2016).

Acknowledgements

During my PhD student, I am lucky to study and work at the highly internationalized, comprehensive and freedom lab (LSPM) in EPFL, Switzerland, which make me achieve and grew a lot. Many people have given me valuable helps in work and accompanied me in life to make my life rich and wonderful.

Foremost, I would like to express my deepest gratitude to Prof. Anders Hagfeldt, my supervisor, for accepting me as his PhD student. His constant encouragement, full support and freedom make me an enjoyable experience in scientific research, study and life.

Secondly, I want to thank my close cooperators, Jiahuan Zhang and Dr. Wanchun Xiang in inorganic perovskites. They make my thesis proceed smoothly in the new research direction. Their company makes my life more wonderful.

Then I am sincerely thankful to Prof. Michael Graetzel for giving the guidance and suggestions in my project. Then I wish to express my thanks to the secretaries-Heidi Francelet, Carmen Biagini and Anne-Lene Odegaard for their timely help on many occasions.

I thank Prof. Xiong Li, and Dr. Hui-Seon Kim as my guide give the guidance and training when I just came EPFL. Then I am grateful for these helps from Prof. Jingshan Luo, Prof. Sining Yun, Dr. Yuhang Liu, Dr. Linfeng Pan, Prof. Dongqin Bi, Prof. Chenyi, Yi, Dr. Yiming Cao and Dr. Yuxiang Yu in work and life.

I am grateful for the valuable scientific inputs on various projects, provided by Dr. Dominik Kubicki, Aditya Mishra for ss-NMR, Dr. Wolfgang Tress for EL and PL, Prof. Lijun Zhang for calculations, Dr. Wenhua Bi for XRD.

I wish to express my thanks to my collaborators on various projects-Dr. Haibing Xie, Prof. Monica Lira, Prof. Shuping Pang, Dr. Zhipeng Shao, Li Hong, Huanhuan Wang. I would like to thank Anand Agarwalla, Brian Carlsen, and Yasemin Saygili for the help in teaching. I am sincerely thankful to Dr. Shuangyan Hu for formatting my thesis. Particularly, I should give special thanks to Thomas Paul Baumeler for helping me translate the abstract into a French version.

I thank my colleagues Dr. Zaakeeruddin, Dr. Yang Li, Anwar Alanazi, Essa Alharbi, Dr. Mozhang Yavari, Dr. Mona Shasti, Dr. Dan Ren, Dr. Haizhou Lu, Dr. Zishuai Wang, Dr. Felix Eickemeyer, Paul Liska, Dr. Lichen Zhao, Dr. Feng Wang, Dr. Jun Li, Natalie Diaz, Dr. Ibrahim Dar, Dr. Hong Zhang, Dr. Yameng Ren, Dr. Bowen Yang, Dr. Jiajia Suo, Dr. Fei Zhang, Prof. Hujiang Shen, Qixing Zhang, Dr. Jing Gao, Dr. Bitao Dong, Hongwei Zhu, Yunfei Jiao,

Chunyang Zhang, Xufeng Lin and others at LSPM and LPI for all valuable discussion and happy times.

I also want to thank my friends in Switzerland, especially including Dr. Zhaofu Fei, Dr. Fan Fu, Lijie Wang, Dr. Xiaopeng Huang, Dr. Shengcai Zheng, Jiangtao Zhou, Dr. Guosheng He, Dr. Zhangjun Huang, Weiyan Ni and Lichen Bai.

Last but not least, I would like to thank my beloved parents, brother and sister for their unconditional love, support and encouragement during my pursuit in the career.

Zaiwei Wang

Lausanne, April 2^{ed}, 2020

Curriculum Vitae

Personal Information.

Name: Zaiwei Wang

Gender: Male

University: École polytechnique fédérale de Lausanne. Degree: Ph.D. Student

Address: Chemin du Couchant 23, 1007 Lausanne. Date of Birth: April 23, 1988

Email: Zaiwei.wang@epfl.ch

Telephone: +41 786533184

OrcID: 0000-0001-9725-0206

ResearcherID: X-4335-2019



Education.

2017.03—Present: Ph.D. candidate in École polytechnique fédérale de Lausanne (EPFL)

Major: Physical chemistry

Supervisor: Prof. Anders Hagfeldt

Date of Ph.D. defense: May 12, 2020.

2013.09—2016.07: Master in Qingdao Institute of Bioprocess and Bioenergy Technology,
Chinese Academy of Science

Major: Chemical Engineering

Supervisor: Prof. Shuping Pang and Prof. Guanglei Cui

2009.09—2016.07: Bachelor in Qingdao University of Science and Technology

Major: Chemistry

Prizes, awards, fellowships.

2016.06 Outstanding Graduate, University of Chinese Academy of Sciences

2015.11 National Scholarship, University of Chinese Academy of Sciences

2015.06 Merit Student, University of Chinese Academy of Sciences.

2011.09 National Encouragement scholarship of ministry of education.

Personal Skills.

Language Skill: English, Chinese.

Experimental Skill: Perovskite materials synthesis, the preparation of PSCs, Scanning electron

microscopy, X-ray diffraction, Cathode Luminescence, Photoluminescence, UV-Vis spectrophotometer.

Publications.

First or corresponding author:

1. Zhang, J.[#]; **Wang, Z.**^{*,#}; Mishra, A.; Yu, M.; Shasti, M.; Tress, W.; Kubicki, D. J.; Avalos, C. E.; Lu, H.; Liu, Y.; Carlsen, B. I.; Agarwalla, A.; Wang, Z.; Xiang, W.; Emsley, L.; Zhang, Z.; Grätzel, M.; Guo, W.; Hagfeldt, A., Intermediate phase enhances inorganic perovskite and metal oxide interface for efficient photovoltaics. *Joule* 2020, 4 (1), 222-234. (co-first and corresponding author). <https://www.sciencedirect.com/science/article/pii/S2542435119305379> (co-first and corresponding author)
2. Xiang, W.[#]; **Wang, Z.**[#]; Kubicki, D. J.; Wang, X.; Tress, W.; Luo, J.; Zhang, J.; Hofstetter, A.; Zhang, L.; Emsley, L.; Grätzel, M.; Hagfeldt, A., Ba-induced phase segregation and band gap reduction in mixed-halide inorganic perovskite solar cells. *Nat. Commun.* 2019, 10 (1), 4686. <https://www.nature.com/articles/s41467-019-12678-5> (co-first author)
3. Xiang, W.[#]; **Wang, Z.**[#]; Kubicki, D. J.; Tress, W.; Luo, J.; Prochowicz, D.; Akin, S.; Emsley, L.; Zhou, J.; Dietler, G.; Grätzel, M.; Hagfeldt, A., Europium-doped CsPbI₂Br for stable and highly efficient inorganic perovskite solar cells. *Joule* 2019, 3 (1), 205-214. <https://www.sciencedirect.com/science/article/pii/S2542435118304707> (co-first author)
4. Shao, Z.[#]; **Wang, Z.**[#]; Li, Z.; Fan, Y.; Meng, H.; Liu, R.; Wang, Y.; Hagfeldt, A.; Cui, G.; Pang, S., A scalable methylamine gas healing strategy for high-efficiency inorganic perovskite solar cells. *Angew. Chem.-Int. Edit.* 2019, 58 (17), 5587-5591. <https://onlinelibrary.wiley.com/doi/full/10.1002/anie.201814024> (co-first author)
5. Pang, S.[#]; Zhou, Y.[#]; **Wang, Z.**[#]; Yang, M.; Krause, A. R.; Zhou, Z.; Zhu, K.; Padture, N. P.; Cui, G., Transformative evolution of organolead triiodide perovskite thin films from strong room-temperature solid-gas interaction between HPbI₃-CH₃NH₂ precursor pair. *J. Am. Chem. Soc.* 2016, 138 (3), 750-3. <https://pubs.acs.org/doi/abs/10.1021/jacs.5b11824> (co-first author)
6. Zhou, Z.[#]; **Wang, Z.**[#]; Zhou, Y.; Pang, S.; Wang, D.; Xu, H.; Liu, Z.; Padture, N. P.; Cui, G., Methylamine-gas-induced defect-healing behavior of CH₃NH₃PbI₃ thin films for perovskite solar cells. *Angew. Chem.-Int. Edit.* 2015, 54 (33), 9705-9. <https://onlinelibrary.wiley.com/doi/full/10.1002/anie.201504379> (co-first author)
7. **Wang, Z.**[#]; Zhou, Y.[#]; Pang, S.; Xiao, Z.; Zhang, J.; Chai, W.; Xu, H.; Liu, Z.; Padture, N. P.; Cui, G., Additive-modulated evolution of HC(NH₂)₂PbI₃ black

- polymorph for mesoscopic perovskite solar cells. *Chem. Mater.* 2015, 27 (20), 7149-7155. <https://pubs.acs.org/doi/abs/10.1021/acs.chemmater.5b03169>
8. Li, C. W. #; **Wang, Z.** #; Chang, Y.; Zong, Y. X.; Ji, F. X.; Zhang, B.; Li, H. Y.; Pang, S. P., Insight into the effect of ion source for the solution processing of perovskite films. *RSC Adv.* 2016, 6 (88), 85026-85029. <https://pubs.rsc.org/en/content/articlepdf/2016/ra/c6ra17197d> (co-first author)
 9. **Wang, Z.**; Xu, H.; Zhang, Z.; Zhou, X.; Pang, S.; Cui, G., High-performance cobalt selenide and nickel selenide nanocomposite counter electrode for both iodide/triiodide and cobalt(II/III) redox couples in dye-sensitized solar cells. *Chin. J. Chem.* 2014, 32 (6), 491-497. <https://onlinelibrary.wiley.com/doi/abs/10.1002/cjoc.201400003>
 10. Wang, H. #; **Wang, Z.** #; Yang, Z.; Xu, Y.; Ding, Y.; Tan, L.; Yi, C.; Zhang, Z.; Meng, K.; Chen, G.; Zhao, Y.; Luo, Y.; Zhang, X.; Hagfeldt, A.; Luo, L., Ligands-modulated excess PbI₂ nanosheets for highly efficient and stable perovskite solar cells. (Advance Materials, *Adv. Mater.* 2020, 2000865. (co-first author).

Co-author

11. Ren, D.; Gao, J.; Pan, L.; **Wang, Z.**; Luo, J.; Zakeeruddin, S. M.; Hagfeldt, A.; Gratzel, M., Atomic layer deposition of ZnO on CuO enables selective and efficient electroreduction of carbon dioxide to liquid fuels. *Angew. Chem.-Int. Edit.* 2019. DOI: 10.1002/ange.201909610 <https://onlinelibrary.wiley.com/doi/pdf/10.1002/ange.201909610>
12. Li, Y.; **Wang, Z.**; Ren, D.; Liu, Y.; Zheng, A.; Zakeeruddin, S. M.; Dong, X.; Hagfeldt, A.; Grätzel, M.; Wang, P., SnS quantum dots as hole transporter of perovskite solar cells. *ACS Applied Energy Materials* 2019, 2 (5), 3822-3829. <https://pubs.acs.org/doi/pdf/10.1021/acsam.9b00510?rand=tnvmix31>
13. Yavari, M.; Ebadi, F.; Meloni, S.; Wang, Z. S.; Yang, T. C.-J.; Sun, S.; Schwartz, H.; **Wang, Z.**; Niesen, B.; Durantini, J.; Rieder, P.; Tvingstedt, K.; Buonassisi, T.; Choy, W. C. H.; Filippetti, A.; Dittrich, T.; Olthof, S.; Correa-Baena, J.-P.; Tress, W., How far does the defect tolerance of lead-halide perovskites range? The example of Bi impurities introducing efficient recombination centers. *J. Mater. Chem. A* 2019. DOI: 10.1039/c9ta01744e <https://pubs.rsc.org/en/content/articlepdf/2019/ta/c9ta01744e>
14. Pérez-Tomas, A.; Xie, H.; **Wang, Z.**; Kim, H.-S.; Shirley, I.; Turren-Cruz, S.-H.; Morales-Melgares, A.; Saliba, B.; Tanenbaum, D.; Saliba, M.; Zakeeruddin, S. M.; Gratzel, M.; Hagfeldt, A.; Lira-Cantu, M., PbZrTiO₃ ferroelectric oxide as an electron extraction material for stable halide perovskite solar cells. *Sustainable Energy & Fuels* 2019, 3 (2), 382-389. <https://pubs.rsc.org/en/content/articlepdf/2019/sc/c8se00451j>

15. Mingorance, A.; Xie, H.; Kim, H. S.; **Wang, Z.**; Balsells, M.; Morales-Melgares, A.; Domingo, N.; Kazuteru, N.; Tress, W.; Fraxedas, J.; Vlachopoulos, N.; Hagfeldt, A.; Lira-Cantu, M., Interfacial engineering of metal oxides for highly stable halide perovskite solar cells. *Advanced Materials Interfaces* 2018, 5 (22), 1800367. <https://onlinelibrary.wiley.com/doi/pdf/10.1002/admi.201800367>
16. Liu, D.; Li, C.; Zhang, C.; **Wang, Z.**; Zhang, H.; Tian, J.; Pang, S., Blended additive manipulated morphology and crystallinity transformation toward high performance perovskite solar cells. *RSC Adv.* 2017, 7 (82), 51944-51949. <https://pubs.rsc.org/en/content/articlepdf/2017/ra/c7ra09954a>
17. Wang Dong, Z. H.-M., Zhou Zhong-Min, **Wang, Z.**, L; uuml; Si-Liu, P. S.-P., CuiGuang-Lei, Effect of solvent on the perovskite thin film morphology and crystallinity. *Acta Phys. Sin.* 2015, 64 (3), 38403. <http://wulixb.iphy.ac.cn/EN/abstract/abstract63373.shtml#>
18. Wang, D.; Liu, Z.; Zhou, Z.; Zhu, H.; Zhou, Y.; Huang, C.; **Wang, Z.**; Xu, H.; Jin, Y.; Fan, B.; Pang, S.; Cui, G., Reproducible one-step fabrication of compact MAPbI_{3-x}Cl_x thin films derived from mixed-lead-halide precursors. *Chem. Mater.* 2014, 26 (24), 7145-7150. <https://pubs.acs.org/doi/pdf/10.1021/cm5037869?rand=7zgol8j6>
19. Xu, H.; Zhang, C.; **Wang, Z.**; Pang, S.; Zhou, X.; Zhang, Z.; Cui, G., Nitrogen-doped carbon and iron carbide nanocomposites as cost-effective counter electrodes of dye-sensitized solar cells. *J. Mater. Chem. A* 2014, 2 (13), 4676-4681. <https://pubs.rsc.org/en/content/articlepdf/2014/ta/c3ta14429a>

Patents.

1. Cui, G.; Pang, S.; **Wang, Z.**; Zhou, Z.; Xu, H.; Zhang, B.; Liu, Z., 201510657577.4
2. Cui, G.; Pang, S.; **Wang, Z.**; Zhou, Z.; Xu, H.; Liu, Z. ; Chang, Y., 201510322422.5
3. Cui, G.; Pang, S.; Zhou, Z.; **Wang, Z.**; Xu, H.; Liu, Z. ; Chang, Y., 201510184150.